THE ORIGINS OF MAGNETIC ANOMALY LOWS ASSOCIATED WITH THREE IMPACT STRUCTURES

by

Ronald Glenn Scott B.Sc.

A thesis submitted to the School of Graduate Studies and Research

in partial fulfillment of the requirements

for the degree of M.Sc. in Earth Sciences

OTTAWA-CARLETON GEOSCIENCE CENTRE

AND

UNIVERSITY OF OTTAWA

OTTAWA, CANADA

ISBN 0-612-16463-2

Canada

UNIVERSITÉ D'OTTAWA
UNIVERSITY OF OTTAWA

ABSTRACT

The discovery and study of terrestrial impact structures is important not only for the elucidation of the Earth's impact history, but also for the economic and environmental aspects of these structures. Another important aspect is the study of the cratering process. Due to the effects of erosion, tectonism and burial, impact structures are often obscured or destroyed. Geophysical methods are increasingly being used in detecting the signatures of impact structures. While gravity lows associated with impact structures are well understood, associated magnetic anomaly lows are not. In this study, drill cores from three Canadian impact structures were analysed for rock magnetic properties and mineralogy, in order to explain the reduced magnetizations associated with these structures. Samples from the drill cores were cut and measured for AMS and NRM parameters. Drill cores from the twin impact craters of the Clearwater structure exhibited different natural remanent magnetization (NRM) characteristics, and samples from their respective drill cores were subject to demagnetization by alternating field and thermal techniques. The difference noted in their NRM characteristics was attributed to the acquisition of a viscous remanent magnetization (VRM) at depth in Clearwater East.

Both magnetic susceptibilities and remanent magnetizations are well below regional values in impact generated breccias, melt rocks, shocked crystalline rocks, and in post-impact sedimentary infill. The processes of brecciation, alteration, shock, and infill by non-magnetic sediments contribute to the development of the magnetic lows. However, a significant component of the magnetic anomalies was found by forward modeling to derive from the unshocked basement rocks

beneath the impact structures. This zone of reduced magnetization may be caused by the partial demagnetization of magnetite by the impact-induced transient stress wave travelling away from the point of impact, and the possible acquisition of a lower intensity shock remanent magnetization in the target rocks at depth.

Table of Contents

LIST OF FIGURES

FIG.

LIST OF TABLES

TABLE

STATEMENT OF ORIGINAL CONTRIBUTION

The study presented here began while I was a summer student at the Geological Survey of Canada (GSC), Geophysics Division, Geophysical Applications Section. The work was done under the supervision of Dr. Mark Pilkington, and with the training assistance of Elizabeth I. Tanczyk, M.Sc.

All sample preparation (sampling, re-coring, cutting), all magnetic measurements (magnetic susceptibility, NRM, AMS), and all demagnetization (AF, thermal) were done by myself. I also performed cutting and trimming for ten thin sections. The samples were sent to Vancouver Petrographics for final thin sectioning. E.I. Tanczyk provided training in the use of the magnetic instruments and the computer programs, RemDbase and AMSDbase. Dr. Keith Benn, University of Ottawa, provided training in the use of the KLY-2 Kappabridge.

Thin section petrography and photography was done by myself. Initial magnetic modelling was done by Dr. Mark Pilkington, however final detailed magnetic modelling was performed by myself with the guidance of Dr. Walter Roest (GSC) and Dr. Pilkington. Dr. Pilkington also provided his expertise in producing the figures used in this thesis.

Portions of this thesis have been presented at several conferences, with M. Pilkington and E.I. Tanczyk as co-authors. A condensed version of this thesis has also been accepted for review in *Meteoritics and Planetary Science*, with the same co-authors.

ACKNOWLEDGMENTS

Mark Pilkington (GSC) is thanked for hiring me as a summer student to work on this project, and for allowing me considerable latitude in pursuing the research. Mark is also thanked for producing the numerous figures that this project generated. Elizabeth Tanczyk is thanked for her assistance in training me in the use of the Palaeomagnetic Laboratory's instruments and computer analysis programs. Ken Buchan is thanked for providing the use of the Laboratory's instrumentation. Keith Benn is especially thanked for encouraging me to turn this project into a master's thesis, and for volunteering to shepherd the project through to its completion.

Elizabeth Tanczyk, Keith Benn, Mark Pilkington and Richard A.F. Grieve (GSC) are all thanked for numerous stimulating conversations and insights on both rock magnetism and cratering mechanics. Finally, Walter Roest (GSC, U of O) and Mark Pilkington are thanked for their assistance with the magnetic modelling.

1. INTRODUCTION

The geophysical detection of buried or eroded terrestrial impact structures has become an important method for discovering potential impact structures on the surface of the Earth. Structures such as Chicxulub, Mexico and Eagle Butte, Canada, are buried impact structures first detected by their gravity and/or magnetic anomaly signatures. The detection of impact structures on the surface of the Earth is important for several reasons. Impact structures on the Earth provide ground truth data for such studies as shock metamorphism, the nature of impact melts, response of isotopic systems to shock, estimation of the cratering flux over geologic history, and cratering mechanics (Grieve and Pesonen, 1992). Impact structures have been studied by use of gravity, magnetic and seismic methods (Pilkington and Grieve, 1992).

The magnetic anomaly lows associated with impact structures are not well understood, and consequently this study was undertaken in order to provide data that would enable a better understanding of the reduced magnetizations associated with terrestrial impact structures. Drill core from three Canadian impact structures (Figure 1); Deep Bay, Saskatchewan; West Hawk Lake, Manitoba; and Clearwater Lakes (East and West), Quebec, was analysed for magnetic susceptibility and its anisotropy (AMS), and natural remanent magnetization (NRM), to provide numerical constraints for forward modelling of the magnetic anomalies associated with each structure, and to identify magnetic carrier mineralogy.

Previous petrophysical studies of rocks from impact structures were limited to surface sample collection and analysis. Due to the availability of numerous drill cores from Canadian impact structures, the study of the petrophysical properties of impact rocks could be extended

below the surface for the first time. This allowed for the construction of well constrained magnetic models for the impact structures studied that consequently permitted detailed study of the resulting magnetic anomalies associated with each structure.

Results from this unique study indicate that the magnetic anomaly lows associated with these three structures are only partially due to brecciation, alteration, shock demagnetization, and infill by non-magnetic sediments. The magnetic lows are also due to demagnetizing effects of the transient stress wave at the time of impact in the surrounding target rocks of the impact structures. This stress wave is the attenuated shock wave due to the initial impact, and is characterized by pressures low enough to avoid optically visible structural changes in silicate minerals (typical of shock metamorphism), but high enough to affect the magnetocrystalline structure of magnetite grains. The principle effect of the transient stress wave appears to be a reduction in magnetic intensity that extends far beyond the calculated morphological dimensions of the impact structures. This reduction in magnetization contributes significantly to the magnetic anomaly lows associated with these structures.

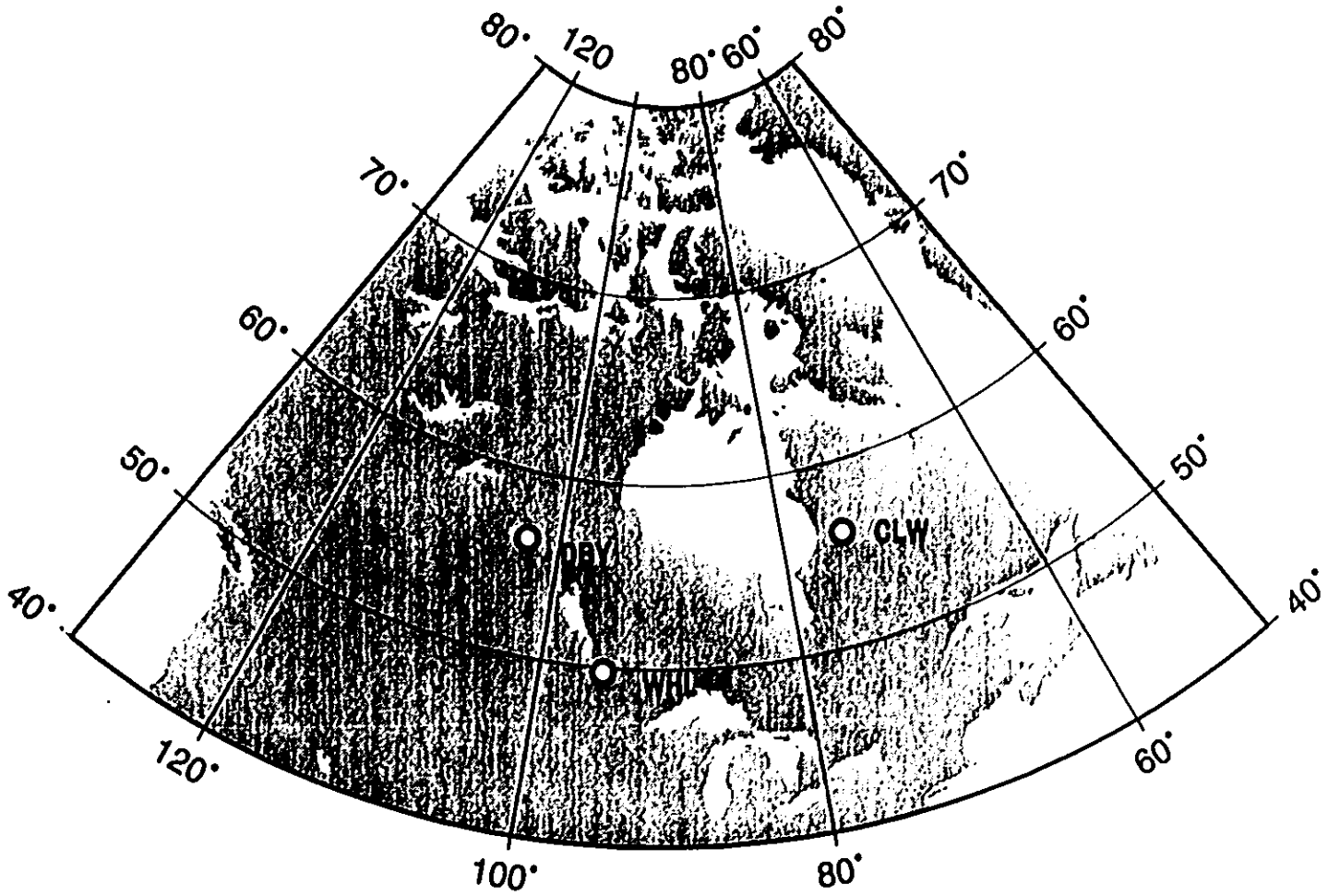

Figure 1. Location map of the three impact structures studied. Deep Bay (DBY), West Hawk Lake (WHL), and Clearwater Lakes (CLW).

1.1 CRUSTAL MAGNETIZATION

Magnetic anomalies on the surface of the Earth are formed by variations in the magnetization of crustal rocks, those rocks that exist at temperatures below the Curie isotherm for magnetic carrier minerals, and can be magnetized in two ways (eg. Blakely, 1995). Rocks can acquire a natural remanent magnetization (NRM) as their magnetic carrier minerals cool below their respective Curie temperatures after formation. For example, magnetite in a cooling lava flow will acquire a natural remanent magnetization in the direction of the geomagnetic field as it cools below 580 - 600°C. This magnetization, which can be carried by members of the iron-titanium oxide group (titanomagnetites, hematites) and some sulphides (pyrrhotite), represent the permanent magnetization in a rock body. The NRM can be altered or overprinted by subsequent reheating during metamorphism or tectonism, and by chemical alteration (Butler, 1992).

The second cause of crustal magnetization is the ability of ferromagnetic, paramagnetic and diamagnetic minerals to acquire a magnetization in the presence of an external magnetic field. Thus rocks containing iron silicates such as micas, pyroxenes and olivine, will acquire a magnetization induced by the Earth's magnetic field (Butler, 1992; Tarling & Hrouda, 1993). This property is referred to as magnetic susceptibility (κ) and is a dimensionless quantity, quoted in SI units. Ferromagnetic minerals also contribute to magnetic susceptibility, and if present in sufficient quantities (> 1-2 %), will dominate the magnetic susceptibility of the rock in question. Magnetic susceptibility is anisotropic in minerals that do not have cubic symmetry, due to crystalline anisotropy, and is usually anisotropic in cubic magnetite due to shape anisotropy of the magnetite grain, which is seldom perfectly equidimensional. Consequently, the magnetic susceptibility is not

the same in all directions. This anisotropy of magnetic susceptibility (AMS) can be represented as a second-order tensor, and as an ellipsoid, with the three principle susceptibilities ($k_1 > k_2 > k_3$) forming the principle axes of the ellipsoid. The AMS of a rock usually does not influence the magnetic anomaly (eg. Florio *et al.* 1993), consequently only bulk magnetic susceptibilities are used for anomaly modelling. However, the orientation of the AMS ellipsoid, and the degree of anisotropy (P), may be related to the strain ellipsoid of the rock, and important information regarding the strain history of the rock can be determined from the AMS ellipsoid (Tarling & Hrouda, 1993).

The two components of crustal magnetization, NRM and magnetic susceptibility, are related through a simple ratio called the Königsberger Ratio, or Q. This ratio is the NRM intensity divided by the bulk magnetic susceptibility (converted to induced intensity). A Q value of 5 would indicate that the NRM is dominating the crustal magnetic field, while Q values approaching 0.1 indicate that induced magnetization (susceptibility) is dominant. Table 1 summarizes the magnetic parameters, symbols, and units used in this study.

TABLE 1. SYMBOLS AND UNITS FOR MAGNETIC VARIABLES

MAGNETIC VARIABLE	SYMBOL	DEFINITION	UNITS
Susceptibility	κ	Magnetization acquired in an applied field.	dimensionless (SI)
Principle Susceptibilities	k_1, k_2, k_3	1=maximum, 2=intermediate, 3=minimum. Three axes of susceptibility tensor ellipsoid.	defined by susceptibility and direction
Anisotropy of magnetic susceptibility	P	$= k_1/k_3$ Degree of anisotropy.	dimensionless
Remanent Magnetization (NRM)	J	Naturally occurring magnetization from magnetic minerals. Has both intensity and direction.	A/m (Amperes/meter)
Magnetic Field	H	Aeromagnetic data collected at 300 m flight height. Crustal magnetic field due to remanence and susceptibility of rocks.	T (Tesla)

1.2 IMPACT CRATERING: THE GEOLOGIC RECORD

Currently, there are about 150 terrestrial impact structures known (Grieve *et al*, 1995). The distribution of impact structures on the surface of the Earth is highly biased towards well studied shield areas in the northern hemisphere, particularly Canada, Fennoscandia, and Russia. In the southern hemisphere, only Australia has a large number of known impact structures. These biases reflect our relative ignorance of other areas in the world, such as South America and Africa, rather than a primary cratering distribution. Few structures are known on the ocean floors, despite the larger surface area of the Earth that is covered by oceans. Again, this reflects our ignorance of the structural features on the bottom of the ocean (Grieve *et al*, 1995), as well as the relative youth of oceanic crust (<200 Ma).

Impact structures on the Earth are subject to the effects of wind, water and glacial erosion, tectonic alteration and destruction, and burial. Consequently, terrestrial impact structures are considerably more difficult to find and identify than their counterparts on the other terrestrial planets and moons. A second bias that arises from the above effects is the erasure of older structures. Known impact structures are not only biased in terms of geographic location, but are also biased towards impacts which are young enough to have avoided significant erosional, burial, or tectonic processes (Grieve *et al*, 1995).

The detection of impact structures is not only of geological or intellectual interest, but is also an economic one. Approximately 25% of the known terrestrial impact structures are associated with some kind of economic resource, and about 12% are currently exploited for mineral or hydrocarbon resources (Grieve & Masaitis, 1994). For example, the Sudbury impact

structure contains one of the most significant nickel deposits in the world. Vredefort, South Africa, hosts unique alluvial gold deposits, while structures formed in sedimentary rocks, such as Ames, Oklahoma, can provide structural traps for oil and gas (Grieve & Masaitis, 1994).

The detection of impact structures is also important for determining the cratering rate over geologic history, and for the study of cratering mechanics. Accurate determination of the rate of impact on the Earth, for large objects producing structures of 20 km or more, is essential in assessing the threat to human civilization from an impact event (Grieve & Pesonen, 1992).

1.3 MORPHOLOGY AND GEOPHYSICS OF IMPACT STRUCTURES

1.3.1 CRATERING MECHANICS AND RESULTING MORPHOLOGIES

Impact structures are found in one of two morphological types, simple and complex. The size of the impact structure is a function of the mass of the impacting object, although target rock properties and impactor velocity also influence the final type and size of the impact structure (Grieve and Pesonen, 1992). Based on analysis of terrestrial impact structures, simple craters have diameters up to 2 km in sedimentary rocks, and up to 4 km in crystalline rocks (Dence, 1972). Above these diameters, craters take a complex form.

Simple craters have bowl shaped forms, with raised and fractured rims. The best known example of a simple crater is the 1.2 km diameter Meteor or Barringer crater in Arizona. Drilling at Meteor Crater (and other simple craters) reveals that the apparent crater floor is underlain by a breccia lens of autochthonous breccia and varying amounts of melted target rock (Fig. 2). Below this breccia lens lies the true bottom of the structure, shocked and fractured parautochthonous

target rocks.

The formation of a simple crater requires the initial creation of a transient cavity in the target rock, produced by the sudden release of energy by the impacting object. This energy is released as kinetic energy, and takes both mechanical and thermal forms (eg. Melosh, 1989). The release of energy creates a shock wave that imparts a high velocity to the target material, as well as thermal energy. The release of the impactors' kinetic energy thus excavates a parabolic cavity with a depth of about one-third its diameter. This occurs in a time interval of about 10 seconds (Melosh, 1989). During the late stages of cavity growth, the walls of the cavity, lined with melted and shocked target material, collapse inwards due to the force of gravity acting on the unconsolidated breccia and melt. The collapse enlarges the diameter of the transient cavity, and fills the final crater with breccia and melt from the transient cavity wall. Below the lens of breccia and melt lies the true crater floor, and consists of fractured target rocks (Fig. 2). Peak shock pressures of 25 GPa have been recorded at the center of the true crater floor (Grieve and Pesonen, 1992).

The final morphology of simple craters has been modelled through detailed studies at 7 impact structures. These studies define structural relationships for simple craters as:

$$d_a = 0.13\ D^{1.06}$$

$$d_t = 0.28\ D^{1.02}$$

where d_a and d_t are apparent and true crater depth, and D is crater diameter. Depths are defined as the distance from the original ground surface to the top and bottom of the breccia lens respectively (Grieve and Pesonen, 1992).

Complex structures are larger, and although they are broadly bowl shaped, their centres have undergone a downward displacement of target rocks followed by rebound (Fig. 2). These structures are thus characterized by central uplifts of rebounded, shocked target rocks occurring as a central peak or ring (Grieve and Pesonen, 1992). The surrounding annular depression produced by the impact is filled with allochthonous breccia and melt rocks (Melosh, 1989; Pilkington & Grieve, 1992). Below the crater floor is a zone of fractured, parautochthonous target rocks. The rim is characterized by faulted blocks which have been stratigraphically down-dropped. The volume of impact melt rocks is significantly greater in the larger complex craters. For example, the impact melt sheet at Manicouagan has been estimated to have had a volume of about 1000 km^3 (Phinney and Simonds, 1977), prior to subsequent erosion.

The mechanics of formation of complex craters are similar to those for simple craters, however, the collapse of the transient cavity at complex craters is more substantial than at simple craters. This is due to the strength of the target rocks, and the much larger transient cavity that is produced by complex crater forming impacts. Studies of complex craters in sedimentary and crystalline rocks have produced different morphological relationships. For apparent depth, these are:

$$d_a = 0.12\ D^{0.30}$$ for sedimentary targets, and

$$d_a = 0.15\ D^{0.43}$$ for crystalline targets.

The difference in strength becomes important in large impacts due to the much larger transient cavity formed, and the inability of the surrounding target rocks to retain their tensile strength under the transient shock impulse of the impact (Grieve and Pesonen, 1992). The uplifted rocks in the

centre of the complex crater have been subject to very high shock levels (30 - 40 GPa), and have behaved hydrodynamically with little to no tensile strength (Melosh, 1989; Grieve and Pesonen, 1992). Where the subsurface stratigraphy is known, the amount of structural uplift (SU) in the centres of complex craters has been determined to be:

$$SU = 0.086\ D^{1.03}$$

where D is the crater diameter and SU is the amount of uplift undergone by the deepest lithology exposed at the surface (Pilkington and Grieve, 1992). For structures like Manicouagan, SU equals 9.5 km, a large portion of the upper crust (Grieve and Pesonen, 1992).

For both simple and complex craters, the impactor energy is distributed as both mechanical and thermal energy (eg. Melosh, 1989). Thermal energy melts and vaporizes both the impacting object and variable amounts of target material. Mechanical energy produces brecciation, fracturing, faulting and structural uplift. Mechanical energy also expresses itself in the form of the impact shock wave. This shock wave produces transient pressures in the gigaPascal range, and is characteristically expressed by so-called shock metamorphic effects in silicate minerals. These features include the formation of planar deformation features (PDFs) in silicates, kink bands in micaceous minerals, and the formation of maskelynite (isotropic melt glass) in feldspars (eg. Stöffler, 1972, 1974). Shock metamorphic effects are due to dislocations in silicate crystal structures by compression, and by shock heating resulting in partial to complete melting of mineral grains. Shock is defined *sensu stricto* as the ability of the transient shock wave to produce optically visible changes in silicate minerals. At pressures too low to produce visible changes, the shock wave is termed a transient stress wave.

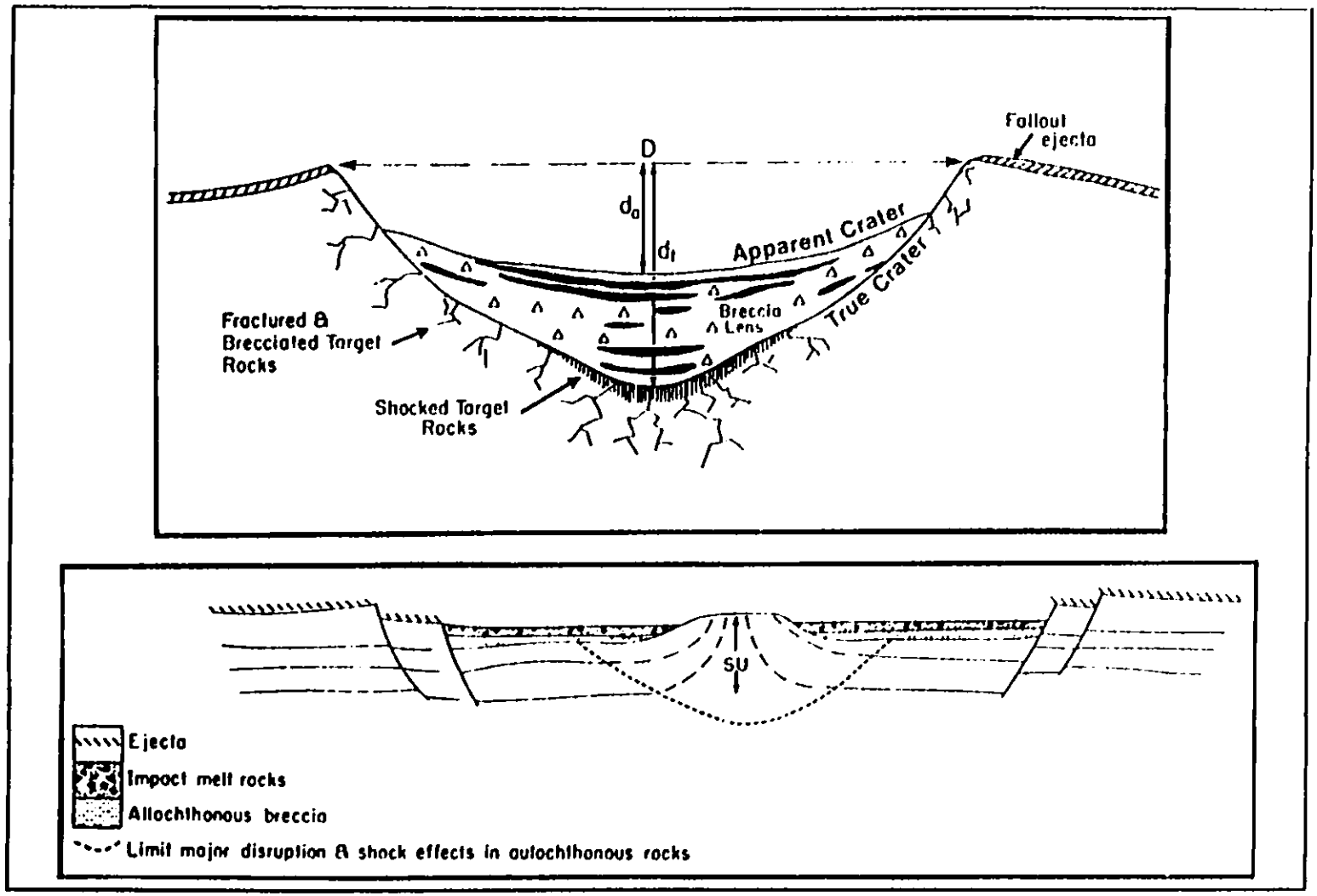

Figure 2. Schematic diagrams of impact structure morphologies. The simple crater (top) forms a bowl shaped structure partially filled with breccia and melt lenses. The complex structure (bottom) is characterized by down faulted blocks along the rims, and a central uplift. The amount of structural uplift (SU) is about 10% of the crater diameter. From Pilkington and Grieve (1992).

1.3.2. GRAVITY SIGNATURE

Impact structures, both simple and complex, are characterized by circular residual gravity anomalies. The anomaly is produced by several factors depending on the size of the structure; infill of the crater by lower density sediments and slightly lower density melt sheets, and particularly by fracturing and brecciation of the target rocks. The gravity low extends to or just slightly beyond the crater rim. Gravity modelling based on density differences between the crater fill and the surrounding country rocks, and the morphological relationships between diameter and depth discussed in the last section (Grieve & Pesonen, 1992), produces modelled anomalies that agree well with the observed gravity anomalies over impact structures (Pilkington & Grieve, 1992). This suggests that the morphological relationships for impact structure size are reasonably accurate, and can be used for magnetic modelling as well.

1.3.3. MAGNETIC SIGNATURE

The magnetic signatures of impact structures are considerably more complex than the gravity signatures. The principal characteristic is a reduced magnetization leading to a magnetic anomaly low (Dabizha & Fedynsky, 1975; Pilkington & Grieve, 1992). This low can range in amplitude from subdued (10 - 100 nT) to very high (100 - 1,000 nT). These lows are particularly evident in crystalline rocks where they can truncate or disrupt regional magnetic lineaments (Pilkington & Grieve, 1992). Large complex structures, generally with diameters greater than 40 kilometres, also have a localized large amplitude magnetic high near the centre of the central uplift of up to 1,000 nT (Pilkington & Grieve, 1992).

The origins of the localized magnetic anomaly highs in complex craters can be produced by several mechanisms. These include the acquisition of a thermoremanent magnetization (TRM) by impact breccias (Pohl *et al*, 1977) and melt rocks (Henkel, 1982), the acquisition of a chemical remanent magnetization (CRM) formed by alteration (Coles & Clark, 1982), and the acquisition of both thermal and chemical remagnetizations (TCRM) such as that found at Lappajärvi, Finland, by Pesonen, *et al* (1992). Magnetic minerals such as magnetite can also be formed by shock decomposition of iron silicates (Feldman, 1995).

The causes of the principal anomaly, the magnetic low, are more complex. Experimental and field studies have shown that shock can reduce the levels of induced (Kumar & Ward, 1963) and remanent magnetization intensity (Cisowski & Fuller, 1978; Robertson & Roy, 1979; Pohl, 1994) in target materials. High post-shock temperatures (>1000°C), followed by rapid cooling can result in the formation of paramagnetic impact glasses (Pohl, 1971), while later low temperature alteration effects due to the movement of fluids through fractures and breccias produced by the impact event can lead to the destruction of magnetic phases (Henkel & Guzman, 1977) or their replacement with minerals of lower susceptibility (eg. magnetite oxidizing to haematite). In uneroded structures, sedimentary infill and/or burial is normally non-magnetic. The random orientation of magnetization vectors within impact breccia deposits can also contribute to a reduced magnetic field strength over impact structures (Beals *et al*, 1963). Finally, highly oxidizing post-impact conditions noted at structures such as Manicouagan, Canada (Morris *et al*, 1995) and Siljan, Sweden (AlDahan, 1990), lead to the conversion of magnetite to lower remanent magnetization intensity haematite in impact lithologies, further reducing the natural

remanent magnetization and susceptibility level of the target rocks.

Previous petrophysical studies have found a systematic reduction in both magnetic susceptibility and natural remanent magnetization (NRM) intensity in post-impact lithologies when compared to their pre-impact equivalents outside of the impact structures. For example, at Lappajärvi, Finland, both melt rocks and impact breccias show lower susceptibilities and natural remanent magnetizations than country rocks (Kukkonen *et al*, 1992). Masaitis, *et al* (1975) reported that susceptibilities of gneisses within allochthonous breccia deposits of the Popigai structure, Russia, were 1.2-2.4 x 10^{-4} SI, two orders of magnitude lower than those outside the structure (2.4-3.4 x 10^{-2} SI). No NRM values were reported. These authors noted that such changes were present even in samples showing no noticeable petrographic transformations of the magnetic carrier phases. Plado *et al* (1966) have recorded both reduced susceptibilities and NRM intensities in granites from inside the Kärdla structure, Finland, compared to those outside.

Previous studies have concentrated on the petrophysical properties of exposed surface rocks, limiting our knowledge of the causes of magnetic anomaly lows to two dimensions. The availability of drill core from several Canadian impact structures permitted, for the first time, a detailed petrophysical study of impact rocks in the third (vertical) dimension, allowing modelling of the anomalies to be better constrained.

2. METHODOLOGY

2.1 MEASUREMENT OF MAGNETIC SUSCEPTIBILITY AND AMS

Drill core from the three impact structures studied was initially measured for magnetic susceptibility with a hand-held KT-5 Exploranium instrument with a sensitivity of 10^{-3} SI. Measurements were taken every one to two metres along the length of the core. The values were corrected for the cylindrical shape and 3.6 cm diameter of the core by multiplying them by a factor of two (M.D. Thomas, pers. com., 1994).

Lithologically representative samples of 10 to 20 cm length were selected for more detailed study. The core samples were cut and re-cored on a drill press to 25 mm diameter and 25 mm length to provide standard size samples (~ 300 in total) for measurements in susceptibility bridges. Samples were measured for their anisotropy of magnetic susceptibility (AMS) on a six-position Sapphire Instruments bridge at the Geological Survey of Canada. Samples with very weak susceptibilities were measured on a fifteen-position Geophyzika KLY-2 Kappabridge at the University of Ottawa. Measured values were analysed and displayed through the use of the AMSDbase program at the GSC.

2.2 MEASUREMENT OF NATURAL REMANENT MAGNETIZATION

The same ~ 300 samples were also measured for NRM on a four-position Geophyzika JR-4 spinner magnetometer. Two samples with NRM intensities higher than the JR-4 machine capability were measured on a six-position Schönstedt digital spinner magnetometer (DSM-1). Samples subjected to alternating field and thermal demagnetization were measured on the JR-4.

Values measured were analysed and displayed through the use of the RemDbase program at the GSC.

2.3 DEMAGNETIZATION PROCEDURES

Alternating field demagnetization was done on selected samples from the Clearwater structures in order to determine why drill core from the two impacts exhibited different NRM intensity and inclination versus depth profiles, despite the impacts occurring in the same rock types at the same time. Demagnetization also permitted the determination of the coercivity of the magnetic carrier minerals, and the isolation of any multiple remanences. AF demagnetization was done on a Schönstedt AF demagnetizer up to 100 mT. This procedure subjects the sample to an alternating field, the peak value of which is predetermined. Samples are demagnetized at each preset step in three orthogonal positions. This field randomizes the magnetic vectors in mineral grains with coercivities less than the peak AF field (Butler, 1992). Consequently, NRM intensity decreases with increasing field strength, and multiple remanences, held by grains of different coercivities, can be resolved.

Thermal demagnetization was done using a large capacity furnace (Roy *et al*, 1972), built at the Earth Physics Branch Palaeomagnetic Laboratory (now GSC). Samples were heated to pre-determined temperatures and allowed to cool in the presence of a zero magnetic field environment. Heating and subsequent cooling in a zero magnetic field allows grains with blocking temperatures lower than the maximum temperature to acquire a random magnetization in the zero field. Consequently, the NRM carried by these grains is erased (Butler, 1992).

Display of NRM demagnetization data is done with the use of equal-area stereonets, and plots of NRM intensity versus temperature or AF field. The stereonet projection (where 90° vertical is at the centre and 0° horizontal is along the circumference), allows the inclination and declination of the NRM and demagnetization vectors to be displayed in a geographically meaningful way. The remanence intensity spectra curves allow for the determination of the coercivity, type of NRM, and Curie (blocking) temperatures of the magnetic carriers.

2.4 MAGNETIC MODELLING

Magnetic data collected from the drill cores was used to constrain magnetic modelling of the anomalies present over the impact structures, in order to determine whether the measured magnetic values from the drill cores would account for the observed magnetic lows. Modelling was done using the GSC program GM-2D. Forward modelling of magnetic anomalies requires the graphical construction of user-defined bodies of rock with well constrained magnetic parameters (cf. Blakely, 1995). Manipulation of the size and orientation of these bodies produces in turn a calculated magnetic anomaly profile in two dimensions. Two dimensional modelling of three dimensional bodies introduces an error of 5-10% in the calculated magnetic profiles (M. Pilkington, pers com, 1996). Ground truth measurements of rocks from the modelled crater bodies, and constraints on the size and shape of the impact structures (Section 1.3.1), avoid the uniqueness problems associated with forward modelling (cf. Blakely, 1995).

The bodies in this study are defined by the morphological relationships for simple and complex craters determined by Grieve and Pesonen (1992), discussed in Section 1.3.1. The

magnetic parameters assigned to the modelled crater bodies are those determined by measurements from their respective drill cores. The magnetic parameters assigned to the regional rocks outside of the crater body are determined by modelling regional magnetic anomaly highs in order to determine the maximum possible pre-impact magnetization in the target rocks. The difference between the magnetic parameters for the magnetic anomaly highs and the measured magnetic parameters determined for the impact structures, is used to calculate a contrast parameter between the modelled crater form and the surrounding rocks. Calculation of the resulting magnetic anomaly produces a magnetic low which can then be compared with the observed field over the impact structures. The use of magnetic data from drill holes allows the anomaly modelling to be well constrained within the impact structures at depth. Deviation between the calculated and observed anomalies requires additional impact related factors to be considered in the formation of the magnetic anomaly lows. Magnetic modelling results are presented in Chapter 6.

3. THE DEEP BAY IMPACT STRUCTURE

3.1 LOCATION AND GEOLOGICAL SETTING

The Deep Bay structure in Saskatchewan (56° 24′ N, 102° 59′ W), corresponds to a large circular lake at the southern end of Reindeer Lake (Figure 3). Deep Bay has a diameter of 13 km, and was excavated in several pelitic gneissic units of the Churchill Province. Target lithologies consist of Proterozoic biotite-garnet-graphite gneissic assemblages, with lesser amounts of granitic and migmatitic rocks (Innes *et al*, 1964; Johnston, 1982). Sedimentary infill consists of well bedded black shales and unconsolidated glacial sand and boulders. Micropalaeontology suggests that the shales are of Cretaceous age (Johnston, 1982). The age of the Deep Bay impact is estimated at 100 ± 50 Ma (Grieve *et al*, 1995), based on the degree of erosion and the presence of Cretaceous sediments in the structure.

3.2 STRUCTURE AND DRILL CORE CHARACTERISTICS

Deep Bay is a small complex crater with a submerged central uplift. Average depth to the sediments is 150 m, with a maximum depth of 216 m, contrasting with the average depth of 30 m found in the Reindeer Lake region. The central uplift is flanked by altered breccia deposits and post-impact sediments. The flanks of the structure consist of eroded and fractured country rocks forming a rim that rises about 81 m from the surface of the lake (Innes *et al* 1964). Along the eastern and southeastern shore the rim rises to a height of 120 m. Granitic rocks along the shoreline show intense fracturing and shattering. The Deep Bay structure also truncates northeasterly striking structural features such as synclinal folds (Innes *et al*, 1964). The structure

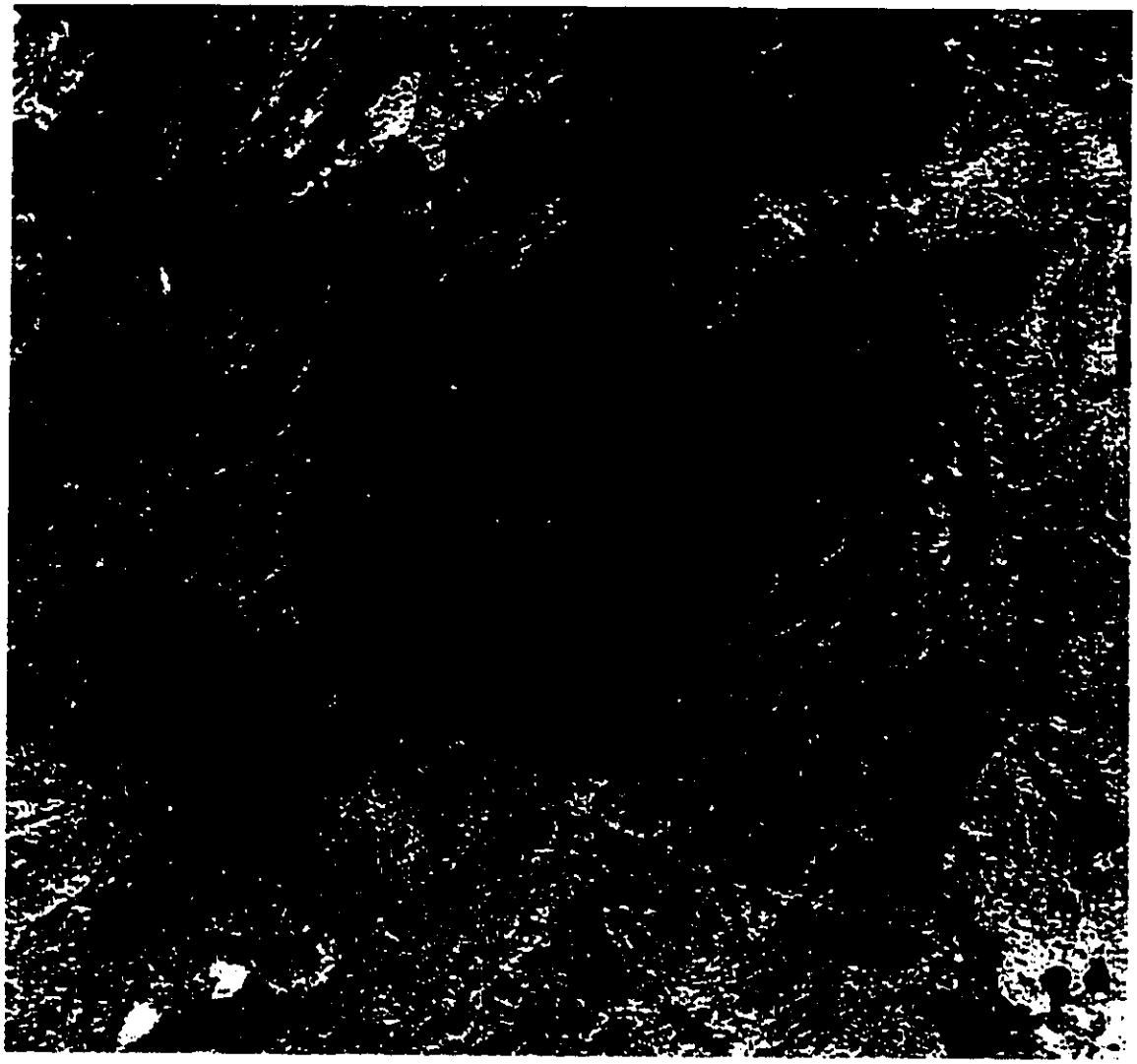

Figure 3. Aerial photo mosaic of the Deep Bay Structure. Its near perfect circular form and greater depth suggested an impact origin. Photo is ~30x30 km. North is to the top. Image courtesy of GSC.

was drilled in the early 1960's during the Dominion Observatory's impact structure research program, resulting in the collection of about 400 m of core. Hole 66-1 was placed on the flank of the central uplift, while hole 62-1A was placed near the structure rim.

3.3 MAGNETIC ANOMALY PROFILE

Aeromagnetic data collected over the Deep Bay structure show a subdued, smooth character, with values of >100 nT below the regional field value (Figure 4). Truncation of linear anomalies, related to northeasterly trending structures in the gneisses, by the impact structure is particularly evident in the northeast part of the bay (Figure 4; Innes et al, 1964). Gridded profile data, taken in four transects across the structure (Figure 5) illustrate the magnetic anomaly low, with some transects exhibiting a magnetic low associated with the structure of < -200 nT. Location of drill holes 62-1A and 66-1 are marked in Figure 4.

3.4 MAGNETIC SUSCEPTIBILITY AND AMS

Figure 6 shows the magnetic susceptibility values from hole 62-1A, taken at 1-2 m intervals, within the brecciated and fractured basement rocks of the crater rim. The target lithology here is medium grained quartz-biotite-plagioclase gneiss, and varies in texture from occasionally fractured to highly brecciated with variable amounts of fine-grained matrix. Values are uniformly around 3×10^{-4} SI, even though there is considerable variation in the degree of fracturing and brecciation.

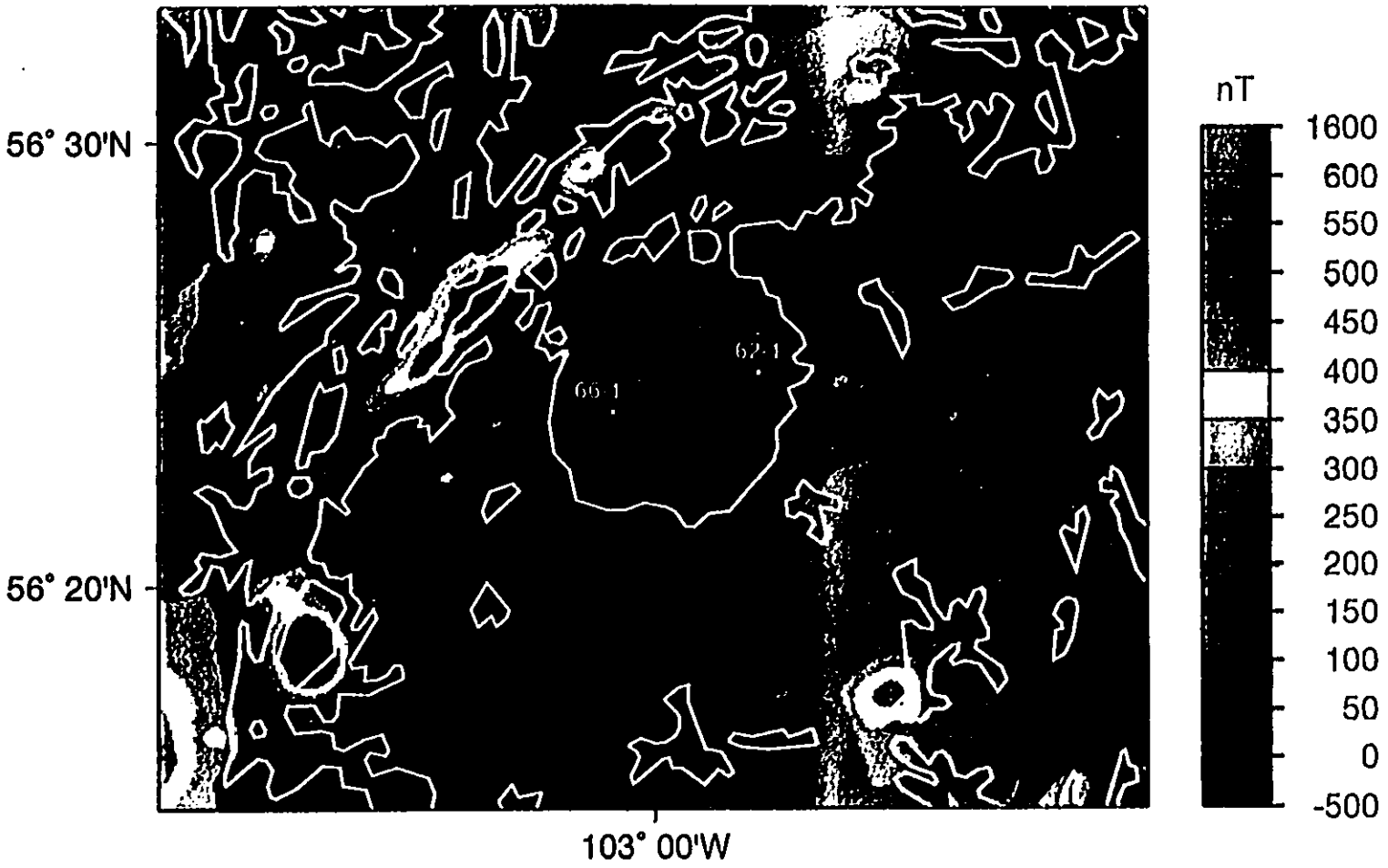

Figure 4. Magnetic anomaly map of Deep Bay. The structure appears to truncate northeasterly trending magnetic lineaments in the western part of the bay. Drill holes 62-1(A) and 66-1 marked. 500 m grid spacing. Image courtesy GSC

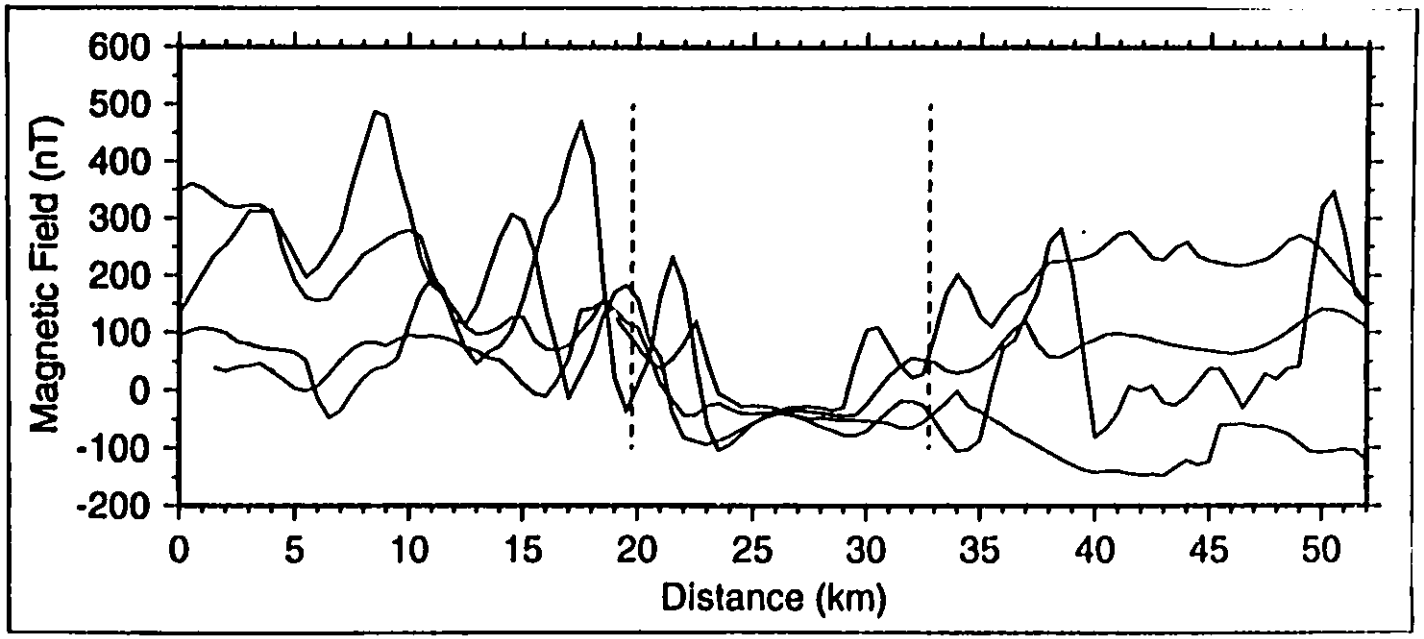

Figure 5. Gridded magnetic profile data from four transects across the Deep Bay structure. Transects are taken radially across the structure at 000°, 45°, 90° and 135° strike. The structure (dashed lines) defines a subdued zone in an area of variable magnetic intensities. Courtesy M. Pilkington, GSC.

AMS measurements on selected samples agree with the bulk susceptibility values noted above. The degree of anisotropy (P) rarely exceeds 1.1, and principle axes directions and inclinations are scattered, reflecting the brecciated nature of the drill core lithology.

Hole 66-1 (not shown) consisted of friable, well laminated shales (164–436 m) overlying highly altered breccia (436-507 m). Susceptibility values were consistent throughout the core at $2x10^{-4}$ SI in the shales and $3\text{-}6x10^{-4}$ SI in the breccia. The consistency in the susceptibility values in the breccia is surprising given the highly variable appearance and wide range of shock levels found in the breccia layer (Dence et al, 1968). AMS measurements were not performed on this hole due to the highly friable nature of the core, which made re-coring for instrumental analysis impossible.

3.5 NATURAL REMANENT MAGNETIZATION

Drill hole 62-1A shows natural remanent magnetization (NRM) intensities in the 1-10 mA/m range, with peak values up to 100 mA/m (Figure 6) corresponding to narrow zones of breccia and rock flour. NRM inclinations appear variable down to 250 m depth, where they stabilize at values of 60° or steeper. Since the susceptibilities for hole 62-1A are so uniform, variations in Q simply reflect fluctuations in NRM intensity (Figure 6). An average value of 0.2 is apparent, despite occasional NRM intensities producing Q values >1. Induced magnetization therefore is dominating the observed magnetic field.

Hole 66-1 was not measured for NRM due to the difficulties in re-coring noted above.

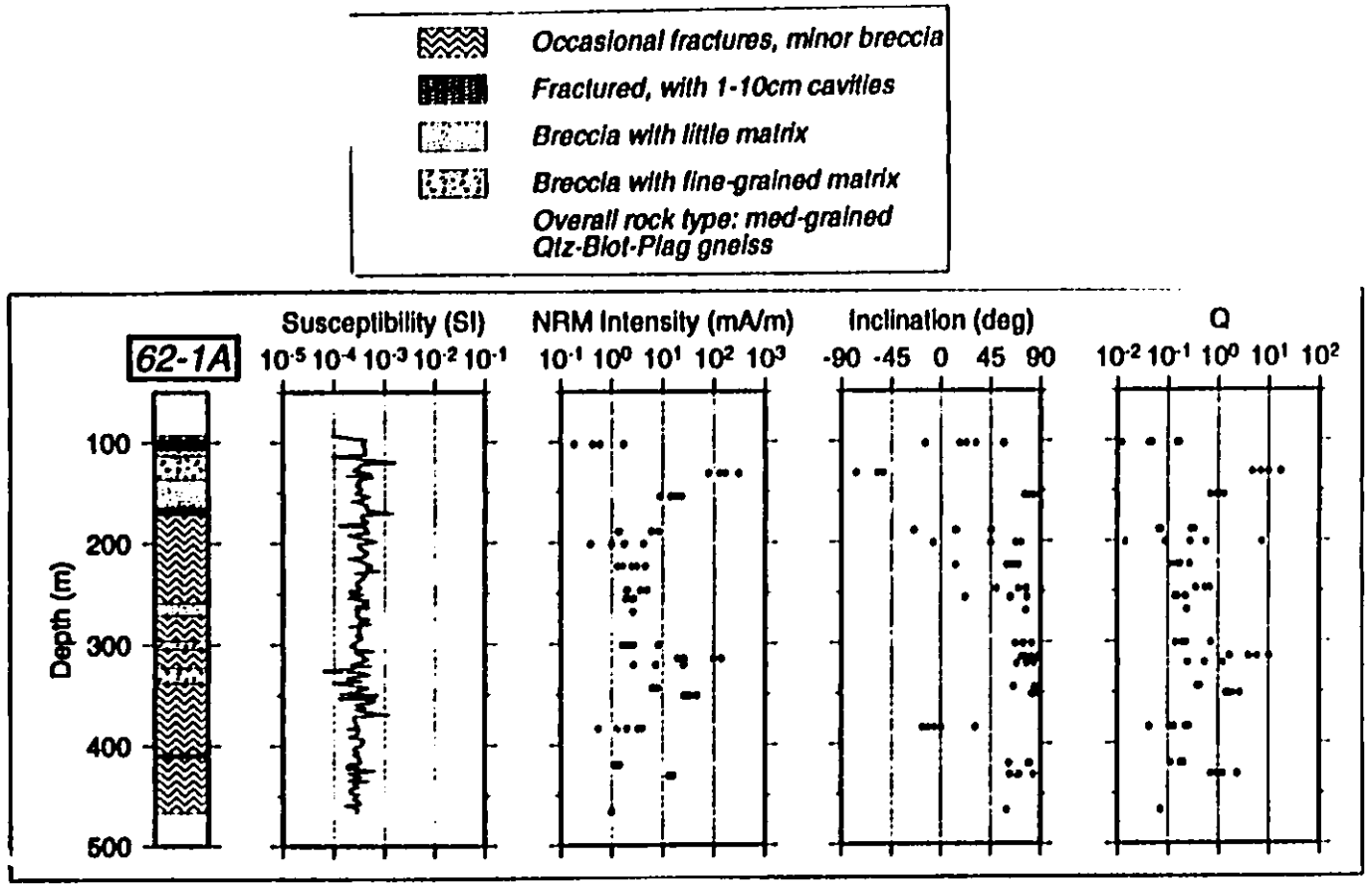

Figure 6. Deep Bay. Lithologies and magnetic parameters for core from hole 62-1A. Susceptibilities are uniform throughout, while NRM intensities and inclinations vary considerably. Lithologies after Innes *et al*, (1964).

4. THE WEST HAWK LAKE IMPACT STRUCTURE

4.1 LOCATION AND GEOLOGIC SETTING

The West Hawk Lake structure in Manitoba (49° 46′ N, 95° 11′ W), is a small irregularly shaped lake with a diameter of 2.5 km (Figure 7). West Hawk was excavated in Archean basaltic-andesitic metavolcanic rocks of the Superior Province in the south, and Archean quartz-mica schists in the north (Short, 1970). The crater is partially infilled with post-impact sediments and glacial drift. The estimated age of West Hawk is 100 ± 50 Ma, based again on the degree of erosion of the structure rim, and amount of sedimentary infill.

4.2 STRUCTURE AND DRILL CORE CHARACTERISTICS

West Hawk is a simple crater, characterized by a bowl shaped depression filled with an allocthonous breccia lens overlain by post-impact sediments. Drilling by the Dominion Observatory during the 1960's resulted in the placement of three holes and > 1 km of recovered core (Halliday and Griffin, 1966; 1967). Figure 8 shows the locations of the drill holes 65-1, 66-1, and 66-3. Hole 65-1 encountered altered breccia from 202 to 521 m depth, and fractured basement from 521 to 782 m depth (Figure 10). Only 4 m of sediments were sampled in this hole (198 to 202 m).

Hole 66-3 passed through glacial drift, boulders and sediments to a depth of 200 m. Below this, felsic and mafic breccias were encountered to a depth of 380 m (Figure 11). Hole 66-1 is located near the crater rim, and intersected glacial till (to 128 m) and fractured andesitic basement rocks to a depth of 260 m (Figure 11).

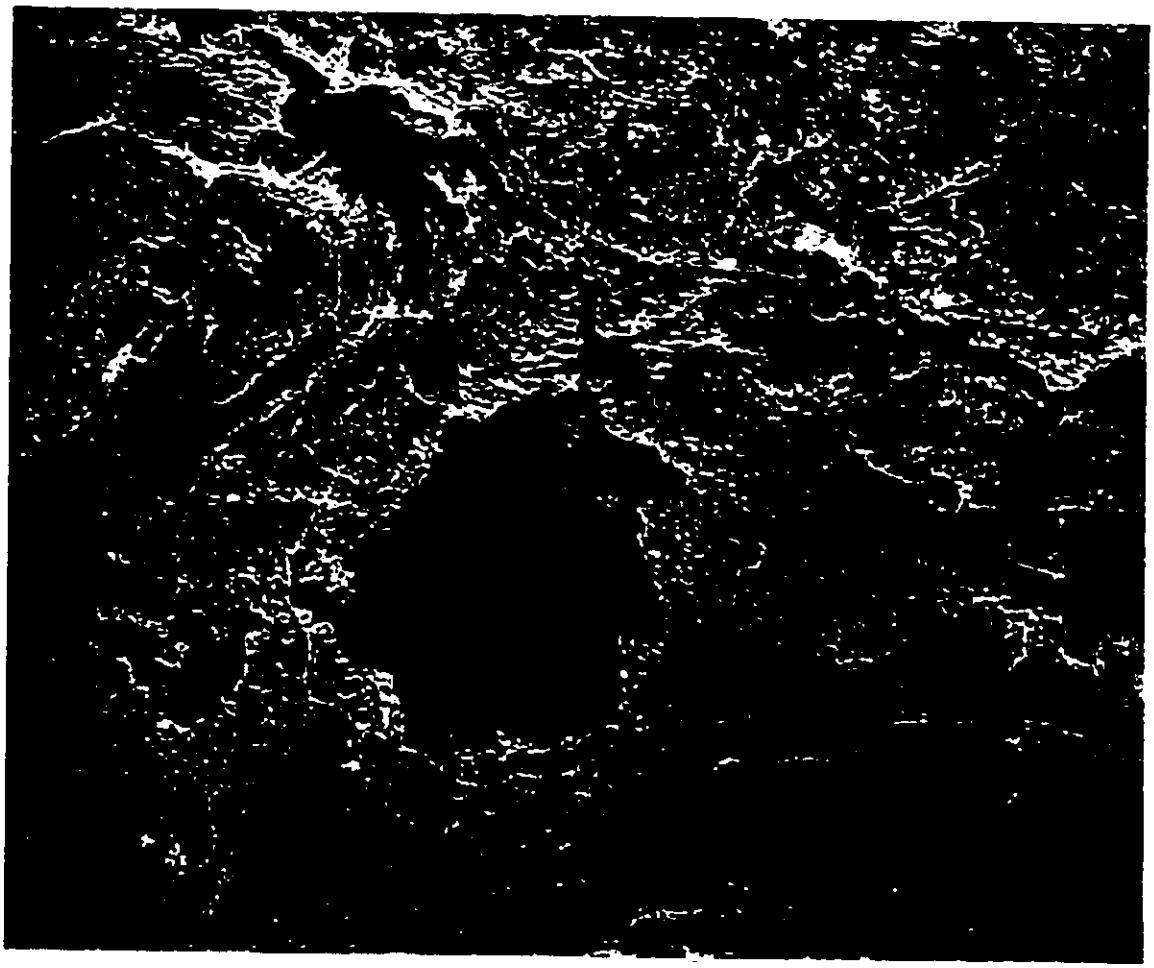

Figure 7. Aerial photograph of the West Hawk Lake structure. With a diameter of 2.5 km, West Hawk is a simple crater. Photo is ~18x20 km. North is to the top. Image courtesy of GSC.

4.3 MAGNETIC ANOMALY PROFILE

Aeromagnetic data collected at a 300 m flight height indicate a >100 nT anomaly low associated with the structure (Figure 8). The magnetic low is more clearly seen in ground magnetic data, which defines an average magnetic low of about 250 nT (Clark, 1980). Gridded magnetic data from four traverses across the structure converge at an intense, localized magnetic low of -200 nT against a background of fluctuating field strengths (Figure 9).

4.4 MAGNETIC SUSCEPTIBILITY AND AMS

The sediments in hole 65-1, the uppermost of which is glacial drift, show the lowest susceptibility values ($< 2x10^{-4}$ SI) of the whole core. The felsic breccia sections show susceptibility values of about $3x10^{-4}$ SI, and the mafic breccia sections show slightly higher values of about $7x10^{-4}$ SI. A peak value of $>10^{-2}$ SI corresponds to a haematized layer in the mafic breccia (Figure 10). Fractured basement (below 521 m) consisting of interbedded greenstone and quartz-mica schists, shows a slight increase in susceptibility from 3 to $6x10^{-4}$SI with depth. Trends in the core densities, reflecting felsic versus mafic lithologies, follow the susceptibility levels, with mafic breccias and basement rocks having the highest values (Halliday and Griffin, 1967).

Hole 66-3 exhibited the highest susceptibilities in association with glacial boulders (Figure 11) of $8x10^{-2}$ to $8x10^{-1}$ SI. Below 187 m, sediments (187-200 m) and upper breccia rocks show susceptibilities of about $3x10^{-4}$ down to 230 m. An increase to susceptibility values of about 10^{-3} SI coincides with a density increase of 0.3 g/cc (Halliday and Griffin, 1967). The andesitic breccias of hole 66-3 show higher susceptibilities than do the breccias found in hole 65-1 (Figure

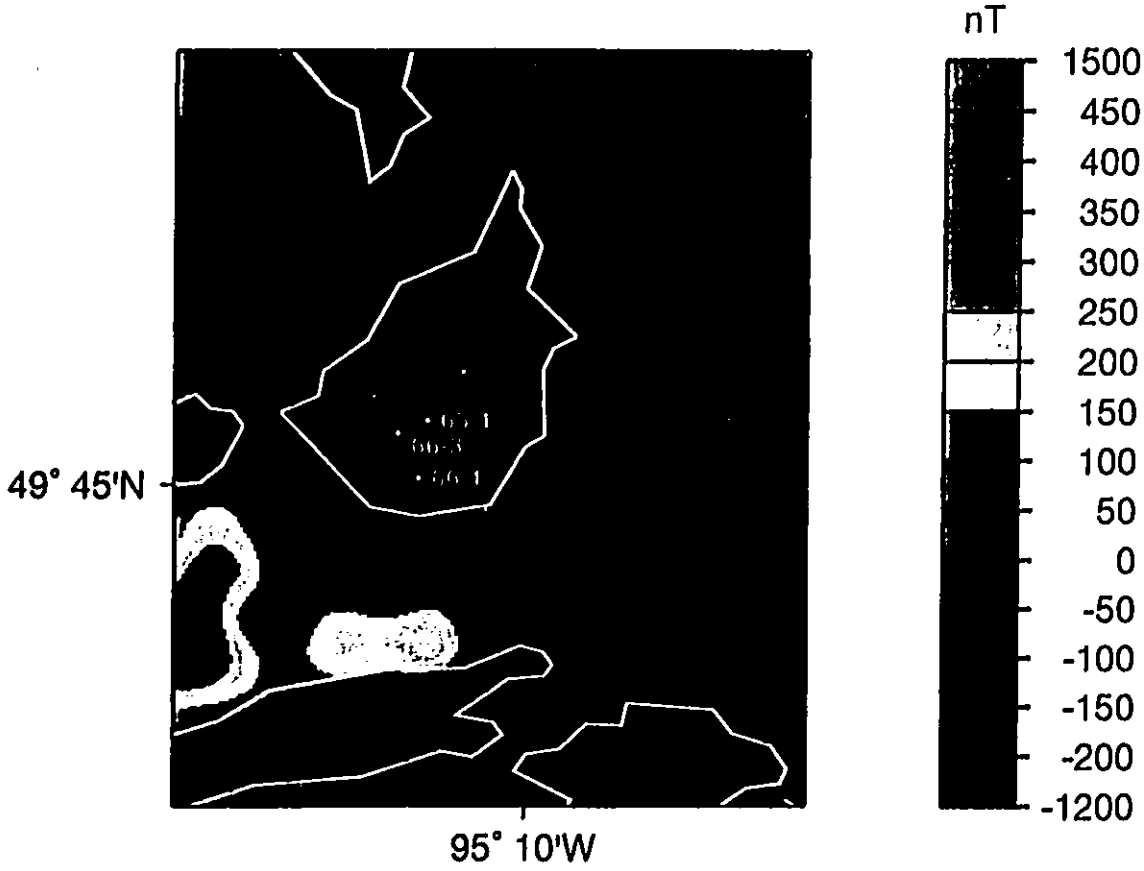

Figure 8. Magnetic anomaly contour map of West Hawk Lake. Drill holes 65-1, 66-1 and 66-3 are marked. Structure outline in white. Courtesy GSC.

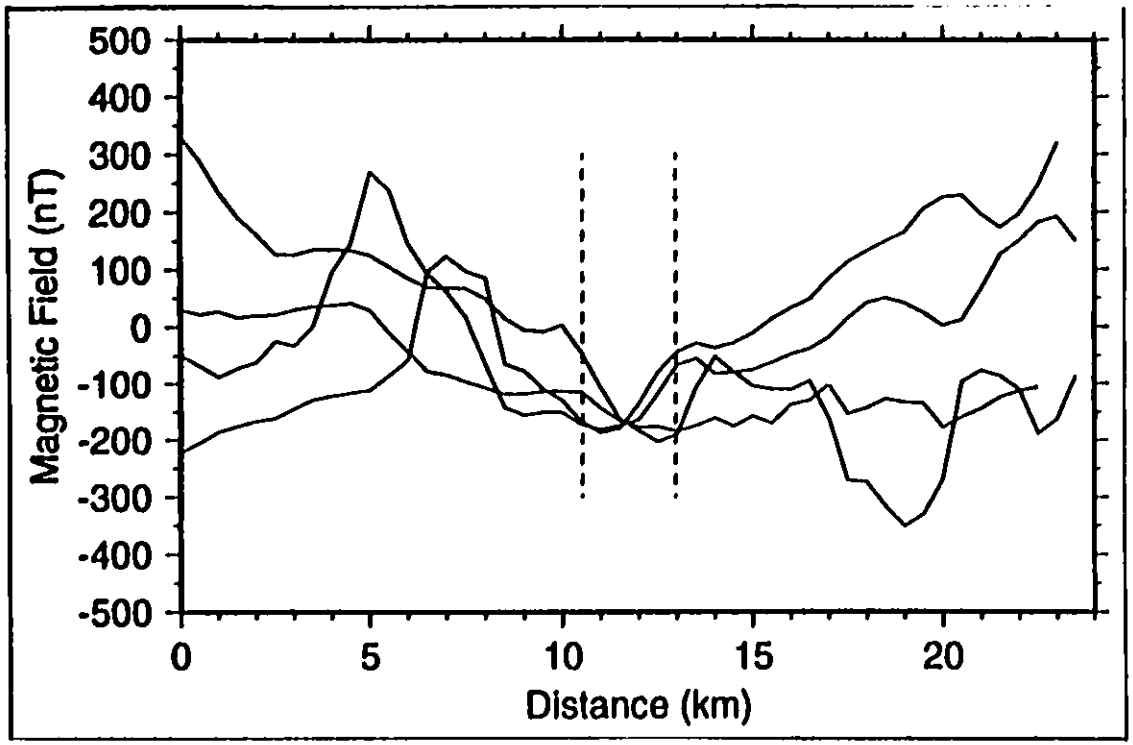

Figure 9. Magnetic field profiles across the West Hawk Lake structure from four radial traverses passing through the centre of the structure at 000°, 45°, 90° and 135° strike. Dashed lines indicate crater rim. Courtesy M. Pilkington, GSC.

10). Short (1970) has suggested that lithological differences in the basement are reflected in the types of breccia in holes 66-3 and 65-1. Alteration in brecciated lithologies is pervasive.

Hole 66-1, near the crater rim, shows susceptibilities in the fractured andesitic basement rocks of about 10^{-3} SI, and are quite uniform (Figure 11). The values exhibit little scatter compared to other logs, and are higher than the basement values in hole 65-1. Anisotropy of magnetic susceptibility measurements indicate a tight grouping of the principle axes of susceptibility at the vertical (k_1), and equally constrained groupings of the intermediate (k_2) and minimum (k_3) axes along the horizontal, suggestive of horizontal compression during the impact event. Core densities of 3.0 g/cc for hole 66-1 are similar to those for country rocks to the south of West Hawk Lake (Halliday and Griffin, 1963), suggesting that impact induced fracturing and subsequent alteration here are minimal.

4.5 NATURAL REMANENT MAGNETIZATION

NRM measurements for holes 65-1 and 66-1 are generally low, within the 1-10 mA/m range (Figures 10, 11). The largest value in hole 65-1 of $> 10^2$ mA/m corresponds to the haematized, high susceptibility layer noted in the above section. Two samples from hole 66-1 show NRM intensities higher than the average 65-1 values (Figures 10, 11). NRM inclinations show a large scatter within samples and do not exhibit any correlation with depth (Figures 10, 11). This can be attributed to a random orientation of magnetized clasts resulting from brecciation, as well as the high degree of alteration in the brecciated rocks.

Average Königsberger ratios (Q) are < 0.1 indicating that, at least within the crater rim,

induced magnetization is the dominant contributor to the observed field. This agrees with the results from the Deep Bay structure (Figure 6).

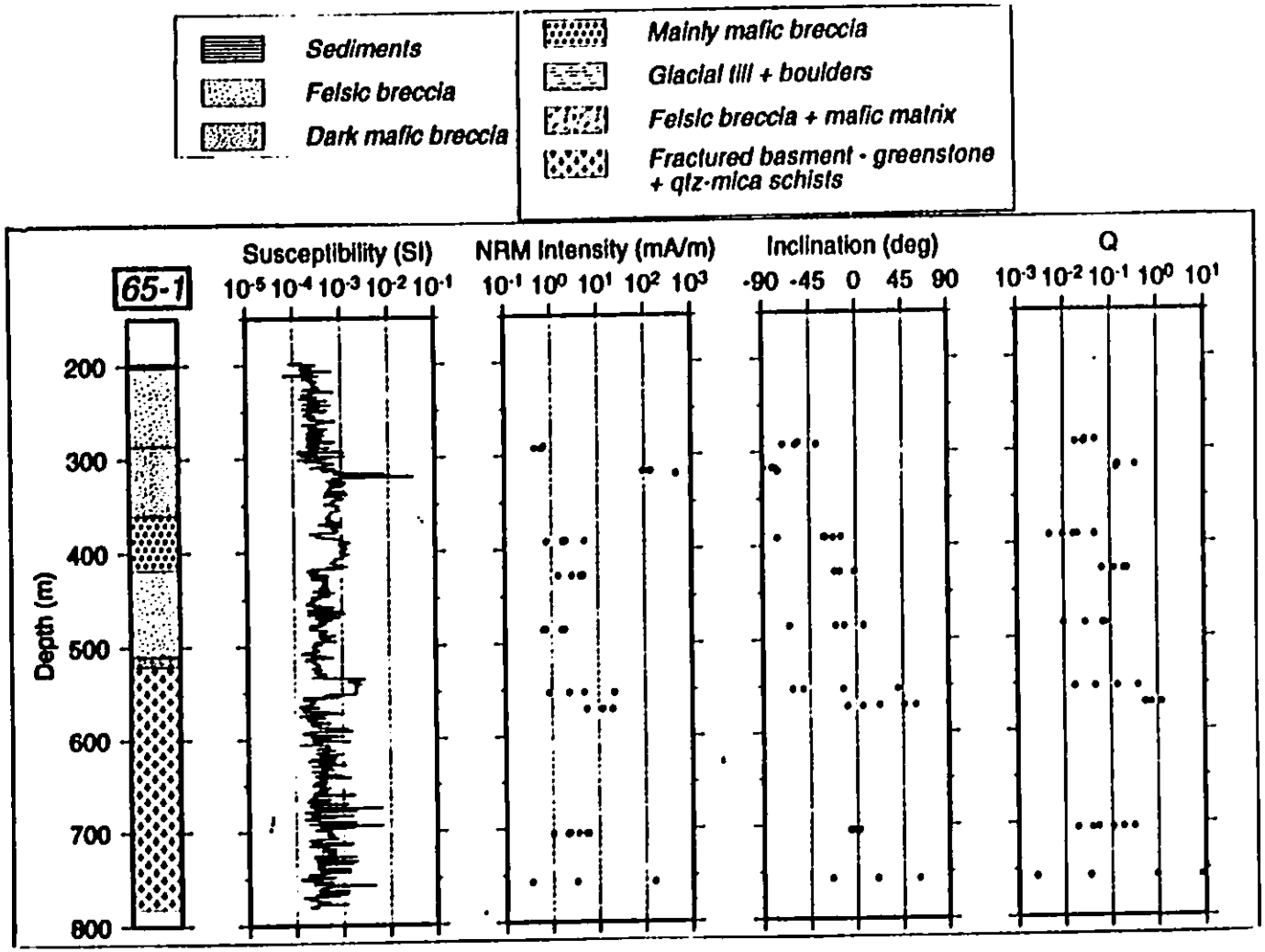

Figure 10. Drill core log and magnetic parameters for West Hawk Lake drill hole 65-1. Magnetic susceptibility values are generally uniform despite the variation in mafic content. NRM intensities are generally low with scattered inclinations. Lithology from Halliday and Griffin (1967).

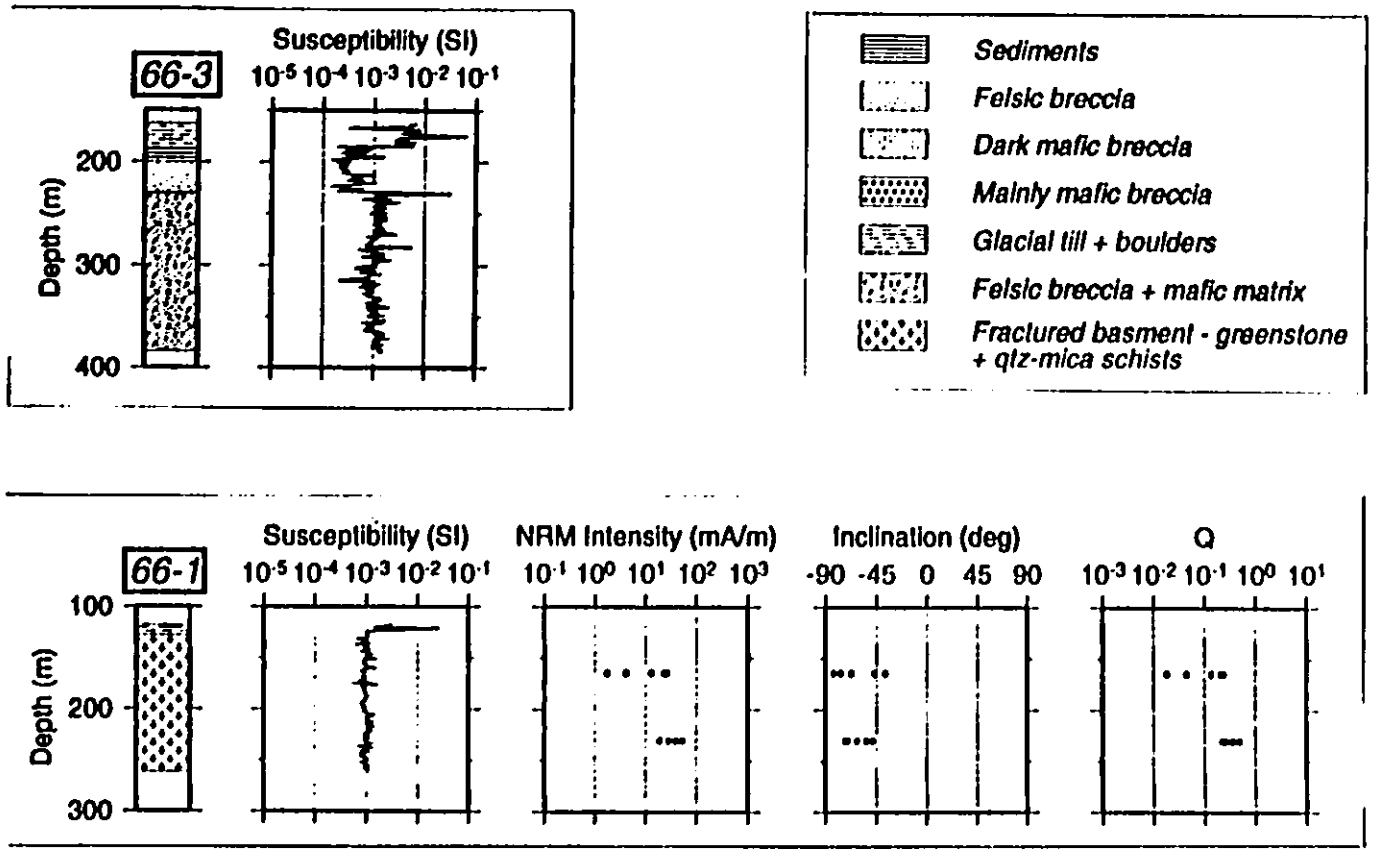

Figure 11. Drill core logs for West Hawk Lake holes 66-1 and 66-3. High susceptibility values at the top of hole 66-3 reflect the presence of glacial till and boulders, while the breccia below reflects uniform values for felsic and mafic breccias. Susceptibilities are consistent for hole 66-1, except for minor glacial deposits at the top of the core. Lithologies form Halliday and Griffin (1967).

5. THE CLEARWATER LAKES IMPACT STRUCTURES

5.1 LOCATION AND GEOLOGIC SETTING

The Clearwater Lakes structures in northern Quebec (West: 56° 13′ N, 74° 30′ W; East: 56° 5′ N, 74° 7′ W) are twin impact structures formed by a double impact, dated by Rb Sr (whole rock) and other methods at 290±20 Ma (Reimold *et al*, 1981). Clearwater West is a circular lake of 36 km diameter with an annular ring of islands. Clearwater East is smaller at 26 km and contains no islands (Figure 12). Target lithologies are Archean granodiorites, quartz-monzonites, quartz-monzodiorites, granitic gneisses, and mafic granulites of the Superior Province. There are also diabase dykes present (Bostock, 1966; Phinney et al, 1978; Simonds et al, 1978).

5.2 STRUCTURE AND DRILL CORE CHARACTERISTICS

Both Clearwater West and East are complex craters. Clearwater West has an exposed central uplift in the form of an annular ring of islands, as well as a few centrally occurring islands. Clearwater East has a submerged central uplift. Highly oxidized melt rocks and melt-breccias outcrop on the annular ring in Clearwater West, and are indicative of the highly oxidizing conditions present in the post-impact environment (Newsom, 1980).

Drilling during the 1960's penetrated mostly shocked and fractured basement rocks with zones of breccia, pseudotachylite and minor melt rock (Figures 16, 17). Hole 1-63 in Clearwater West penetrated quartz-monzodiorite, granites and granitic gneisses, representative of retrograded granulite (Hische, 1994), to a depth of 338 m.

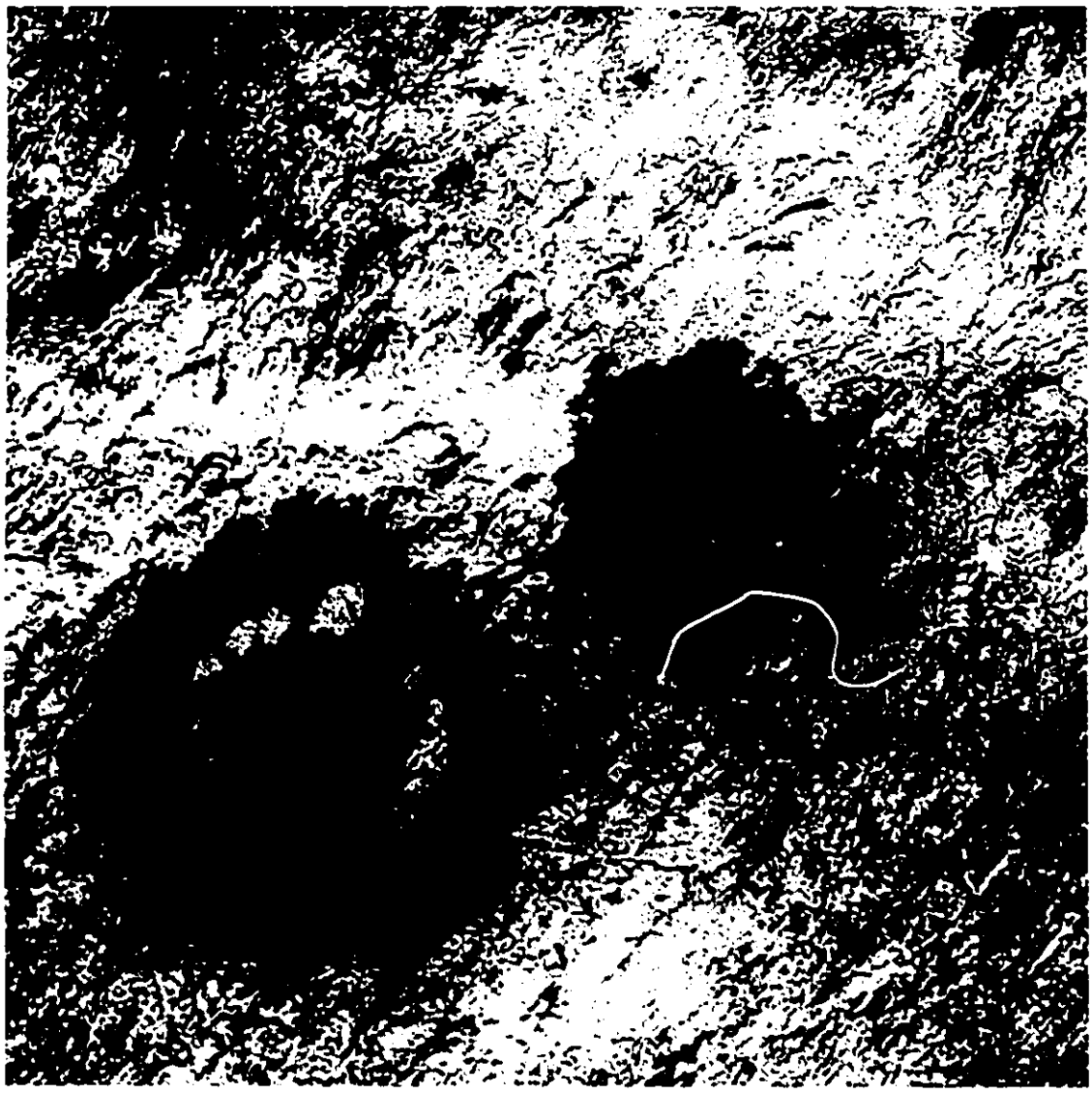

Figure 12. Landsat image of the Clearwater Lakes structures. Both are circular lakes with submerged central uplifts. Clearwater West has an annular ring of islands. Image dimensions are ~80x80 km. North is to the left. Image courtesy of GSC.

Hornblende-biotite-clinopyroxene-orthopyroxene-magnetite is the dominant mafic mineral assemblage, with minor sulphides also present. Amphibolite sections, thought to be the remains of diabase dykes, occur at ~120 m depth (Figure 16). Shock metamorphosed minerals, such as biotite and quartz, indicate peak shock pressures of 20-25 GPa (Hische, 1994).

Hole 1-64 in Clearwater East penetrated suevitic breccia (brecciated rock containing melt), and sequences of granites and quartz monzonites monzodiorites to a depth of 1009 m (Hische, 1994). Sections of amphibolite-facies diabase at 250 m and 950 m, as well as a number of pseudotachylite veins were also encountered (Figure 17). Alteration is somewhat more pervasive than in Clearwater West, with chloritization and hematization dominating.

5.3 MAGNETIC ANOMALY PROFILE

Both structures are characterized by irregular high-amplitude aeromagnetic lows of >500 nT and reaching extreme lows of -1000 nT (Figure 13). The lows are equally apparent in gridded magnetic profiles from four transects across the structures (Figures 14, 15). The central uplifts of both structures are characterized by the highest amplitude magnetic lows, while the structure rims are variable in magnetic intensity.

5.4 MAGNETIC SUSCEPTIBILITY

In Clearwater West, lithologies from hole 1-63 exhibited bulk magnetic susceptibilities on the order of $3x10^{-2}$ SI to a depth of ~250 m (Fig. 16). Below this the susceptibility drops slightly to just under 10^{-2} SI (Fig. 16). Fluctuations in susceptibility values about these averages appear to

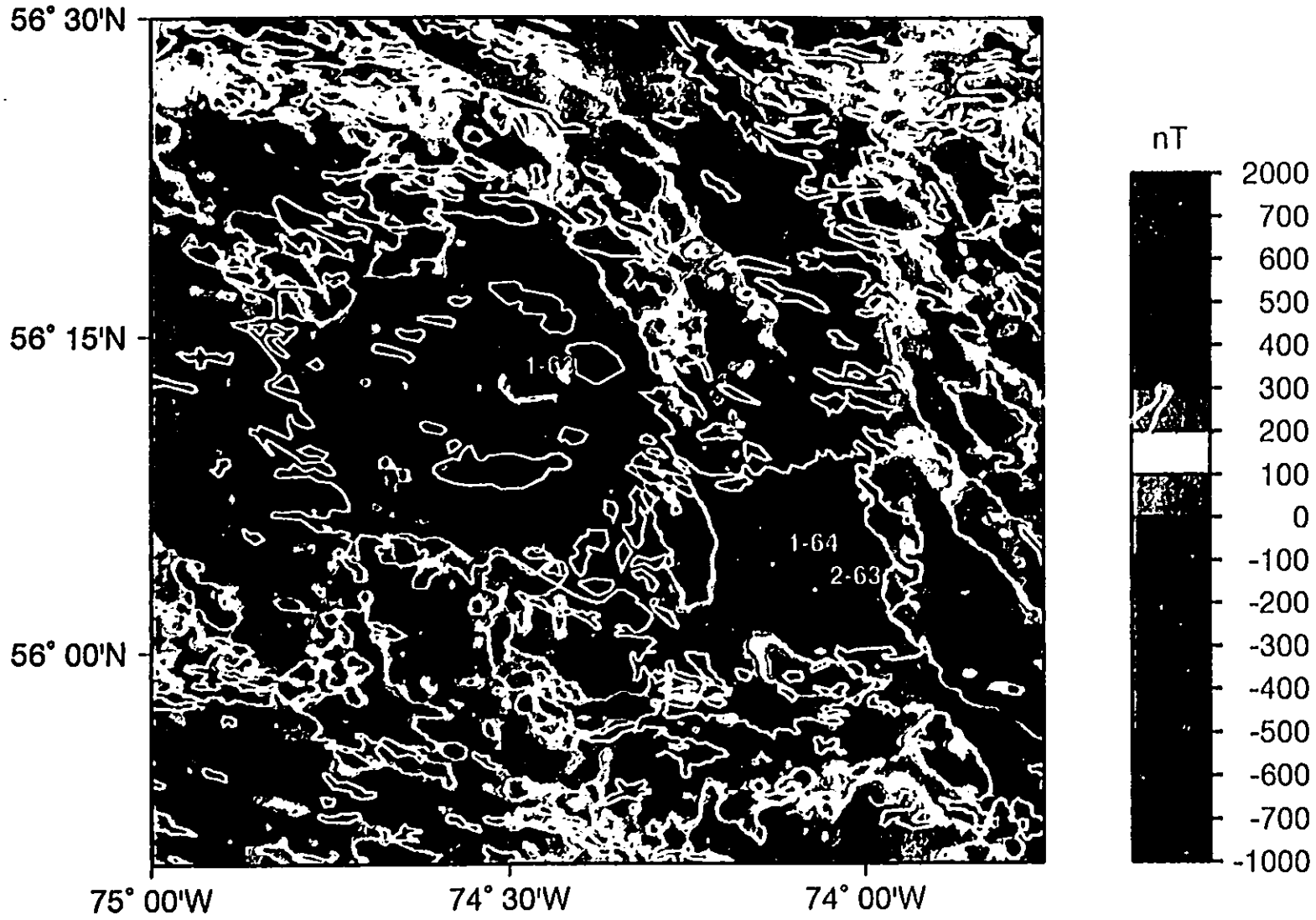

Figure 13: Magnetic anomaly map of the Clearwater Lakes impact structures. Topographic contours in white. Anomaly lows in the centres of the structures reach -1000 nT. Drill holes 1-63, 2-63 and 1-64 marked. Image courtesy of GSC.

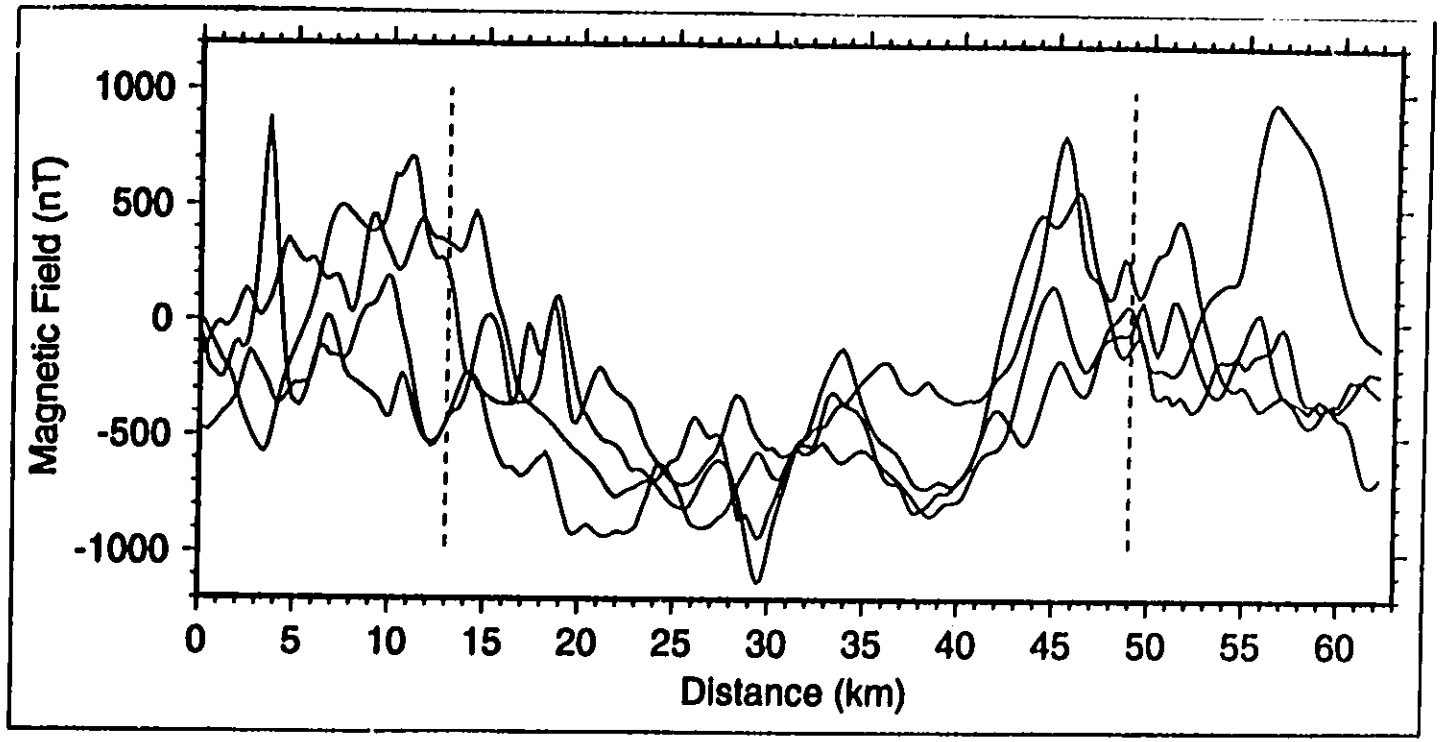

Figure 14: Magnetic field profiles from four radial transects across Clearwater West, at 000°, 45°, 90° and 135° strike. The structure (dashed lines) is characterized by a low magnetization levels, reaching -1000 nT. Courtesy GSC.

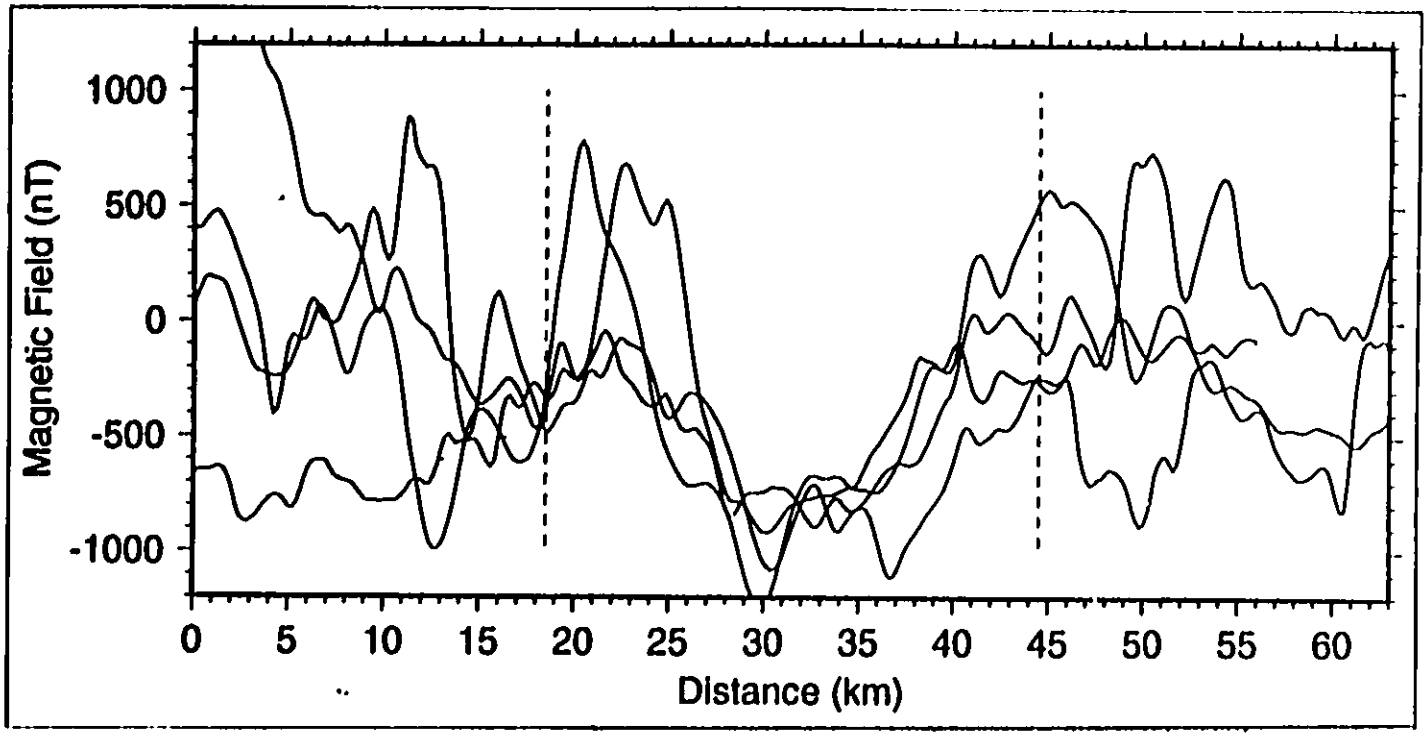

Figure 15: Magnetic anomaly profile of the Clearwater East structure from four radial transects across the structure, at 000°, 45°, 90° and 135° strike. The rims (dashed lines) enclose a zone of reduced magnetization of up to -1000 nT. Courtesy GSC.

be due to variations in mafic mineral and magnetite content, although no direct correlation with lithology is apparent (Figure 16).

In Clearwater East, the magnetic susceptibility fluctuates again with mafic mineral and magnetite content, but remains fairly constant throughout hole 1-64. Values are in the $1\text{-}3\times10^{-3}$ SI range, rising slightly to $\sim5\times10^{-3}$ SI in the bottom 300 m (Figure 17). A second, shallower drill hole was measured for magnetic susceptibility in Clearwater East. Hole 2-63 is 4.5 km from the centre of Clearwater East (Figure 13), and contains sediments with susceptibilities of $\sim3\times10^{-4}$ SI, and breccias with values of up to 10^{-2} SI (not shown). The breccia values are similar to those values found for the crystalline rocks in hole 1-63 (Figure 16).

5.4.1 AMS - CLEARWATER WEST

Anisotropy of magnetic susceptibility (AMS) measurements revealed anisotropy degrees (P) of 1.1 on average, with peak values of 1.3 to 1.4. P was found to be highly variable in the top ~ 150 m of the core, with individual samples from within 5 to 10 cm of each other exhibiting ranges of P on the order of 0.3. The top ~ 150 m of core also exhibits variable low to intermediate inclinations for the maximum axis of susceptibility (k_1). Below this, the maximum axis is predominantly vertical for the remainder of the core (Figure 18). The reason for the shallow inclination of k_1, and the highly variable degree of anisotropy (P) noted in the top third of the core, is unknown. The high inclination of k_1 below this may indicate the effect of horizontal compression of the central uplift immediately after rebound while the rocks were still undergoing

plastic deformation (Scott *et al.* 1995). Compressive stress can orient the long axis of the shape anisotropy of magnetite perpendicular to the direction of compressive stress. In the central uplift, during the last phases of plastic deformation, the stress regime is horizontal. Consequently, any reorientation or new growth of magnetite will tend to occur in the vertical direction, a process similar to the formation of a mineral foliation by tectonic stresses. The long axis of the magnetite grains will thus tend to be vertical, and consequently the maximum axis of the susceptibility anisotropy will also tend to the vertical. This interpretation is conjectural, and represents an avenue for further study in conjunction with AMS measurements from other complex impact structures (eg. Scott *et al.* 1996).

5.4.2 AMS - CLEARWATER EAST

In contrast to the high inclinations for the maximum axis of susceptibility (k_1) found in Clearwater West, Clearwater East displays a dominance of k_1 at low angles (< 30°) throughout the core (Figure 19). Given that both structures are complex craters, the effects of horizontal compression during the final stages of uplift should be similar. The results from Clearwater East may be due to the presence of pyrrhotite, which was detected in samples from petrography and from thermal demagnetization (see below). Pyrrhotite exhibits a k_1 axis perpendicular to the crystallographic c-axis, giving rise to an inverse magnetic fabric (Uyeda et al. 1963). An inverse magnetic fabric arises when a mineral such as pyrrhotite has its c-axis in the plane of maximum flattening, but its maximum susceptibility axis is perpendicular to that plane. Thus k_1 would be perpendicular to the mineral foliation, giving rise to the so-called inverse magnetic fabric.

Consequently, if the k_1 poles are inverted 90° in order to compensate for this effect, the maximum axes plot at > 60°, agreeing with the inclinations found at Clearwater East (Scott *et al.*, 1995).

The degree of anisotropy (P) was found to be slightly higher than for Clearwater West. P rises from ~1.1 to ~1.3 with depth, and isolated peak values reach 1.6. Due to the unoriented nature of the vertically drilled core, the strikes of the magnetic foliations and lineations were not determinable. The magnetic anisotropies of the samples from both structures are insufficient to influence the magnetic anomaly low (eg. Florio *et al.*, 1993), due to their low P values and their scattered orientations. The bulk susceptibilities, however, provide ~50% of the magnetization in the rocks, since Q~1 (Figures 16, 17), and thus make a significant contribution to the magnetic anomaly.

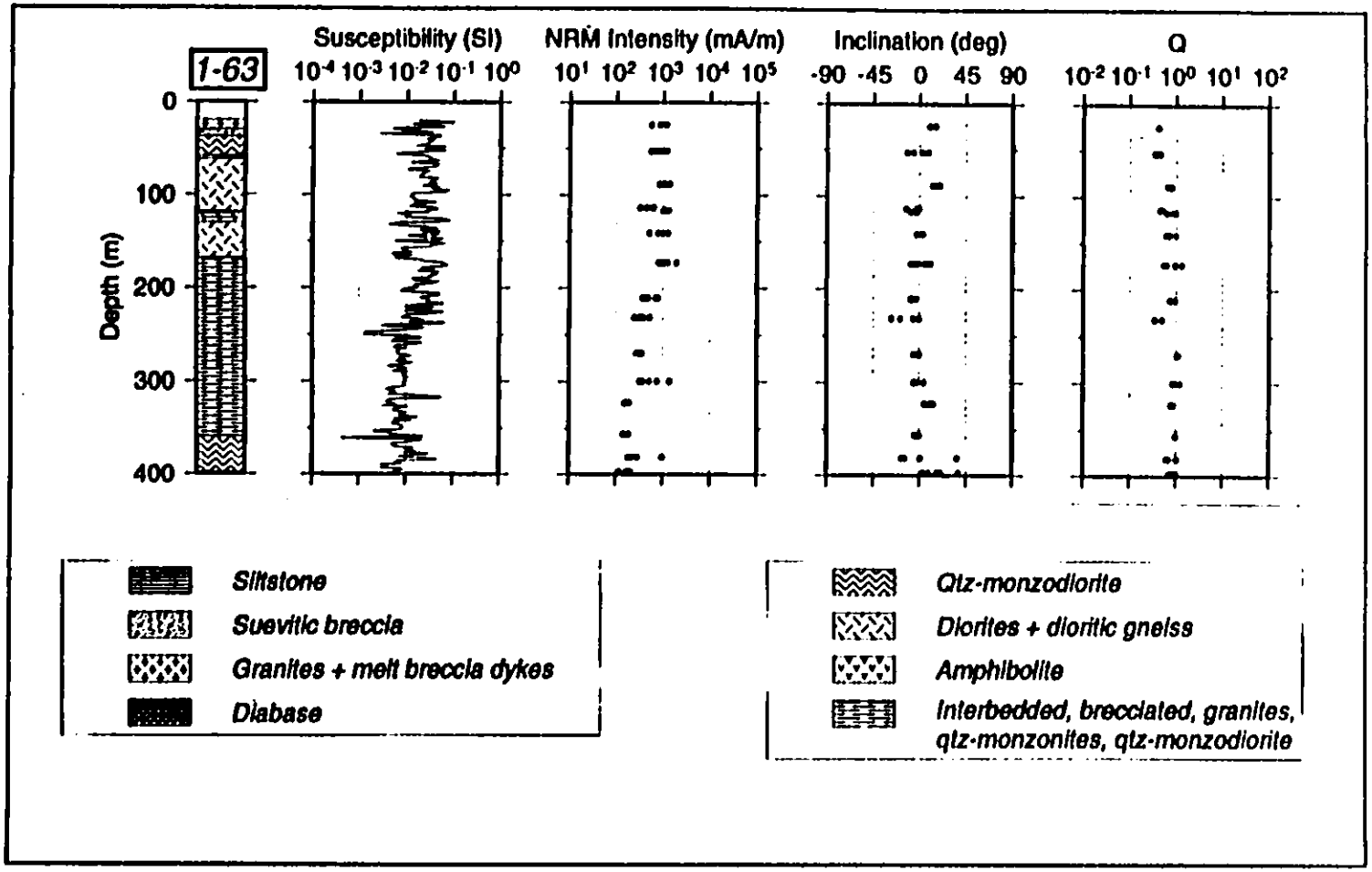

Figure 16. Clearwater West. Drill core log from hole 1-63. Magnetic susceptibilities decline slightly with depth, as do NRM intensities. NRM inclinations are very shallow and are often reversed. Q values of ~1 indicate that both susceptibility and remanence are contributing to the magnetic anomaly. Lithologies after Hische (1994).

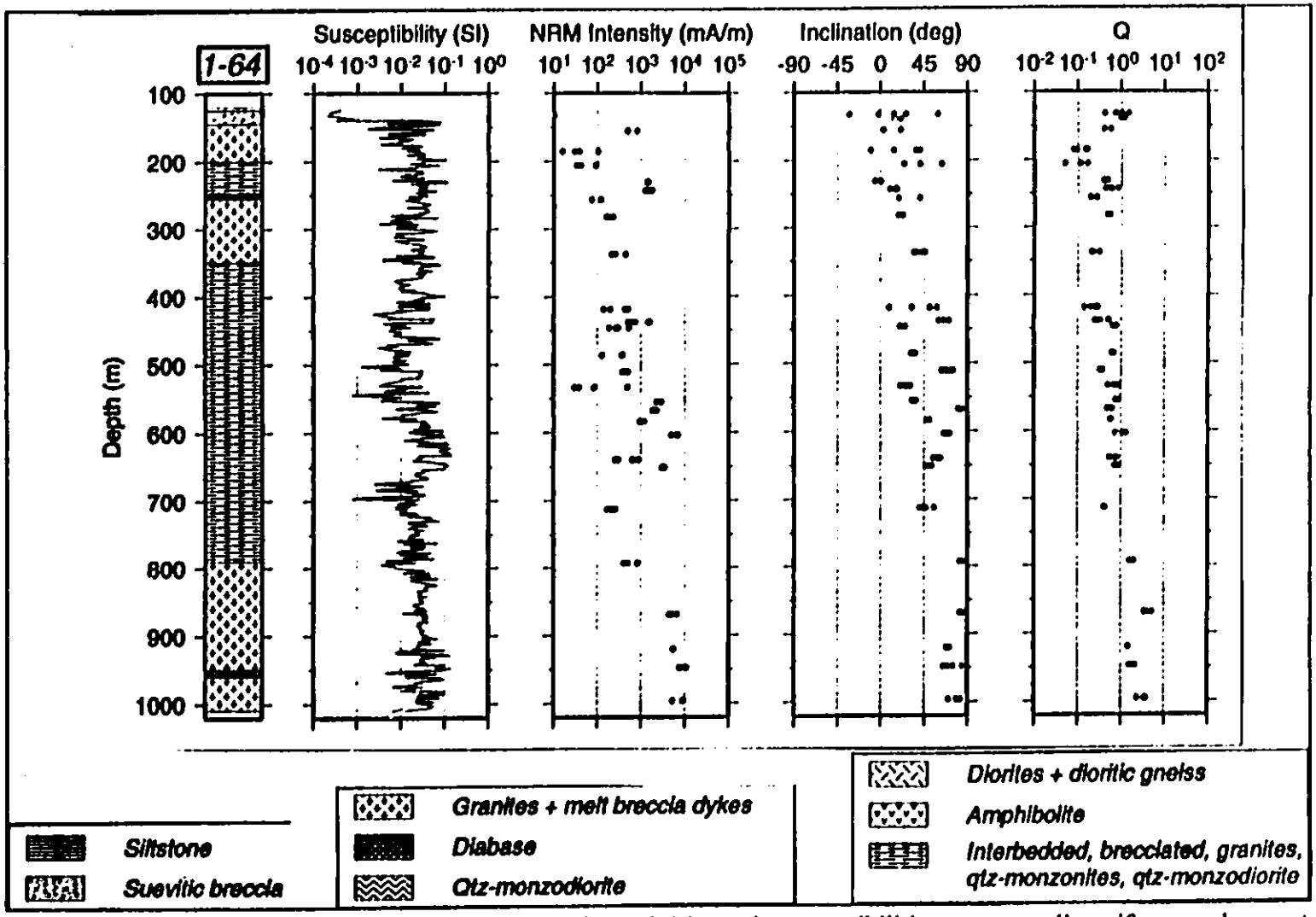

Figure 17. Clearwater East. Drill core log from hole 1-64. Magnetic susceptibilities are generally uniform, and are not dependent on lithology. NRM intensities increase with depth, as does the inclination of the NRM vector. Q rises from values <1 at the top of the core to values of ~5 at the bottom of the core. Lithologies from Hische (1994).

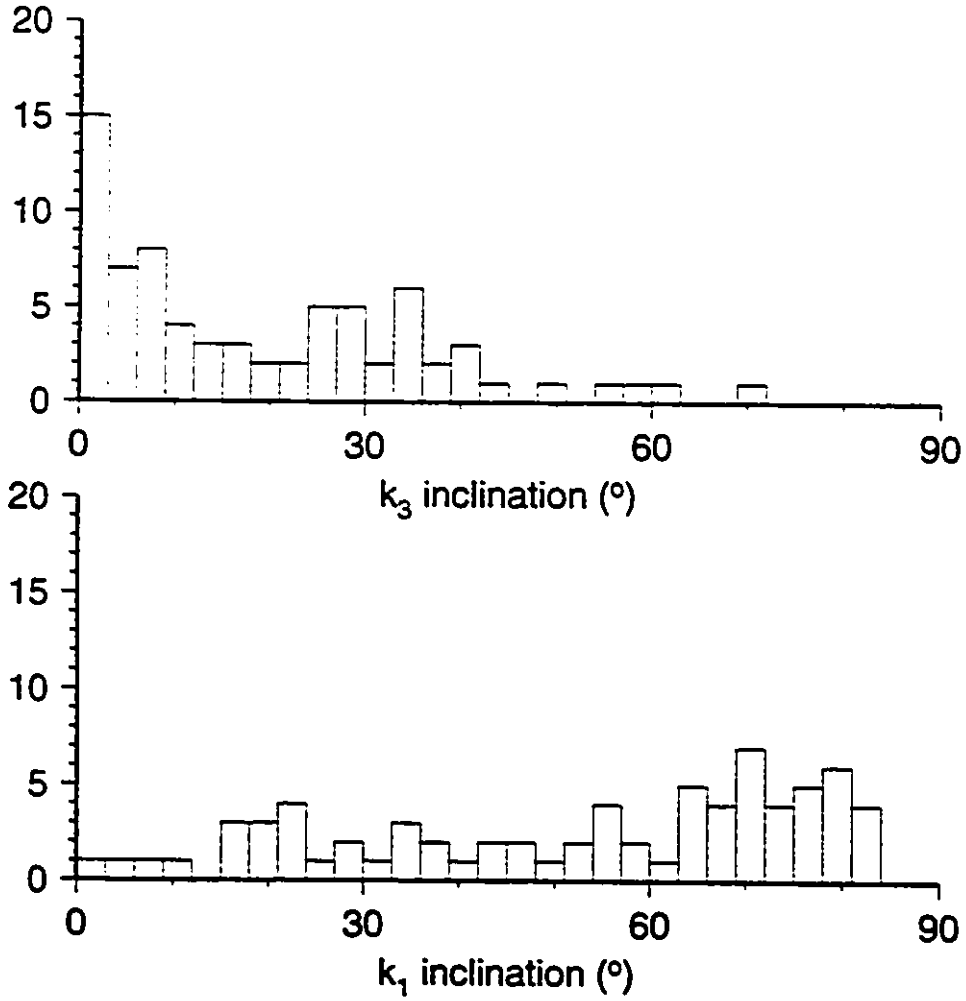

Figure 18. Histogram compilation of AMS data for Clearwater West. High angle (>60°) inclinations of k_1 are more frequent, while k_3 exhibits a dominance of inclinations below 30°.

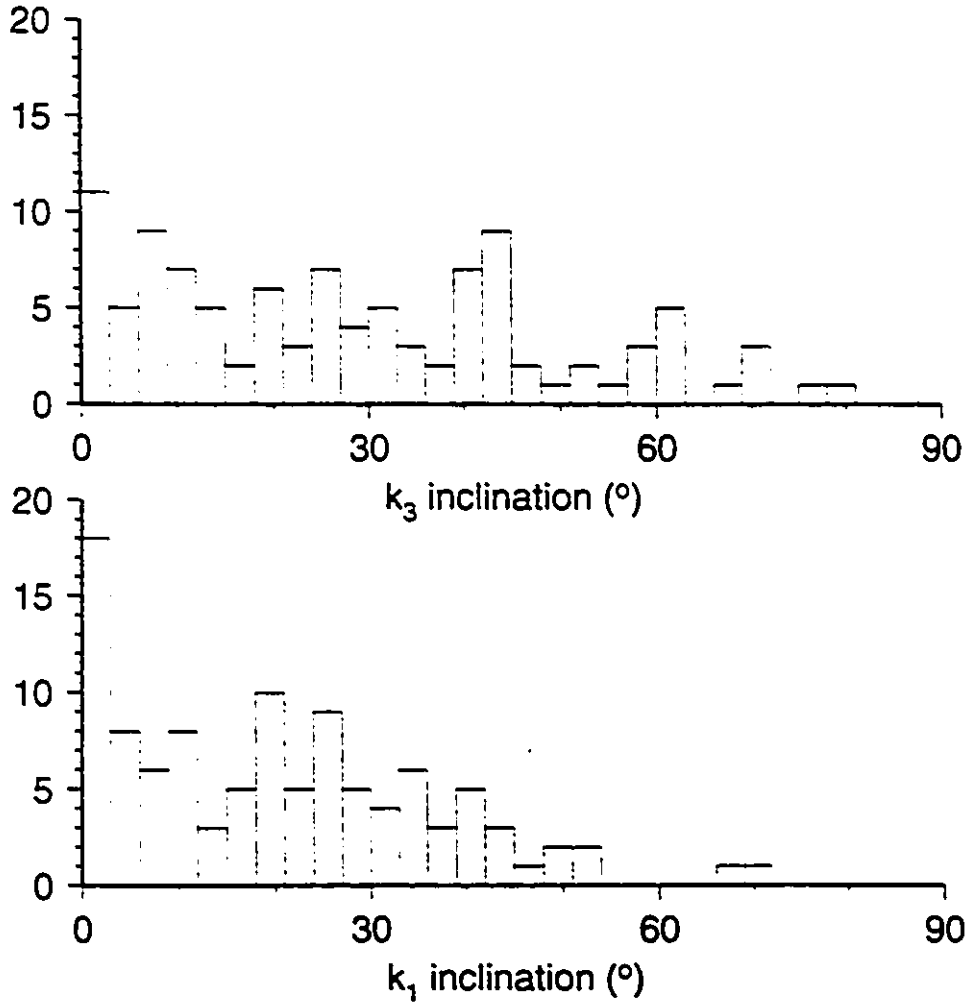

Figure 19. Histogram compilation of AMS data for Clearwater East. Low angle (<30°) inclinations of k_1 are more frequent, while k_3 exhibits a dominance of inclinations below 60°.

5.5 NATURAL REMANENT MAGNETIZATION

The natural remanent magnetization intensity in Clearwater West decreases with depth from ~ 10^3 mA/m to just above 10^2 mA/m at the bottom of the hole (Figure 16). Inclinations are very shallow and point up (reversed), with the exception of a few samples whose inclinations point down (Figure 16). Q values are very close to unity throughout the hole, and show little variation between samples (Figure 16). This indicates that the NRM adds a significant component to the resulting magnetic field anomaly. The reversed, shallow inclinations for the NRM are typical of the palaeomagnetic signature for this part of North America acquired during the Permo-Carboniferous Reversed Polarity Superchron. This observation agrees with previous radiometric dating, that determined a Permian age for the Clearwater impact (Reimold et al, 1981), and indicates the resetting of the NRM by shock heating.

Clearwater East, in contrast, exhibits more variable NRM intensity and inclinations (Figure 17). NRM intensity ranges from 10^1 - 10^2 mA/m at the top of the hole to ~10^0 mA/m at the bottom. Inclinations of the NRM vector also increase with depth, rising from ~30° at the top of the hole to almost vertical at the bottom (Figure 17). Q values show greater variation than in Clearwater West, with an increase from top to bottom of 0.1 to 5 (Figure 17). As with magnetic susceptibility, there is no direct correlation between NRM parameters and lithological changes in the core.

In order to determine the nature of the NRM present in both cores (1-63 West, 1-64 East), demagnetization was performed on selected samples to isolate any multiple remanences, and to determine the magnetic carriers.

5.5.1 AF AND THERMAL DEMAGNETIZATION, CLEARWATER WEST

Demagnetization of selected, representative samples from the entire core was done by alternating field (AF) and thermal methods. Both methods revealed that an extremely stable single component remanence is present in Clearwater West. The direction of the demagnetized remanence does not deviate from that of the NRM (Figure 20). The unblocking temperature spectra indicate that the remanence is carried by magnetite (T_c = 580°C), with little to no contribution from pyrrhotite, present in trace amounts among the observed sulphide phases (Figure 20). This is confirmed by optical petrography, which indicated 3-5% titanomagnetite in the rocks, with some grains exhibiting magnetite-ilmenite exsolution textures.

5.5.2 AF AND THERMAL DEMAGNETIZATION, CLEARWATER EAST

Both AF and thermal demagnetization resolved two components of remanence in Clearwater East (Figure 21). A high angle component, typically removed by temperatures of ~350°C and alternating fields of 15 mT, is considered to be a viscous remagnetisation (VRM) acquired at depth by the influence of the present Earth's field. Continued treatment isolated a second remanence that is stable in ranges of 350 to 550°C and 15 to 60 mT. The inclination of this stable remanence is horizontal to shallow upward (Figure 21), which is similar to the stable remanence found in Clearwater West (Figure 20) and compatible with a Permian age. Beyond 550°C and 60 mT, remanence vectors become random and no older remanent components could be identified in the Archean target rock.

Thermal demagnetization indicates the presence of both titanomagnetite and pyrrhotite

(Figure 21), with the pyrrhotite unblocking by ~350°C. Optical petrography confirms this interpretation, with large grains of pyrrhotite easily discernable, as well as pitted titanomagnetite grains.

5.5.3 SUMMARY OF DEMAGNETIZATION RESULTS

Both Clearwater East and West record a thermochemical remanent magnetization (TCRM), carried principally by magnetite, and characteristic of the magnetostratigraphy for the late Permian. The TCRM was acquired at the time of impact by resetting of the NRM by shock (SRM), heat (TRM) and chemical alteration (CRM). The discrepancy between the NRM profiles for Clearwater West and East is accounted for by the post-impact acquisition of a viscous remanent magnetization (VRM) held by pyrrhotite.

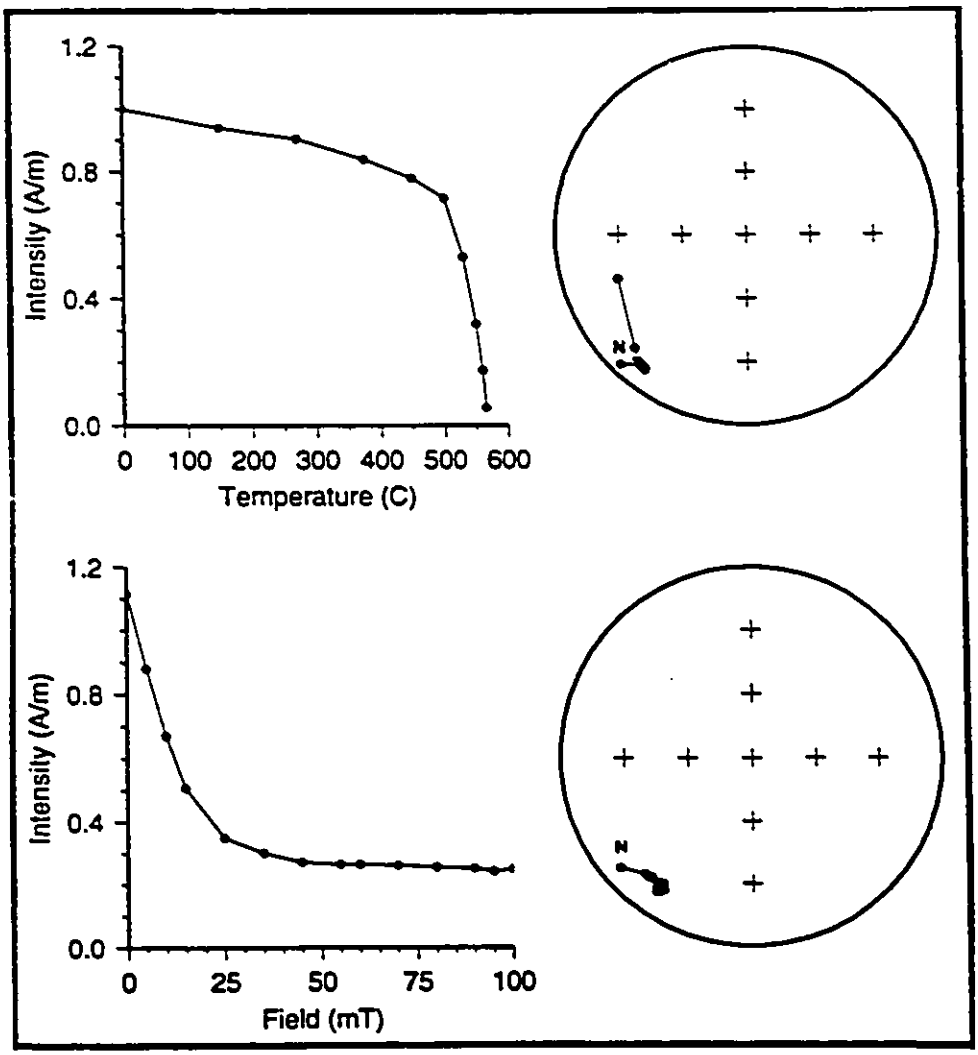

Figure 20. AF(bottom) and thermal (top) demagnetization results from Clearwater West. Samples 240 D and E; 114.6 m depth, amphibolite lithology. Remanence is very stable, of high coercive strength, and is single component. The square shouldered thermal decay spectrum is indicative of magnetite.

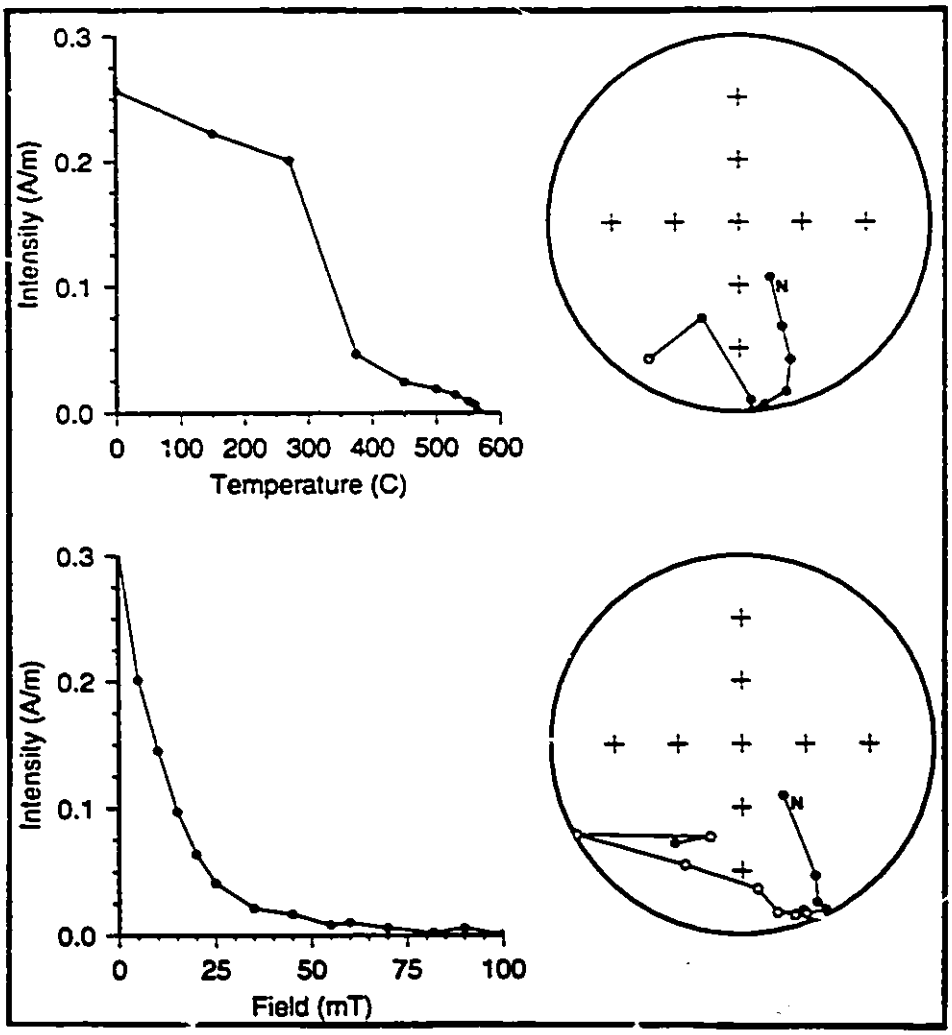

Figure 21. AF (bottom) and thermal (top) demagnetization spectra, Clearwater East. Sample 130 D and E; 629.7 m depth, hematized leucocratic granite lithology. The remanence vector rotates to the horizontal in both treatments. Thermal decay curve is indicative of pyrrhotite, which demagnetizes at ~380°C, and magnetite (565°C).

6. MAGNETIC MODELING

The previous chapters presented measured magnetic susceptibility and natural remanent magnetization data from within the impact structures. These data are used to constrain magnetic modeling parameters for the individual structures. The modeling process compares the measured magnetic values from inside the impact structures to estimated values for regional magnetic highs in order to set contrast parameters between regional and impact magnetic values. For example, if the magnetic susceptibility within a structure was measured to be ~10^{-4} SI, and estimated values for regional magnetic highs were on the order of 10^{-2} SI, then the susceptibility contrast is -10^{-2} SI. This value is assigned to the modelled crater body, resulting in a magnetic anomaly low associated with the impact structure. In all structures studied, the regional magnetic highs were used toestimate the maximum background, or regional, magnetization present in the target rocks. These modeled regional values are considered to be upper limits on pre-impact crustal magnetization. Lower modeled regional values will result in lower contrast values, and consequently reduced modeled magnetic anomaly lows over the impact structures.

Determination of the modeled body shape for West Hawk is based on the crater morphology relationship for simple craters presented by Grieve and Pesonen (1992), and discussed in Section 1.3.1. Modeling was simplified by using simple 2-D bowl shaped geometries to represent not only the visible surface structure, but also the depth to the true crater floor. In the case of complex structures with central uplifts, the depth of the zone of shocked rocks (*sensu stricto*) is determined by using the amount of structural uplift (SU) to represent the zone of affected rocks at depth, and using the morphological relationship for structural uplift (SU)

presented by Pilkington and Grieve (1992). Since these rocks have undergone hydrodynamic uplift, they have been affected during the impact event, and can be considered to represent the maximum depth of impact induced structural effects (uplift, fracturing, shock). Using the structural uplift as the maximum depth of affected rocks, a generous estimate of both the horizontal and vertical dimensions of the structure can be modeled using a simple bowl-shaped geometry. This represents an approximation of the true geometry of a complex structure, however, for magnetic modeling purposes this is adequate in representing the dimensions of the zone of reduced magnetization directly attributable to the crater morphology.

Input of magnetic declination and magnetic inclination data for the current Earth's field to the modeling program was done from published magnetic maps of Canada (Newitt & Haines, 1990 a,b).

6.1 DEEP BAY

Figures 22 and 23 show the results of magnetic modelling for the Deep Bay impact structure. The observed anomalies used are an across-strike (NW-SE) aeromagnetic transect, and a W-E transect (Figure 4). This NW-SE transect includes NE trending magnetic lineaments, and is thus useful for delineating the amplitude of the magnetic low associated with the Deep Bay structure.

The shape of the modeled crater is derived from the measured surface diameter (D) of 13 km, and the degree of structural uplift (SU) given by Pilkington and Grieve (1992), where $SU=0.086D^{1.03}$ = 1 km. A bowl shaped geometry is modelled with a maximum depth extent of

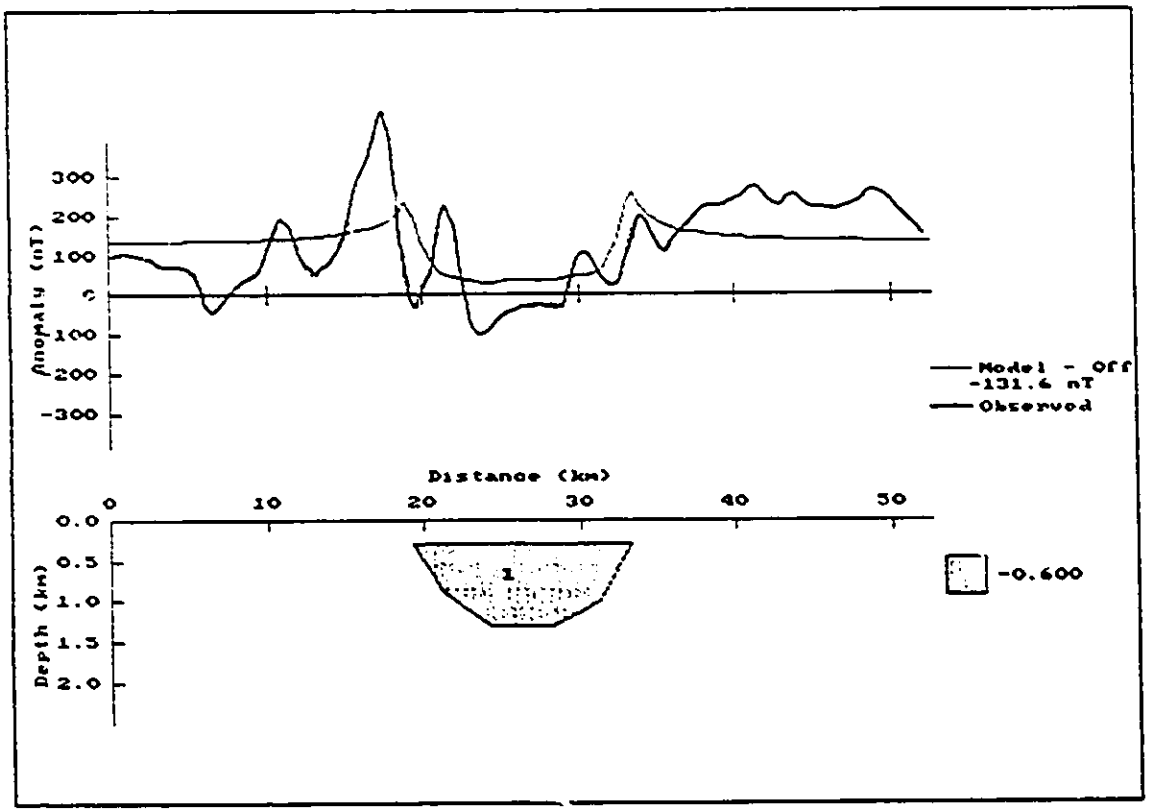

Figure 22. Magnetic anomaly model of Deep Bay. Observed field is a NW-SE aeromagnetic transect. The modelled anomaly (black) does not have the same amplitude as the observed anomaly. Modelled peaks at the edges of the crater are due to the sudden contrast between the regional rocks and the crater magnetic parameters.

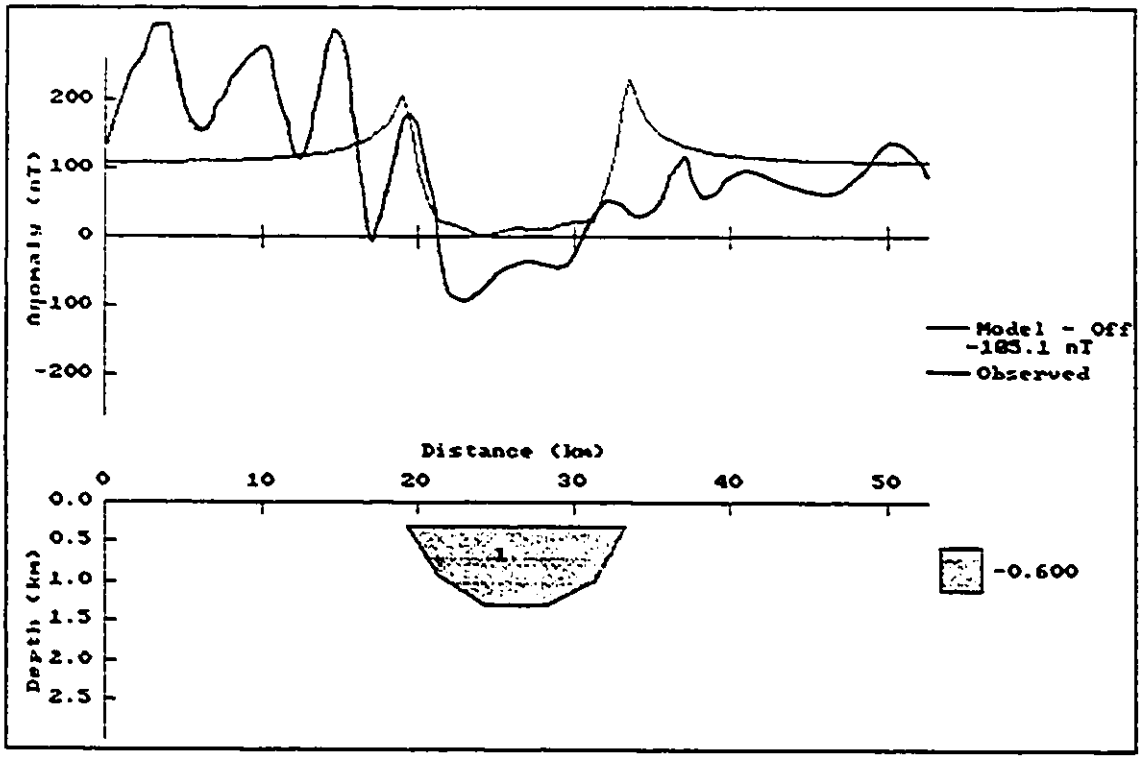

Figure 23. Magnetic anomaly model of Deep Bay, West-East transect. The observed anomaly reaches lows of -100 nT, while the modeled anomaly reaches a low of ~ 00 nT. Modeled anomaly in black, observed in red.

1 km. Due to the collection of the aeromagnetic data at a 300 m flight height, the modelled body must be "buried" by the same amount in order to compensate for the non-surface nature of the measured magnetic field.

Magnetic susceptibility and NRM intensity values measured from Deep Bay ($3x10^{-4}$SI and <10 mA m respectively) are low for high grade gneissic terrains. Modeled regional anomaly highs of >100 nT require susceptibility values of ~ 10^{-2} SI or NRM intensities of ~500 mA/m in the country rocks. Using these values to provide magnetic contrasts between the regional rocks and the modelled crater body, a magnetic anomaly low associated with the Deep Bay structure of ~20 nT is obtained along the NW-SE transect (Figure 22). However, the observed magnetic low along this transect has a maximum low of -100 nT (Figure 22). Along the W-E transect (Figure 23), the modelled low has a value of ~0-10 nT, while the observed anomaly low again reaches -100 nT. Clearly, the modelled anomaly, using maximum depth and diameter extents for the crater body, and maximum regional magnetic parameters for comparison, does not provide a modelled magnetic low sufficient to account for the observed low of -100 nT. If average regional magnetic values of ~ +100 nT are used for comparison, the modelled anomaly accounts for only 40-50% of the observed anomaly.

Consequently, the effects of brecciation, alteration and infill by non-magnetic sediments contribute to the formation of the magnetic low over the Deep Bay structure, but do not appear to account for the full amplitude of the low. An affected zone of reduced magnetization may extent beyond the borders of the impact structure.

6.2 WEST HAWK LAKE

Figures 24 and 25 show the results from modeling of the West Hawk Lake structure. The observed anomalies are: a S-N across-strike transect (Figure 25), and a NW-SE oblique to strike transect (Figure 26). The modeled body is also "buried" in the model for the reasons noted above.

West Hawk Lake is a simple crater with no central uplift. Structural relationships for simple craters give a depth to the bottom of the breccia lens (d_f) equal to $0.28D^{1.02}$, where D is the crater diameter of 2.5 km (Grieve & Pesonen, 1992). This relationship gives a depth of 0.695 km to the crater floor.

Measured susceptibilities of $3x10^{-4}$ SI and NRM intensities of <10 mA/m in the West Hawk Lake core are below the values expected in Precambrian metavolcanics (e.g., Clark & Emerson, 1991). As with Deep Bay, regional magnetic anomaly highs require magnetizations in the 10^{-2} SI or 500 mA/m range. Consequently, magnetic parameter contrasts for West Hawk are similar to those for Deep Bay. In the observed S-N magnetic profile, the low associated with the impact structure is -180 to -200 nT (Figure 24). The modeled anomaly low, using the maximum regional magnetization parameters and the measured magnetic parameters for the modeled crater body, produces a low of ~ -100 nT (Figure 24), or ~50% of the observed field over the crater.

Using the NW-SE transect (Figure 25), the observed magnetic low is again ~ -200 nT, while the modeled anomaly low reaches ~ -140 nT, or about 70% of the observed anomaly (Figure 25).

Consequently, the effects of brecciation, alteration, and weakly to non-magnetic sedimentary infill do not account for the full extent of the observed magnetic anomaly low

associated with West Hawk. A contribution of between 30% (minimum) and 50% (maximum) is required from the surrounding rock at depth in order to fully account for the anomaly low.

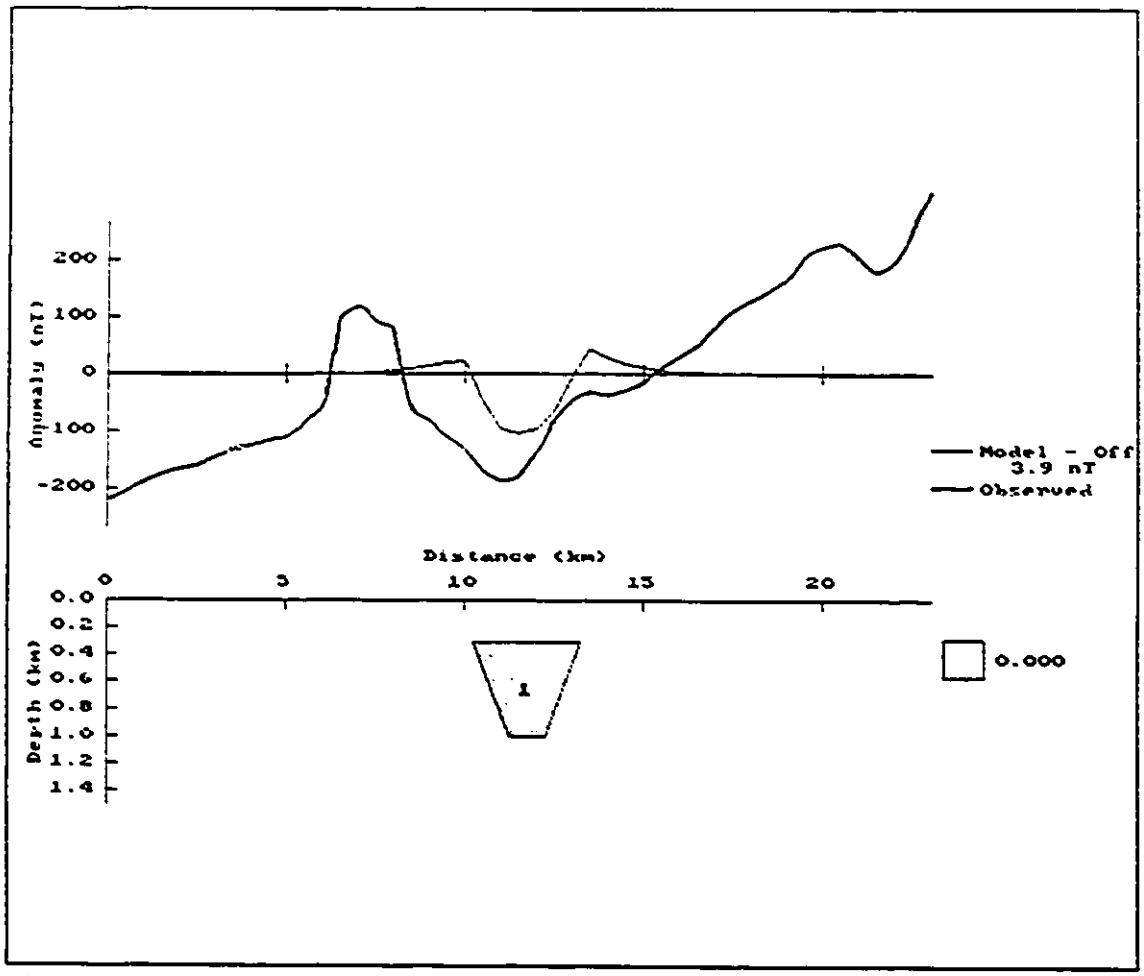

Figure 24. Modelled magnetic field anomaly for West Hawk. Observed anomaly is a south-north aeromagnetic transect. As with Deep Bay, the modelled anomaly (black), using maximum contrast values, fails to fully account for the amplitude of the observed low (red).

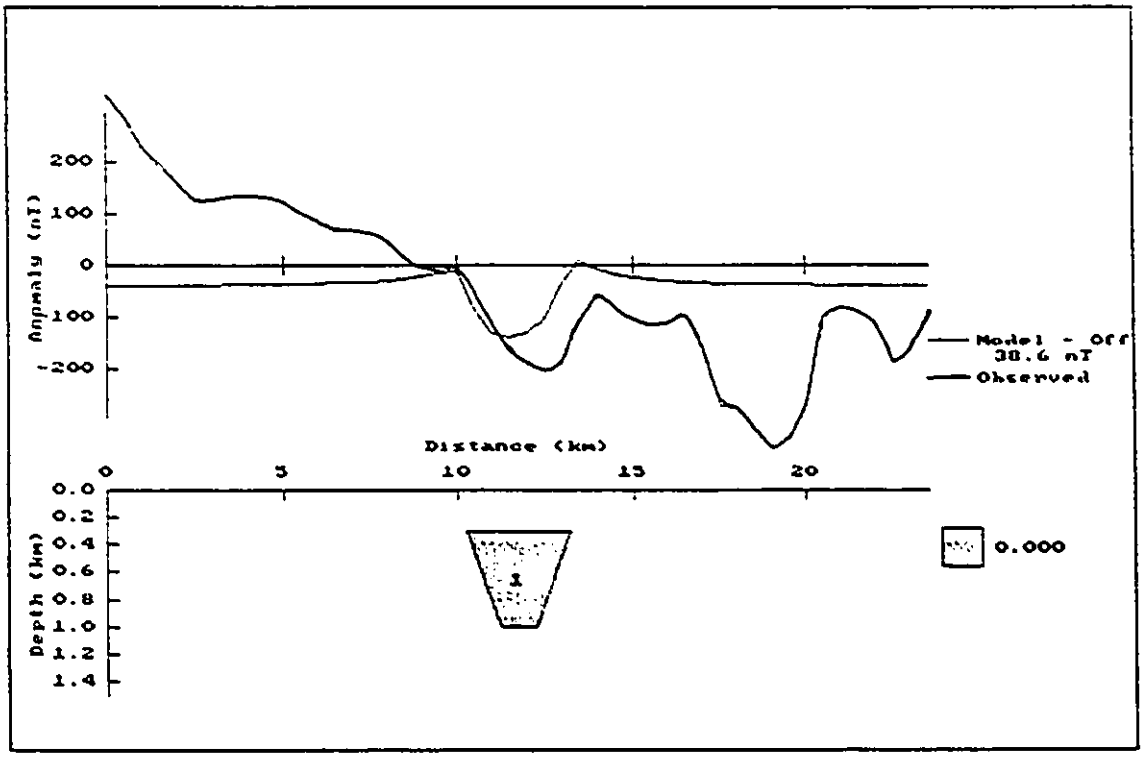

Figure 25. Magnetic anomaly model of West Hawk Lake using a NW-SE aeromagnetic transect. The observed anomaly reaches -200 nT, while the modeled anomaly reaches only to -140 nT.

6.3 CLEARWATER WEST

Figure 26 shows the results of modeling of the Clearwater West structure. The observed anomaly is a NW-SE transect, selected from the four transects shown in Figure 14, and is representative of the anomaly low associated with the impact structure.

The shape of the crater is derived from the relationship of Grieve & Pesonen (1992) for complex craters, where the depth of the affected rocks is given by the structural uplift (SU). For Clearwater West with a diameter of 36 km, this depth is 3.5 km. Again, the modeled structure is buried 300 m in order to compensate for the 300 m flight height of the aeromagnetic survey.

Drill core measurements show values of ~0.01 SI for magnetic susceptibility, and ~1 A/m for NRM intensity. Modeled values for the regional highs in the Clearwater area, where anomaly highs reach 1000 nT, require values of ~0.1 SI or equivalent NRM intensities of ~5 A/m. These values are significantly higher than those measured in the drill core from Clearwater West. Consequently, susceptibility contrasts of 0.09 SI and NRM intensity contrasts of 4 A/m were used to model the crater anomaly. It must be noted that these contrasts are again extreme values based on regional magnetic highs, and lower contrast values would result in a lower amplitude modeled anomaly low.

The shallow reversed NRM inclination will tend to deflect the total magnetization vector in the direction of the NRM declination. Although the declination was not recoverable from the drill core, its position can be estimated from the paleopole position for this part of North America at the time of impact, which gives a value ~17°W. However, from the mapped anomalies (Figure 13) this effect is not apparent, possibly due to randomization of the NRM vector in the brecciated

rocks on the flanks of the central uplift. An additional reason for the lack of the deflection effect could be the presence of a chemical remanent magnetization (CRM) in the breccia, or a viscous remagnetisation (VRM) at depth. Both effects could reasonably dilute the effect of the shallow, reversed NRM vector.

The observed magnetic anomaly low over Clearwater West reaches amplitudes of -1000 nT. Regional highs on the sides of the structure range from ~ +300 nT to +1000 nT. Using the crater morphology derived above, and the magnetic parameter contrasts based on the regional magnetic highs, the modelled anomaly has a maximum magnetic low of -600 nT (Figure 26). Although the observed anomaly reaches -1000 nT, the average observed anomaly over the crater floor is ~-800 nT. Consequently, the modelled anomaly low accounts for ~75% of the average observed anomaly over Clearwater West, using an anomaly of 0.00 nT as a baseline.

Unlike Deep Bay and West Hawk, where sedimentary infill and brecciation were obvious contributors to the reduced magnetizations measured in the drill cores, Clearwater West core is characterized primarily by shocked crystalline rocks uplifted from 3.5 km depth. Consequently, shock effects in the crystalline rocks of the central uplift are responsible for 75% of the observed magnetic anomaly low, although the thin sedimentary cover and slight brecciation probably contribute a small amount as well. However, there still remains an average discrepancy of ~ -200 nT between the observed an modeled magnetic field profiles. It would appear that additional factors beyond those considered in modeling the anomaly, must contribute to the magnetic anomaly low.

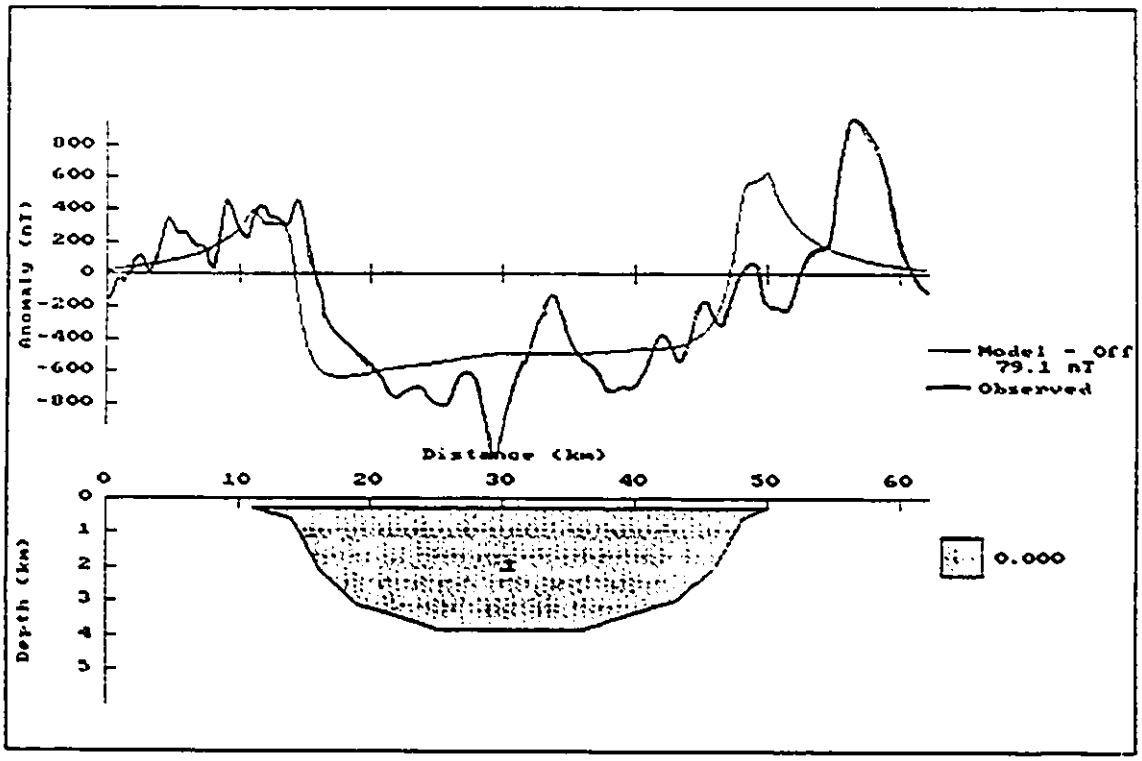

Figure 26. Magnetic anomaly model of Clearwater West. Observed field is a NW-SE transect across the structure. The modelled anomaly reaches a low of -600 nT, while the observed anomaly has an average low of about -800 nT. Peaks at the edge of the crater model are due to the "edge effect".

6.4 CLEARWATER EAST

Figure 27 shows the results of magnetic modelling for Clearwater East. The observed anomaly is a W-E transect across the structure, selected from the four transects (Figure 15), and is a good representation of the magnetic anomaly low over the structure.

As with Clearwater West, the factor SU was determined to be 2.15 km, based on a diameter of 26 km. Again, the modelled structure is buried at 300 m to compensate for the height of aeromagnetic data collection used in the observed anomaly.

Magnetic susceptibility and NRM intensities for Clearwater East are the same as for Clearwater West. The VRM in the lower part of hole 1-64 will tend to reinforce the induced magnetization vector, due to their similarity in inclination and polarity. Since Q values are ~1, the susceptibility can be modelled at a value of 0.02 SI (adding equivalent NRM intensity), and the susceptibility contrast can be set at 0.08 SI. Magnetic high values are the same as those for Clearwater West, where regional magnetic highs reach +1000 nT.

The modelled anomaly exhibits a maximum low of -400 nT, while the observed magnetic low reaches values of -800 to -1000 nT. Despite the presence of the VRM, which would serve to increase the magnetization present in the structure, the modelled values produce an anomaly that is only 50% that of the highest amplitude observed magnetic lows. Clearly, a significant reduction in magnetization has occurred beneath the structure floor. As in Clearwater West, brecciation and the thin wedge of sedimentary infill are not significant contributors to the reduced magnetization measured in the central uplift. Shock appears to be the only major contributor to the reduction in magnetic intensity in the measured drill core rocks.

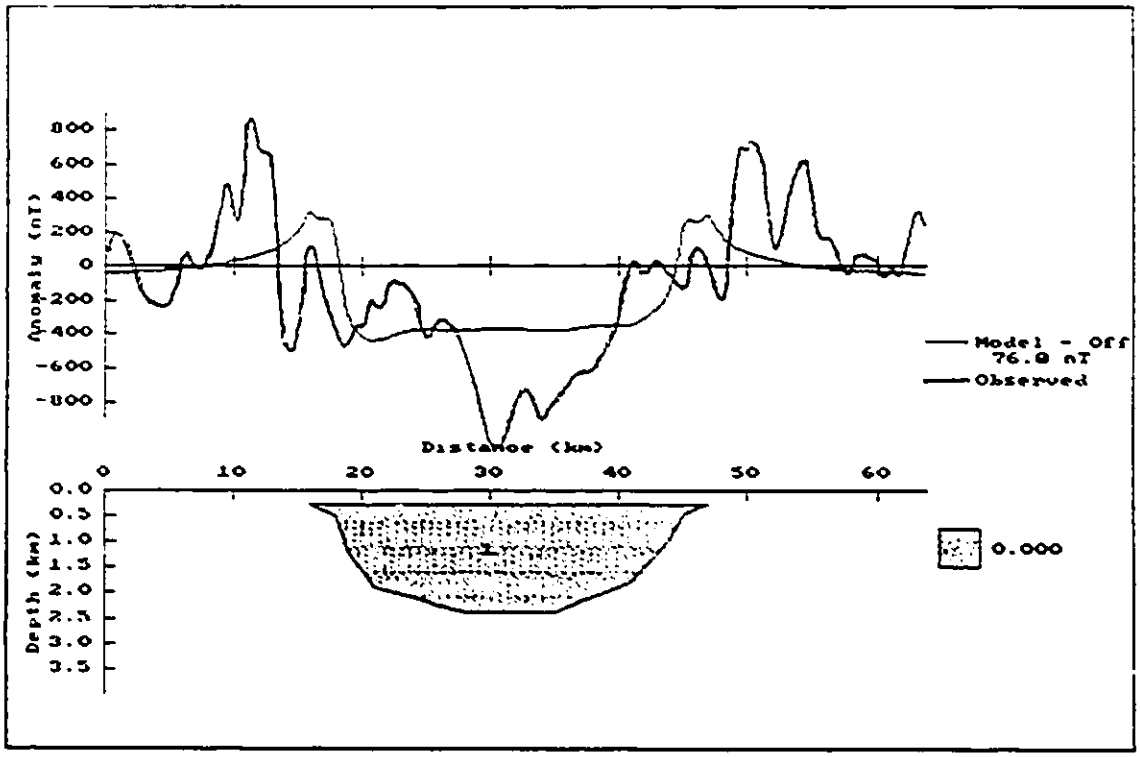

Figure 27. Magnetic anomaly model of Clearwater East. Observed field is a W-E transect across the structure. The modeled anomaly produces a low of -400 nT, 50% less than the average observed anomaly of ~ -800 nT.

6.5 DISCUSSION OF FORWARD MODELLING RESULTS

All four impact structures studied exhibit reduced magnetizations that extend beyond their morphologically defined limits (Table 2). Both Deep Bay and West Hawk contain extensive non-magnetic sedimentary infill and altered breccia layers. However, when the magnetic susceptibilities and natural remanent intensities within the structures are compared with the maximum possible magnetizations present in the surrounding rocks, the modelled anomalies are insufficient to account for the observed magnetic field low.

Several factors influence the observed magnetic lows over the impact structures (Table 2). All have been subject to infill by non-magnetic sediments, particularly Deep Bay and West Hawk. They also contain breccias, which, for the most part, have weak magnetic susceptibilities and natural remanent intensities. Brecciation randomizes NRM vectors, however the dominance of magnetic susceptibility ($Q<1$) in Deep Bay and West Hawk makes the randomization effect negligible in the formation of the observed magnetic field (Beals *et al*, 1963). Similarly, the basement rocks sampled in these structures exhibit reduced magnetic properties compared to the pre-impact regional levels. Drill hole data indicate that no simple relation between shock level and/or lithology and magnetization is apparent at any of the three structures.

The Clearwater structures are characterized by shocked uplifted basement rocks with relatively minor amounts of breccia, melt rock, and non-magnetic sedimentary infill. The Clearwater structures have much less sedimentary infill, brecciation, and alteration than do Deep Bay and West Hawk. Here the peak magnetic lows are associated with dominantly crystalline material in the central uplifts. This material has been shocked (cf. Hische, 1994), and has acquired

a reversed polarity, horizontal NRM at the time of impact. This NRM orientation should deflect the anomaly horizontally, however this is not observed in the aeromagnetic data, possibly due to the overprinting of a strong VRM at depth. The effects of shock on the target rocks are clearly seen as the dominant factor in reducing the magnetization within the structures. Significant magnetic lows remain after maximum magnetic parameter contrasts are used for modelling, and again we require an extended zone of reduced magnetization extending beyond the calculated morphological limits of the impact structures to account for the observed field.

Since modelling produces anomalies that are less than the observed anomalies, it can be suggested that the estimates for the pre-impact regional magnetizations are too low, and using higher regional magnetizations would account for the observed anomalies. This is unlikely, since the estimates for pre-impact magnetizations are based on regional magnetic highs, and thus represent an extreme upper bound for regional magnetic parameters. Assigning higher magnetic levels to the target rocks makes no sense geologically, as the modelled bodies representing lithologic units would have to shrink to geologically meaningless dimensions.

Alternatively, the morphological relationships for the depth to the bottom of the true crater (simple craters) and the amount of structural uplift (complex craters) are wrong, and the actual depths of rocks affected by shock (*sensu stricto*) is much deeper. This again is unlikely, since these relationships are constrained by studies of terrestrial impact structures where drill core is available (Grieve and Pesonen, 1992), and have been used for modelling the gravity anomalies associated with impact structures with great success (Pilkington and Grieve, 1992). Consequently, the most likely explanation for the discrepancy between modelled and observed anomalies is the

presence of an extended zone of reduced magnetization due to the impact event.

TABLE 2. SUMMARY OF MODELLING PARAMETERS AND RESULTS

STRUCTURE	LITHOLOGIC FACTORS	MAGNETIC[a] CONTRASTS	PERCENT[b] ANOMALY
DEEP BAY	BRECCIATION, ALTERATION, SEDIMENTARY INFILL	10^{-2} SI or 490 mA/m	40 - 50%
WEST HAWK	BRECCIATION, ALTERATION, SEDIMENTARY INFILL	10^{-2} SI or 490 mA/m	50 - 70%
CLEARWATER WEST	SHOCKED CRYSTALLINE	0.09 SI or 4 A/m	~ 75%
CLEARWATER EAST	SHOCKED CRYSTALLINE	0.09 SI or 4 A/m	~ 50%

a. Contrast parameters used for modelling are extreme values for either magnetic susceptibility or NRM intensity.

b. Percent anomaly is the amount of the observed anomaly accounted for by forward modelling using the morphological relationships of Grieve & Pesonen (1992), Pilkington and Grieve (1992), and the contrast parameters.

Modelled geometries of simple bowl-shaped structures based on depth extents for simple craters (West Hawk) and structural uplift for complex structures (Deep Bay, Clearwater), account for ~40% of the observed anomaly at West Hawk, ~50% at Deep Bay, and ~50 to 75% at the Clearwater structures (Table 2).

Consequently, the target rocks beneath the crater floors must reflect an impact-induced reduction in NRM intensity and susceptibility. At Clearwater, based on the analysis of crystallographic shock effects, Hische (1994) estimated recorded shock levels of 5-10 GPa at ~400 m depth in hole 1-63 and ~15 GPa at ~1000 m in hole 1-64, well above that required to cause decreased magnetization levels (Pohl, 1994). However, modelling indicates that reduced magnetizations exist at depths well below the zone marked by diagnostic shock effects in silicate minerals, such as planar deformation features (PDFs) in quartz and pyroxenes, and kink bands in biotite (eg. Stöffler, 1972, 1974). This reduction appears to be due to the passage of the attenuated shock wave, now downgraded in energy to a transient stress wave, through these rocks.

6.5.1 SOURCES OF ERROR

Any quantitative geophysical study must include some attempt at estimation of error in order to constrain the final interpretation. In this study, instrumental measurement errors are several orders of magnitude below the values measured. For example, instrument error in aeromagnetic magnetometers is ~1 nT (M. Pilkington, pers com, 1996). Measurement error in NRM values is <1 mA/m in intensity, and <1° in inclination and declination. Error in magnetic

susceptibility measurements is $\pm 1 \times 10^{-5}$ SI for the Exploranium instrument, $\cdot 10^{-4}$ SI for the Sapphire Instruments SI bridge, and $<10^{-7}$ SI for the KLY-2 Kappabridge. All of the measured magnetic values are at least one, and usually several orders of magnitude larger than the instrument errors, which can therefore be regarded as insignificant.

Of greater significance is the error associated with Grieve and Pesonen's (1992) morphological dimensions for simple and complex craters. Grieve has estimated the possible error associated with the dimensions of simple craters as <5%, and that associated with complex craters as 10-20% (R.A.F. Grieve, pers. com. 1996). These uncertainties reflect the small sample dataset used to construct the morphological relationships, as well as the lack of detailed dimensional data from drilling. An additional problem in determining the dimensions of impact structures is the degree of erosion. Older structures in glaciated terrains have been subject to considerable erosion, and consequently the original dimensions must be estimated. The morphological relationships, nevertheless, are currently the best available estimates of crater dimensions, and have worked well for gravity anomaly studies (Pilkington and Grieve, 1992).

The modeling process introduces further sources of error. Modeling 3-D structures in 2-D can introduce an error of ±5-10% in the modeled anomaly (M. Pilkinton, pers. com. 1996). Lack of available regional magnetic data from the undeformed country rocks outside of the impact structure requires the estimation of pre-impact target rock magnetic parameters based on the observed regional magnetic field. In order to favour a conservative interpretation of the modeled anomalies, the maximum pre-impact magnetizations were estimated from regional magnetic highs. The error in this procedure would thus contribute to higher amplitude modeled anomalies.

While instrumental measurement errors can be considered insignificant, the modeling of crater dimensions in 2-D, the uncertainty in the morphological relationships, and the estimation of regional magnetic values, introduce the significant sources of error in this study. Consequently, the interpretation of the modeled anomalies must be regarded as first-order approximations. However, it can be noted that all three impact structures studied exhibit magnetic anomaly lows that are not fully accounted for by the models. The degree to which some additional and unknown factor contributes to the magnetic lows is currently difficult to constrain accurately.

6.5.2 THE TRANSIENT STRESS WAVE

As the impact shock wave spreads out from the point of impact, its energy attenuates until it can no longer produce brecciation, melting, and shock features in silicate minerals. At this point, the shock wave can better be described as a transient stress wave (or acoustic, seismic wave). This wave will continue to diminish in energy as it travels away from the point of impact until it dissipates completely (eg. Melosh, 1989). The question of the effect of the transient stress wave on the magnetization of rocks outside of the impact structure (*sensu stricto*) remains. Experimental studies by Nagata (1971) of the effect on the magnetization of basalts under mechanical shock regimes, indicated that even at low transient mechanical shock pressures, the natural remanent magnetization can be partially demagnetized. Nagata referred to this phenomenon as dynamical remanence. Nagata's study was undertaken in order to determine whether repeated blows with a geological hammer on basalts during sample acquisition might affect the NRM in the rocks sampled (insignificantly). Nagata's study determined that mechanical shock, of sufficient

magnitude, will cause irreversible dislocations in the domain walls in magnetite, leading to a diminished NRM intensity.

Similar work done by Pohl, Bleil and Hornemann (1975), also on basalts and using an automated hammer, determined that transient stress waves of up to 8 kbar will demagnetize both single and multi-domain magnetite. Their study agreed with the conclusions of Nagata (1971), and also suggested that an additional effect was the irreversible rotation of spontaneous magnetizations in magnetite in the 2.5 to 10 kbar transient stress pressure range.

The above studies concentrated on the effect of transient stresses on the NRM. Diminished remanent intensity or the acquisition of a new remanence by transient stresses has been termed shock remanent magnetization (SRM). The effect of transient stress on the magnetic susceptibility of magnetite was investigated by Kumar and Ward (1963). Their study was undertaken in order to determine the effect of stress waves from nuclear explosions on the magnetic susceptibility of surrounding materials, in this case a magnetite grout mixture. Their research found a 4% increase in the amount of haematite in the grout mixture after shock loading, indicating a shock induced chemical transformation of magnetite to haematite. The dominant effect, however, was a drop in magnetic susceptibility after shock loading, suggesting that the stress wave produces destructive changes in the magneto-crystalline structure of magnetite.

The above effects of the transient shock or stress wave have been documented in various rock types and experimental conditions by Hargraves and Perkins (1969), Wasilewski and Doan (1973), and by Cisowski and Fuller (1978). It is clear from these studies that transient stress waves produced by impacts (and man-made explosions) can reduce both NRM intensity and

magnetic susceptibility, primarily by introducing changes in the magneto-crystalline structure of magnetite.

Detailed crystallographic studies on shock loaded magnetite grains have yet to be done (D. Stöffler, pers com, 1995). A study of the effects of shock on ilmenite was attempted by Blyth Robertson (GSC) on rocks from the Charlevoix impact structure in Quebec. This study was abandoned due to the difficulty in discriminating between shock effects and natural variations in the ilmenite grains (R.A.F. Grieve, pers com, 1996).

In the context of this study, it appears that the amplitudes of the magnetic anomaly lows are derived not only from within the impact structure dimensions, but also from surrounding rocks that have been subject to demagnetization by the transient stress wave.

7.0 CONCLUSIONS AND FUTURE RESEARCH

This study was undertaken in order to determine the origin of the reduced magnetic field intensities associated with the three impact structures. Natural remanent magnetization (NRM) and magnetic susceptibility (and its anisotropy) data from drill cores within the structures provided ground truth constraints for magnetic modelling. Modelling the anomalies indicated that the reduced magnetizations associated with impact generated breccias, shocked crystalline rocks, and post-impact alteration and sedimentary infill, is insufficient to account for the amplitude of the anomalies. A zone of reduced magnetization extending vertically beyond the calculated structure dimensions is required to fully account for the magnetic anomaly lows.

Although no drill core that sampled below the true crater bottom (West Hawk) or below the central uplift (Deep Bay, Clearwater) was available, it can nevertheless be inferred from the previous studies cited that the diminished shock wave, in the form of a transient stress wave, has affected the magnetization of magnetic carrier minerals well below the modelled depths. For example, the zone of reduced magnetization at Clearwater East must extend several kilometres beneath the centrally uplifted rocks in order to account for the observed anomaly.

Unfortunately, drill core that extends to these depths is not presently available. From a petrographic point of view, neither the shock wave nor the transient stress wave produce optically visible changes in oxide magnetic carriers. The transition from shock to stress is marked by the termination of shock induced metamorphism in silicate minerals. Consequently, confirmation of the effects of the transient stress wave by direct petrographic methods on deep rocks from the

impact structures are not currently possible.

Further research on the crystallographic effects of transient shock and stress waves on the magneto-crystalline structure of magnetite is needed. While previous studies have demonstrated that both NRM intensity and magnetic susceptibility can be reduced in magnetite grains by mechanical shock pressures, detailed studies on the dislocations induced by shock along domain walls, and other magneto-crystalline effects have yet to be done. Further study of the effects of shock on magnetite would hopefully delineate the range of stress pressures over which the magnetic characteristics of magnetite are affected. Combined with theoretical calculations of the attenuation of the shock wave from impact events, this data would be useful in constraining the zone of affected rocks at depth associated with impact structures.

REFERENCES

ALDAHAN, A.A., 1990. Petrology and mineral alterations of granitic rocks from the Gravberg-1 well, Siljan impact structure, Sweden; *Scientific Summary Report (VG) 1990:50*, Vattenfall, 63 p.

BEALS, C.S., INNES, M.J.S., & ROTTENBERG, J.A., 1963. Fossil meteorite craters; in *The Moon, Meteorites and Comets*, ed. B.M. Middlehurst & G.P. Kuiper, University of Chicago Press, Chicago, p. 235-284.

BLAKELY, R.J., 1995. *Potential Theory in Gravity and Magnetic Applications*, Cambridge U. P., 441 pp.

BOSTOCK, H.H., 1966. The Clearwater Complex, New Quebec; *Geol. Surv. Can. Bull. 178*, 49 p.

BUTLER, R.F., 1992. *Paleomagnetism*, Blackwell, Boston, 319 pp.

CISOWSKI, S.M., & FULLER, M., 1978. The effect of shock on the magnetism of terrestrial rocks; *J. Geophys. Res. 83*, p. 3441-3458.

CLARK, J.F., 1980. Geomagnetic surveys at West Hawk Lake, Manitoba, Canada; *Dept. Energy, Mines Res., Earth Phys. Br. Ser. 20*, p. 1-11.

CLARK, D.A., & EMERSON, D.W., 1991. Notes on rock magnetization characteristics in applied geophysical studies; *Explor. Geophys., 22*, p. 547-555.

COLES, R.L., & CLARK, J.F., 1982. Lake St. Martin impact structure, Manitoba, Canada: Magnetic anomalies and magnetizations; *J. Geophys. Res. 87*, p. 7087-7095.

DABIZHA, A.I., & FEDYNSKY, V.V., 1975. The Earth's "astroblemes" and their diagnosis by geophysical methods (in Russian). *Zamlya i Vselennaya; v. 3*, p. 56-64.

DENCE, M.R., INNES, M., & ROBERTSON, P.B., 1964. Recent geological and geophysical studies of Canadian craters. in *Shock Metamorphism of Natural Materials*, ed. B.M. French and N.M. Short, Mono Book Corp., Baltimore, p. 339-362.

DENCE, M.R., 1972. The nature and significance of terrestrial impact structures. *Int. Geol. Cong. 24th (Montreal, Canada), Harpell's, Quebec*, p. 77-89.

FELDMAN, V.I., 1995. The conditions of shock metamorphism: in B.O. Dressler, R.A.F. Grieve & V.L. Sharpton (eds.), *Large Meteorite Impacts and Planetary Evolution*, Geol. Soc. Amer. Spec. Pap. 293, p. 121-132.

FLORIO, G., FEDI, M., RAPOLLA, A., FOUNTAIN, D.M., & SHIVE, P.N., 1993. Anisotropic magnetic susceptibility in the continental lower crust and its implications for the shape of magnetic anomalies. *Geophys. Res. Lett. 20*, p. 2623-2626.

GRIEVE, R.A.F., & PESONEN, L.J. 1992. The terrestrial impact cratering record: *Tectonophys. 216*, p. 1-30.

GRIEVE, R.A.F., & MASAITIS, V.L., 1994. The economic potential of terrestrial impact craters, *Int. Geol. Rev., 36*, p. 105-151.

GRIEVE, R.A.F., RUPERT, J., SMITH, J., & THERRIAULT, A., 1995. The record of terrestrial impact cratering, *GSA Today*, 5, p. 189, 194-196.

HALLIDAY, I., & GRIFFIN, A.A., 1963. Evidence in support of a meteorite origin for West Hawk Lake, Manitoba, Canada; *J. Geophys. Res. 68*, 5297-5305.

HALLIDAY, I., & GRIFFIN, A.A., 1966. Preliminary results from drilling at West Hawk Lake crater; *J. Roy. Astr. Soc. Can., 60*, no. 2, p. 1-10.

HALLIDAY, I., & GRIFFIN, A.A., 1967. Summary of drilling at West Hawk Lake crater; *J. Roy. Astr. Soc. Can. 61*, no. 1, p. 1-8.

HARGRAVES, R.B. & PERKINS, W.E., 1969. Investigations of the effect of shock on natural remanent magnetism. *J. Geophys. Res. 74*, p. 2576-2589.

HENKEL, H. 1982: The Lake Mien structure; *Sveriges Geologiska Undersokning, Sektionen Geofysik, Anslag NFR 2638-3*, 7 p.

HENKEL, H., & GUZMAN, M., 1977. Magnetic features of fracture zones; *Geoexpl. 15*, p. 173-181.

HISCHE, R., 1994. Geology of the Clearwater Impact Structure, Quebec (in German). *Unpublished Ph.D. thesis, Westphälian Wilhelm University*, Münster, 113 p.

INNES, M.J.S., PEARSON, W.J., & GEUER, J.W., 1964. The Deep Bay crater; *Publications of the Dominion Observatory, Ottawa, v. 31*, p. 19-52.

JOHNSTON, W.G.Q., 1982. Geology of the Southend Area; Saskatchewan Geological Survey, *Open File Rep. OF 82-4*, p.63-67.

KUKKONEN, I.T., KIVEKÄS, L., & PAANANEN, M., 1992. Physical properties of kärnäite (impact melt), suevite and impact breccia in the Lappajärvi meteorite crater, Finland; *Tectonophys. 216*, p. 31-40.

KUMAR, A., & WARD, J.H., 1963. The effect of explosive shock on the susceptibility of magnetite grout mixture; *University of California, Report Mt-63-10*, 8 p.

MASAITIS, V.L., MIKHAILOV, M.V., & SELIVANOVSKAYA, T.V., 1975. The Popigay meteorite crater, *Dokl. Akad. Nauk SSSR*, p. 85-102. (in Russian).

MELOSH, H.J., 1989. *Impact Cratering: A Geologic Process*, Oxford Uni. Press, New York, 245 pp.

MORRIS, R.V., GOLDEN, D.C., BELL III, J.F., & LAUER Jr., H.V., 1995. Hematite, pyroxene, and phyllosilicates on Mars: Implications from oxidized impact melt rocks from Manicouagan Crater, Quebec, Canada; *J. Geophys. Res.*, p. 5319-5328.

NAGATA, T., 1971. Introductory notes on shock remanent magnetization and shock demagnetization of igneous rocks. *Pure & Appl. Geophys. 89-6*, p. 159-177.

NEWITT, L.R. & HAINES, G.V., 1990a. Magnetic Inclination Chart of Canada 1990.0, *Geol. Surv. Can. Can. Geophys. Atlas 9*, scale 1:10 000 000.

NEWITT, L.R. & HAINES, G.V., 1990b. Magnetic Declination Chart of Canada 1990.0, *Geol. Surv. Can. Can. Geophys. Atlas 10*, scale 1:10 000 000.

NEWSOM, H.E., 1980. Hydrothermal alteration of impact melt sheets with implications for Mars; *Icarus 44*, p. 207-216.

PESONEN, L.J., MARCOS, N., & PIPPING, F., 1992. Palaeomagnetism of the Lappajärvi impact structure, western Finland; *Tectonophys.*, *216*, p. 123-142.

PHINNEY, W.C., & SIMONDS, C.H., 1977. Dynamical implications of the petrology and distribution of impact melt rocks. in *Impact and Explosion Cratering*, ed. D.J. Roddy, R.O. Pepin and R.B. Merrill, Pergamon Press, New York, p. 771-790.

PHINNEY, W.C., SIMONDS, C.H., COCHRAN, A., & McGEE, P.E., 1978. West Clearwater, Quebec impact structure, Part II: Petrology; *Proc. Lunar Planet. Sci. Conf., 9th*, p. 2659-2693.

PILKINGTON, M., & GRIEVE, R.A.F. 1992. The geophysical signature of terrestrial impact craters; *Rev. Geophys. 30*, p.161-181.

PLADO, J., PESONEN, L.J., ELO, S., PUURA, V., & SUUROJA, K., 1996. Geophysical research on the Kärdla impact structure, Hiuumaa Island, Estonia; *Meteoritics & Planet. Sci. 31*, p. 289-298.

POHL, J., 1971. On the origin of the magnetization of impact breccias on Earth; *Zeitschrift für Geophysik 37*, p. 549-555.

POHL, J., BLEIL, U., & HORNEMANN, U., 1975. Shock magnetization and demagnetization of basalt by transient stress up to 10 kbar. *J. Geophys. 41*, p. 23-41.

POHL, J., STÖFFLER, D., GALL, H., & ERNSTSON, K., 1977. The Ries impact crater; in *Impact and Explosion Cratering*, ed. D.J. Roddy, R.O. Pepin and R.B. Merrill, Pergamon Press, New York, p. 343-404.

POHL, J., 1994. The effect of shock on magnetic properties of rocks and minerals [abs]. *Third International Workshop: Shock Wave Behaviour in Nature and Experiment, Limoges Rochechouart France, Program with Abstracts*, p.51

REIMOLD, W.U., GRIEVE, R.A.F., & PALME, H., 1981. Rb-Sr dating of the impact melt from East Clearwater, Quebec; *Contrib. Min. Pet. 76*, p. 73-76.

ROBERTSON, P.B., & GRIEVE, R.A.F., 1977. Shock attentuation at terrestrial impact structures: in *Impact and Explosion Cratering*, ed. D.J. Roddy, R.O. Pepin and R.B. Merrill, Pergamon Press, New York, p. 343–404.

ROBERTSON, P.B., & ROY, J.L., 1979: Shock-diminished paleomagnetic remanence at the Charlevoix impact structure, Quebec; *Can. J. Earth Sci. 16*, no.9, p. 1842-1856.

ROY, J.F., SAUNDERS, E., & REYNOLDS, J., 1972: An electric furnace for studying the magnetic properties of rocks (in French): *Publications of the Earth Physics Branch 42*, p. 229-237.

SCOTT, R.G., PILKINGTON, M. & TANCZYK, E.I., 1995. Magnetic study of the Clearwater Lake impact structures [abs.], *Lunar & Planet. Sci. XVI*, Houston, p. 1261-1262.

SCOTT, R.G., GRIEVE, R.A.F. & PILKINGTON, M., 1996. Petrographic and rock magnetic study of the central magnetic anomaly, Manicouagan impact structure, Quebec [abs.], *Lunar & Planet. Sci. XVII*, Houston, p. 1163-1164.

SHORT, N.M. 1970: Anatomy of a meteorite impact crater: West Hawk Lake, Manitoba, Canada; *Geol. Soc. Amer. Bull. 81*, p. 609-648.

SIMONDS, C.H., PHINNEY, W.C., McGEE, P.E., & COCHRAN, A. 1978: West Clearwater, Quebec impact structure, Part I: Field geology, structure and bulk chemistry; *Proc. Lunar Planet. Sci. Conf. 9th*, p. 2633-2658.

STÖFFLER, D., 1972. Deformation and transformation of rock-forming minerals by natural and experimental shock processes I. Behaviour of minerals under shock compression. *Fortschr. Miner. 49*, p. 50-113.

STÖFFLER, D., 1974. Deformation and transformation of rock-forming minerals by natural and experimental shock processes II. Physical properties of shocked minerals. *Fortschr. Miner. 51*, p. 256-289.

TARLING , D.H., & HROUDA, F., 1993. *The Magnetic Anisotropy of Rocks*: Chapman & Hall, London, 217 pp.

UYEDA, S., FULLER, M.D., BELSHE, J.C., & GIRDLER, R.W., 1963. Anisotropy of magnetic susceptibility of rocks and minerals. *J. Geophys. Res. 68*, p. 279-291.

WASILEWSKI, P.J., & DOAN, A.S., 1973. Remanent magnetization and structural effects due to shock in natural and man-made iron-nickel alloys, in Rohde, R.W., Bitcher, B.M., Holland, J.R. & Karnes, C.H. (Eds.), *Metallurgical Effects at High Strain Rates*, Plenum Press, New York, 352 pp.

APPENDIX A: AMS DATA

APPENDIX A1: DEEP BAY - HOLE 62-1A - AMS DATA

SAMPLE	DEPTH (m)	k_1 (SI)	DEC. (°)	INC. (°)	k_2 (SI)	DEC. (°)	INC. (°)	k_3 (SI)	DEC. (°)	INC. (°)
DBY010A	93.9	3.513E-04	150.49	4.77	3.268E-04	246.98	53.53	3.082E-04	57.00	36.06
DBY010B		3.289E-04	177.34	34.60	3.123E-04	294.50	33.49	2.671E-04	55.18	37.64
DBY010C		2.672E-04	143.59	2.49	2.598E-04	236.17	45.91	2.322E-04	51.19	43.98
DBY010D		2.415E-04	299.61	15.21	2.346E-04	193.13	46.21	2.071E-04	42.72	39.82
DBY010E		2.051E-04	199.90	52.15	1.999E-04	296.45	5.06	1.791E-04	30.33	37.39
DBY020A	120.6	3.898E-04	7.81	52.08	3.849E-04	172.15	36.87	3.686E-04	267.91	7.62
DBY020B		3.653E-04	243.21	63.24	3.570E-04	347.52	7.10	3.413E-04	80.95	25.65
DBY020C		3.972E-04	326.73	26.85	3.933E-04	213.09	38.37	3.728E-04	81.72	39.85
DBY020D		3.681E-04	173.79	51.41	3.587E-04	279.63	12.29	3.392E-04	18.70	35.89

DBY030A	141.3	3.068E-04	139.58	15.37	2.861E-04	45.85	13.33	2.321E-04	276.68	69.44
DBY030B		3.791E-04	323.69	3.54	3.579E-04	53.95	4.19	3.088E-04	193.67	84.51
DBY030C		4.240E-04	155.14	0.27	4.018E-04	65.09	10.52	3.681E-04	246.61	79.48
DBY030D		4.835E-04	147.55	9.25	4.633E-04	55.86	10.24	3.870E-04	278.85	76.13
DBY030E		3.490E-04	147.42	6.82	3.309E-04	56.16	10.41	2.725E-04	270.12	77.51
DBY040A	173.1	4.249E-04	274.22	23.61	4.175E-04	109.00	65.68	4.085E-04	6.65	5.52
DBY040B		4.574E-04	295.72	2.03	4.501E-04	29.03	58.44	4.479E-04	204.48	31.48
DBY040C		5.568E-04	300.71	27.56	5.468E-04	167.69	52.59	5.425E-04	43.63	23.19
DBY040D		4.552E-04	236.51	39.51	4.424E-04	134.75	13.88	4.288E-04	29.30	47.16

DBY050A	184.5	1.710E-04	280.73	44.59	1.580E-04	11.58	0.85	1.479E-04	102.43	45.40
DBY050B		4.749E-06	326.93	15.60	5.644E-07	74.22	46.78	9.921E-06	223.85	39.03
DBY050C		8.946E-05	331.73	0.53	7.919E-05	61.98	24.58	7.257E-05	240.57	65.41
DBY050D		2.583E-04	346.07	23.77	2.462E-04	85.58	20.57	2.300E-04	211.95	57.68
DBY050E		6.236E-04	329.51	24.05	6.115E-04	91.66	47.51	5.778E-04	223.90	31.10
DBY060A	204.9	3.803E-04	130.13	41.75	3.625E-04	234.54	15.58	3.567E-04	340.22	44.11
DBY060B		4.675E-04	128.85	41.25	4.657E-04	288.19	46.86	4.502E-04	29.54	10.45
DBY060C		3.919E-04	79.18	37.67	3.726E-04	342.30	8.82	3.633E-04	241.28	50.95
DBY060D		2.337E-04	289.43	3.22	2.285E-04	179.92	80.77	2.243E-04	19.92	8.73
DBY060E		1.659E-04	91.18	47.31	1.631E-04	313.38	34.35	1.604E-04	207.28	22.09

DBY070A	226.5	1.609E-04	206.87	0.50	1.588E-04	116.67	21.75	1.529E-04	298.12	68.25
DBY070B		1.610E-04	290.56	3.46	1.530E-04	200.45	1.89	1.355E-04	81.88	86.05
DBY070C		1.263E-04	145.45	24.20	1.246E-04	240.70	11.50	1.173E-04	354.09	62.88
DBY080A	233.7	3.140E-04	264.11	19.64	3.070E-04	69.81	69.78	2.979E-04	172.46	4.61
DBY080B		2.680E-04	261.61	35.36	2.656E-04	10.71	24.76	2.585E-04	127.56	44.41
DBY080C		3.237E-04	252.04	31.02	3.167E-04	346.25	6.97	3.148E-04	87.53	58.03
DBY090A	246.0	2.430E-04	135.37	82.71	2.366E-04	308.09	7.23	2.296E-04	38.20	0.92
DBY100A		2.541E-04	99.20	19.63	2.510E-04	197.69	22.49	2.284E-04	332.12	59.40
DBY100B	276.0	2.634E-04	286.73	11.39	2.565E-04	191.34	25.02	2.337E-04	39.18	62.18
DBY100C		2.561E-04	223.02	2.81	2.503E-04	131.69	25.24	2.347E-04	318.95	64.59

DBY100D		2.744E-04	159.84	18.67	2.709E-04	251.03	3.48	2.369E-04	351.20	70.98
DBY110A		2.648E-04	359.05	20.50	2.623E-04	89.65	0.85	2.312E-04	181.92	69.48
DBY110B		3.449E-04	348.69	33.48	3.429E-04	81.39	4.02	3.120E-04	177.41	56.21
DBY110C	288.0 *	5.533E-04	23.94	32.11	5.434E-04	9.3281	7.32	4.914E-04	187.96	56.86
DBY110D		2.710E-03	82.38	19.47	2.342E-03	330.55	46.45	1.940E-03	187.88	37.09
DBY110E		5.511E-04	83.90	25.36	5.169E-04	329.74	40.81	4.282E-04	196.14	38.61
DBY120A		4.605E-04	308.26	29.27	4.508E-04	200.77	28.19	4.343E-04	75.46	47.16
DBY120B	294.0	3.116E-04	51.01	8.45	3.037E-04	141.33	2.13	2.837E-04	245.35	81.29
DBY120C	294.0	2.455E-04	88.47	55.91	2.368E-04	335.64	14.71	2.212E-04	236.93	29.98
DBY130A	315.0	4.295E-04	96.79	53.76	4.062E-04	223.40	23.62	3.950E-04	325.59	25.77

DBY130B		3.670E-04	196.68	80.61	3.574E-04	85.47	3.42	3.486E-04	354.95	8.74
DBY140A	321.6	3.917E-04	307.41	58.35	3.888E-04	160.26	27.38	3.731E-04	62.49	14.64
DBY140B		3.787E-04	111.94	34.34	3.549E-04	335.79	46.55	3.430E-04	218.94	23.16
DBY140C		4.100E-04	181.81	45.34	3.946E-04	86.72	5.02	3.866E-04	351.83	44.22
DBY140D		3.611E-04	140.57	31 87	3.541E-04	277.39	49.56	3.493E-04	35.91	22.15
DBY140E		4.091E-04	179.26	49.23	3.998E-04	294.57	20.23	3.888E-04	38.76	33.63
DBY150A	351.3	3.560E-04	32.25	37.14	3.441E-04	221.68	52.49	2.993E-04	125.71	4.56
DBY150B		2.986E-04	353.96	46.98	2.751E-04	187.28	42.24	2.673E-04	91.17	6.68
DBY150C		2.806E-04	1.13	39.64	2.601E-04	219.17	43.55	2.304E-04	108.79	20.12
DBY150D		3.411E-04	328.94	37.41	3.332E-04	217.76	25.28	3.240E-04	102.55	42.05

DBY150E	351.3	3.658E-04	8.73	49.38	3.293E-04	200.11	40.06	3.072E-04	105.35	5.65
DBY160A	384.6	2.095E-04	336.72	21.16	1.782E-04	67.77	2.72	1.585E-04	164.73	68.65
DBY160B		1.429E-04	326.20	43.49	1.287E-04	67.20	11.37	1.121E-04	168.51	44.28
DBY160C		3.090E-04	341.93	47.15	2.612E-04	75.06	2.89	2.456E-04	167.72	42.70
DBY170A	394.5	1.314E-04	109.57	9.62	1.262E-04	358.43	64.91	1.113E-04	203.68	22.95
DBY170B		4.369E-04	111.70	24.46	4.252E-04	358.05	41.44	3.896E-04	223.06	38.69
DBY170C		4.027E-04	99.78	30.65	3.788E-04	344.50	35.79	3.754E-04	218.60	39.13
DBY170D		3.105E-04	85.27	43.52	2.758E-04	230.21	40.76	2.587E-04	336.86	18.39
DBY180A	426.6	3.499E-04	111.95	12.65	3.007E-04	205.92	17.15	2.859E-04	347.31	68.45

APPENDIX A2: WEST HAWK - HOLE 1-65 - AMS DATA

SAMPLE	DEPTH (m)	k_1 (SI)	DEC. (°)	INC. (°)	k_2 (SI)	DEC. (°)	INC. (°)	k_3 (SI)	DEC. (°)	INC. (°)
WHL 10A	265.5	1.793E-4	338.0	21.0	1.772E-4	237.0	27.0	1.742E-4	100.0	55.0
WHL 10B		1.058E-4	358.0	07.0	1.057E-4	268.0	01.0	1.038E-4	174.0	83.0
WHL 20A	267.3	1.568E-4	244.0	05.0	1.563E-4	146.0	59.0	1.549E-4	337.0	30.0
WHL 20B		1.753E-4	008.0	07.0	1.737E-4	278.0	05.0	1.718E-4	153.0	81.0
WHL 20C		1.744E-4	201.0	08.0	1.741E-4	291.0	03.0	1.711E-4	040.0	82.0
WHL 30A	290.1	3.281E-3	188.0	80.0	2.696E-3	097.0	00.0	1.961E-3	007.0	10.0
WHL 30B		6.082E-3	183.0	81.0	4.734E-3	093.0	00.0	3.376E-3	003.0	09.0
WHL 30C		9.123E-3	174.0	79.0	7.288E-3	278.0	03.0	4.979E-3	008.0	11.0
WHL 40A	292.8	3.022E-2	166.0	56.0	2.656E-2	313.0	30.0	1.896E-2	052.0	16.0

WHL 50A	357.9	7.523E-4	034.0	33.0	7.488E-4	164.0	45.0	7.387E-4	285.0	27.0
WHL 50B		7.813E-4	033.0	34.0	7.742E-4	166.0	45.0	7.614E-4	284.0	25.0
WHL 50C		8.285E-4	034.0	15.0	8.205E-4	135.0	36.0	8.105E-4	285.0	50.0
WHL 60A	358.2	1.356E-3	284.0	70.0	1.339E-3	088.0	19.0	1.327E-3	180.0	05.0
WHL 60B		1.125E-3	072.0	59.0	1.123E-3	248.0	31.0	1.118E-3	339.0	02.0
WHL 70A	391.8	1.544E-4	186.0	06.0	1.520E-4	088.0	56.0	1.499E-4	280.0	34.0
WHL 70B		1.572E-4	026.0	03.0	1.544E-4	118.0	31.0	1.502E-4	291.0	59.0
WHL 70C		1.549E-4	189.0	22.0	1.536E-4	080.0	38.0	1.496E-4	302.0	44.0
WHL 70D		1.682E-4	183.0	12.0	1.651E-4	087.0	25.0	1.632E-4	297.0	62.0

WHL 80A	444.0	4.990E-4	327.0	16.0	4.942E-4	192.0	67.0	4.778E-4	061.0	15.0
WHL 80B		1.777E-4	232.0	19.0	1.767E-4	139.0	06.0	1.754E-4	031.0	70.0
WHL 80C		1.776E-4	285.0	51.0	1.768E-4	170.0	19.0	1.738E-4	067.0	32.0
WHL 80D		1.971E-4	304.0	20.0	1.961E-4	035.0	04.0	1.939E-4	137.0	70.0
WHL 90A	505.8	4.166E-4	205.0	17.0	4.118E-4	308.0	35.0	4.010E-4	094.0	50.0
WHL 90B		2.630E-4	016.0	07.0	2.603E-4	107.0	08.0	2.594E-4	247.0	79.0
WHL 90C		3.659E-4	093.0	02.0	3.644E-4	003.0	11.0	3.605E-4	194.0	79.0
WHL 90D		3.803E-4	159.0	07.0	3.784E-4	068.0	08.0	3.734E-4	293.0	79.0
WHL100A	522.6	5.582E-5	279.0	12.0	5.353E-5	016.0	30.0	5.172E-5	169.0	57.0
WHL100B		1.741E-4	300.0	28.0	1.659E-4	200.0	18.0	1.628E-4	082.0	55.0

WHL100C		2.567E-4	291.0	14.0	2.493E-4	041.0	54.0	2.336E-4	192.0	32.0
WHL100D		8.448E-5	098.0	00.0	7.553E-5	008.0	25.0	6.581E-5	188.0	65.0
WHL110A	523.5	1.211E-3	012.0	06.0	1.155E-3	103.0	07.0	7.801E-4	240.0	81.0
WHL110B		1.453E-3	016.0	09.0	1.354E-3	286.0	03.0	9.481E-4	174.0	81.0
WHL120A	645.0	2.969E-4	148.0	09.0	2.956E-4	050.0	43.0	2.871E-4	248.0	46.0
WHL120B		1.504E-4	354.0	05.0	1.488E-4	085.0	13.0	1.403E-4	244.0	76.0
WHL120C	645.0	3.478E-4	154.0	01.0	3.440E-4	064.0	26.0	3.375E-4	246.0	64.0
WHL120D		1.299E-4	350.0	04.0	1.275E-4	082.0	20.0	1.215E-4	249.0	69.0
WHL130A	645.3	4.021E-4	088.0	07.0	4.013E-4	357.0	06.0	3.993E-4	227.0	81.0
WHL130B		4.032E-4	288.0	02.0	4.013E-4	018.0	08.0	3.919E-4	187.0	82.0

WHL130C		4.119E-4	130.0	03.0	4.087E-4	039.0	06.0	3.991E-4	247.0	83.0
WHL140A	692.7	1.084E-3	084.0	56.0	1.051E-3	328.0	16.0	9.760E-4	229.0	29.0
WHL140B		7.222E-4	101.0	52.0	7.084E-4	341.0	22.0	6.469E-4	237.0	30.0
WHL140C		1.297E-3	319.0	53.0	1.257E-3	057.0	06.0	1.147E-3	151.0	37.0
WHL140D		1.532E-4	328.0	01.0	1.413E-4	059.0	43.0	1.209E-4	237.0	47.0

APPENDIX A3: WEST HAWK - HOLE 1-66 - AMS DATA

SAMPLE	DEPTH (m)	k_1 (SI)	DEC. (°)	INC. (°)	k_2 (SI)	DEC. (°)	INC. (°)	k_3 (SI)	DEC. (°)	INC. (°)
WHL150A	150.0	8.423E-4	153.0	74.0	8.001E-4	267.0	07.0	7.753E-4	358.0	14.0
WHL150B		6.923E-4	129.0	76.0	6.882E-4	260.0	09.0	6.818E-4	351.0	10.0
WHL150C		6.910E-4	108.0	83.0	6.864E-4	259.0	06.0	6.814E-4	349.0	03.0
WHL150D		8.420E-4	156.0	74.0	7.972E-4	267.0	06.0	7.776E-4	358.0	15.0
WHL150E		7.022E-4	181.0	76.0	6.927E-4	272.0	00.0	6.829E-4	002.0	14.0
WHL160A	210.0	9.110E-4	020.0	77.0	8.318E-4	170.0	11.0	6.914E-4	261.0	06.0
WHL160B		8.054E-4	005.0	78.0	7.598E-4	175.0	12.0	6.512E-4	266.0	02.0
WHL160C		6.563E-4	358.0	71.0	6.308E-4	173.0	19.0	5.621E-4	263.0	02.0

WHL160D	210.0	8.327E-4	300.0	73.0	7.750E-4	130.0	16.0	6.749E-4	039.0	03.0
WHL160E		6.547E-4	307.0	75.0	6.275E-4	133.0	15.0	5.588E-4	042.0	01.0

APPENDIX A4: CLEARWATER WEST - HOLE 1-63 - AMS DATA

SAMPLE	DEPTH (m)	k_1 (SI)	DEC. (°)	INC. (°)	k_2 (SI)	DEC. (°)	INC. (°)	k_3 (SI)	DEC. (°)	INC. (°)
CWR200A	24.3	3.046E-02	102.71	67.61	2.731E-02	344.20	11.13	2.651E-02	250.28	19.18
CWR200B		4.945E-02	142.31	67.17	4.765E-02	16.36	13.88	4.238E-02	281.82	17.75
CWR200C		6.700E-02	134.35	75.38	6.220E-02	11.55	8.04	5.503E-02	279.81	12.12
CWR210A	52.2	3.400E-02	88.74	61.33	3.213E-02	224.02	21.24	2.966E-02	321.43	18.34
CWR210B		3.621E-02	76.25	69.46	3.297E-02	224.76	17.72	2.949E-02	318.01	10.05
CWR210C		7.925E-02	68.83	74.11	6.679E-02	218.98	13.86	5.544E-02	310.86	7.60
CWR210D		7.382E-02	64.65	71.43	6.355E-02	212.60	15.89	5.490E-02	305.29	9.35
CWR210E		4.206E-02	67.55	72.97	3.835E-02	211.95	13.99	3.459E-02	304.35	9.52
CWR210F		4.325E-02	54.96	66.45	3.934E-02	210.13	21.59	3.504E-02	303.72	8.98

CWR220A	87.0	3.226E-02	127.26	70.55	3.069E-02	359.41	12.23	2.915E-02	266.13	14.90
CWR220B		2.950E-02	112.99	72.60	2.773E-02	355.40	8.26	2.616E-02	263.14	15.21
CWR220C		2.553E-02	121.70	73.91	2.430E-02	353.92	10.02	2.238E-02	261.69	12.46
CWR220D		4.217E-02	191.96	30.04	3.775E-02	288.30	10.81	3.043E-02	35.87	57.68
CWR220E		3.850E-02	88.60	74.91	3.608E-02	346.27	3.29	3.374E-02	255.40	14.71
CWR220F		3.717E-02	100.09	73.74	3.445E-02	349.08	5.97	3.185E-02	257.47	15.07
CWR230A	111.9	3.012E-02	90.37	78.32	2.802E-02	190.33	2.03	2.577E-02	280.74	11.50
CWR230B		2.102E-02	81.95	81.18	1.986E-02	183.86	1.83	1.843E-02	274.14	8.63
CWR230C		2.901E-02	135.30	76.50	2.709E-02	9.81	7.94	2.416E-02	278.28	10.85
CWR230D		1.545E-02	57.55	81.58	1.446E-02	192.54	5.97	1.353E-02	283.16	5.91

CWR240A	114.6	3.820E-02	37.53	85.42	3.456E-02	202.91	4.43	3.125E-02	293.00	1.15
CWR240B		2.526E-02	76.68	83.63	2.409E-02	204.20	3.89	2.232E-02	294.54	5.03
CWR240C		2.957E-02	31.31	58.02	2.906E-02	189.62	30.13	2.751E-02	285.34	9.75
CWR240D		2.948E-02	30.01	79.26	2.840E-02	209.36	10.73	2.759E-02	299.38	0.14
CWR250A	138.9	1.202E-02	210.38	58.77	1.180E-02	16.14	30.45	1.138E-02	109.86	6.31
CWR250B		3.850E-02	221.61	81.76	3.448E-02	31.36	8.10	3.105E-02	121.57	1.45
CWR250C		5.051E-02	180.64	84.58	4.408E-02	32.07	4.64	3.767E-02	301.85	2.81
CWR250D		2.548E-02	169.33	83.61	2.328E-02	36.29	4.36	2.044E-02	305.93	4.65
CWR260A	170.1	3.086E-02	192.07	78.36	2.947E-02	333.99	9.21	2.777E-02	65.14	7.05
CWR260B		3.285E-02	156.71	75.20	3.151E-02	333.23	14.78	2.967E-02	63.46	0.86

CWR260C	170.1	2.566E-02	179.41	79.74	2.495E-02	347.47	10.04	2.380E-02	77.84	2.08
CWR260D		3.537E-02	177.40	85.98	3.412E-02	345.03	3.92	3.208E-02	75.09	0.86
CWR260E		3.379E-02	80.93	75.65	3.232E-02	292.77	12.26	3.042E-02	201.16	7.34
CWR260F		3.665E-02	45.82	80.87	3.488E-02	300.16	2.48	3.283E-02	209.78	8.79
CWR260G		3.637E-02	310.72	82.75	3.475E-02	111.13	6.84	3.222E-02	201.41	2.41
CWR270A	207.6	2.488E-02	59.54	25.57	2.409E-02	324.69	10.02	2.280E-02	215.05	62.27
CWR270B		2.138E-02	68.58	18.85	2.045E-02	333.51	14.50	1.962E-02	208.24	65.87
CWR270C		1.088E-02	77.04	6.10	1.046E-02	285.14	83.09	1.039E-02	167.38	3.21
CWR270D		1.351E-02	347.41	11.88	1.286E-02	241.80	51.99	1.278E-02	86.03	35.48
CWR270E		8.866E-03	345.86	18.71	8.559E-03	230.27	51.90	8.420E-03	87.98	31.81

CWR270F	207.6	1.114E-02	339.72	3.56	1.077E-02	248.74	15.40	1.038E-02	82.41	74.18
CWR280A	228.3	1.893E-02	355.48	47.75	1.842E-02	256.43	8.13	1.771E-02	159.28	41.10
CWR280B		1.640E-02	310.74	37.52	1.575E-02	56.96	19.99	1.511E-02	168.84	45.70
CWR280C		2.524E-02	354.08	54.84	2.426E-02	104.85	14.03	2.393E-02	203.66	31.49
CWR280D		3.366E-02	315.85	84.81	3.299E-02	221.23	0.38	3.191E-02	131.20	5.17
CWR280E		1.457E-02	18.15	48.41	1.431E-02	269.77	15.81	1.299E-02	167.34	37.32
CWR290A	265.5	5.928E-03	326.14	51.43	5.696E-03	58.35	1.75	5.665E-03	149.71	38.52
CWR290B		6.244E-03	327.42	72.93	6.215E-03	184.98	13.68	6.058E-03	92.52	10.01
CWR290C		5.982E-03	290.07	58.51	5.779E-03	175.93	14.06	5.765E-03	78.45	27.55
CWR290D		6.890E-03	89.64	55.49	6.857E-03	211.05	19.72	6.787E-03	311.60	27.07

CWR300A	295.5	1.907E-02	36.56	61.19	1.838E-02	293.87	6.89	1.747E-02	200.22	27.83
CWR300B		3.653E-02	330.42	34.27	3.522E-02	92.44	37.90	3.251E-02	213.54	33.57
CWR300C		9.462E-03	318.10	27.32	9.407E-03	74.90	41.12	9.002E-03	205.47	36.68
CWR300D		6.719E-03	77.06	39.92	6.677E-03	328.07	21.25	6.421E-03	217.18	42.52
CWR300E		5.978E-03	17.87	50.51	5.942E-03	117.16	7.57	5.670E-03	213.23	38.47
CWR310A	318.0	4.377E-03	211.71	45.44	4.336E-03	101.77	18.55	4.209E-03	356.17	38.71
CWR310B		4.468E-03	264.23	13.12	4.451E-03	160.71	45.11	4.327E-03	6.32	41.94
CWR310C		4.794E-03	219.08	38.51	4.767E-03	110.72	21.59	4.634E-03	358.52	43.68
CWR310D		4.303E-03	219.46	32.66	4.252E-03	117.54	17.85	4.152E-03	3.53	51.63
CWR310E		4.366E-03	247.76	26.12	4.323E-03	138.08	34.48	4.242E-03	6.21	44.18

CWR320A	350.4	4.149E-03	92.99	57.05	4.089E-03	226.49	24.04	3.999E-03	326.41	21.12
CWR320B		3.572E-03	45.81	67.45	3.536E-03	257.74	19.42	3.364E-03	163.80	11.03
CWR320C		3.519E-03	85.61	71.31	3.460E-03	259.62	18.60	3.342E-03	350.23	1.82
CWR320D		3.179E-03	69.50	66.29	3.127E-03	263.66	23.07	3.006E-03	171.44	5.20
CWR330A	375.0	3.577E-02	302.10	26.73	3.487E-02	172.11	51.93	2.828E-02	45.65	24.96
CWR330B		7.007E-03	151.35	23.88	6.507E-03	283.59	56.64	6.143E-03	51.13	21.86
CWR330C		4.271E-03	154.78	22.33	3.936E-03	36.22	49.33	3.677E-03	259.63	31.97
CWR330D		4.967E-03	161.41	23.78	4.563E-03	40.89	49.06	4.338E-03	266.82	31.10
CWR330E		6.488E-03	155.61	36.15	5.764E-03	271.22	30.62	5.553E-03	29.61	38.82
CWR340A	391.2	4.038E-03	65.88	65.02	3.980E-03	303.18	14.12	3.911E-03	207.88	20.16

CWR340B	391.2	5.658E-03	105.49	26.07	5.563E-03	342.16	48.32	5.366E-03	211.86	29.93
CWR340C		3.660E-03	124.24	19.14	3.570E-03	2.24	56.76	3.510E-03	224.00	26.04
CWR340D		4.511E-03	107.33	43.93	4.457E-03	337.18	33.80	4.318E-03	227.04	27.23
CWR340E		4.007E-03	114.06	39.94	3.975E-03	350.26	33.61	3.752E-03	235.67	32.05

APPENDIX A5: CLEARWATER EAST - HOLE 1-64 - AMS DATA

SAMPLE	DEPTH (m)	k_1 (SI)	DEC. (°)	INC. (°)	k_2 (SI)	DEC. (°)	INC. (°)	k_3 (SI)	DEC. (°)	INC. (°)
CWR010A	130.5	1.221E-04	292.00	6.00	1.198E-04	27.00	37.00	1.179E-04	194.00	52.00
CWR011A	130.8	3.490E-04	308.28	4.93	3.454E-04	213.05	46.55	3.161E-04	42.90	43.03
CWR011B		2.248E-04	25.55	17.26	2.128E-04	280.27	40.29	1.997E-04	133.42	44.64
CWR011C		1.346E-04	136.63	6.74	1.199E-04	231.04	33.03	1.109E-04	36.49	56.11
CWR011D		1.911E-04	275.22	28.97	1.847E-04	167.93	28.23	1.751E-04	42.22	47.39
CWR020A	137.4	1.440E-04	099.00	13.00	1.426E-04	006.00	13.00	1.412E-04	234.00	72.00
CWR020B		1.755E-04	047.00	7.00	1.727E-04	139.00	16.00	1.700E-04	294.00	72.00
CWR030A	153.0	2.798E-02	89.60	26.02	2.653E-02	202.20	38.21	2.379E-02	334.78	40.69
CWR030B		3.379E-02	87.43	21.75	3.222E-02	201.55	45.70	2.896E-02	340.39	36.30

CWR040A	182.4	7.063E-03	309.17	38.80	6.918E-03	128.05	51.19	6.476E-03	218.73	0.55
CWR040B		4.437E-03	65.61	28.53	4.256E-03	259.68	60.73	3.965E-03	158.89	6.00
CWR040C		5.964E-03	97.10	37.82	5.655E-03	276.16	52.18	5.375E-03	6.74	0.47
CWR040D		1.465E-02	336.69	56.59	1.393E-02	149.20	33.19	1.218E-02	241.46	3.44
CWR050A	202.8	1.264E-02	319.37	49.69	1.195E-02	139.57	40.31	1.101E-02	49.49	0.12
CWR050B		1.498E-02	139.26	25.11	1.417E-02	31.96	32.40	1.325E-02	259.30	46.88
CWR050C		7.895E-03	72.55	20.01	7.666E-03	317.53	49.27	7.523E-03	176.63	33.75
CWR055A	228.0	9.470E-02	90.37	3.11	7.466E-02	340.21	81.04	5.823E-02	180.83	8.39
CWR055B		8.099E-02	247.71	31.14	5.601E-02	2.47	34.74	4.587E-02	127.60	39.70
CWR055C		8.844E-02	276.43	0.64	6.768E-02	8.90	75.63	5.731E-02	186.27	14.35

CWR060A	239.4	7.940E-02	311.44	34.25	7.249E-02	160.01	52.21	5.630E-02	51.23	14.02
CWR060B		8.128E-02	318.76	23.18	7.417E-02	168.17	63.83	6.083E-02	53.75	11.48
CWR060C		7.550E-02	317.02	22.80	6.835E-02	159.62	65.52	5.371E-02	50.60	8.44
CWR060D		4.472E-02	321.67	23.89	4.060E-02	180.82	60.24	3.300E-02	59.27	16.63
CWR060E		3.728E-02	319.62	19.61	3.387E-02	183.78	63.58	2.907E-02	55.86	16.98
CWR070A	252.9	6.139E-03	139.77	54.63	6.089E-03	300.51	33.83	5.482E-03	36.69	9.13
CWR070B		1.378E-02	85.86	45.57	1.333E-02	285.60	42.69	1.223E-02	186.23	10.01
CWR080A	277.8	7.840E-03	224.45	14.16	7.262E-03	113.29	55.03	6.767E-03	323.24	31.21
CWR080B		9.977E-03	225.88	15.71	9.203E-03	114.53	52.30	8.639E-03	326.51	33.24
CWR080C		7.920E-03	228.46	20.67	7.398E-03	108.32	53.08	7.019E-03	330.58	29.08

CWR090A	332.4	2.403E-02	351.59	26.64	2.232E-02	229.43	46.70	2.142E-02	99.32	31.26
CWR090B		2.310E-02	14.38	37.27	2.171E-02	237.49	43.81	2.077E-02	123.33	23.11
CWR090C		2.704E-02	18.36	27.07	2.592E-02	227.26	59.72	2.442E-02	114.88	12.53
CWR090D		3.411E-02	0.07	8.69	3.222E-02	183.23	81.30	2.793E-02	90.16	0.45
CWR100A	411.9	2.277E-02	337.49	12.09	2.212E-02	93.77	64.21	2.070E-02	242.42	22.42
CWR100B		2.347E-02	335.12	46.96	2.144E-02	71.91	6.29	1.953E-02	167.67	42.35
CWR100C		3.995E-02	15.42	71.06	3.717E-02	235.83	14.64	3.618E-02	142.72	11.75
CWR100D		4.009E-02	126.00	73.19	3.859E-02	16.89	5.65	3.551E-02	285.28	15.78
CWR103A	430.8	5.271E-02	96.69	26.48	4.901E-02	257.32	62.17	4.333E-02	2.70	7.97
CWR103B		6.903E-02	96.26	23.00	6.409E-02	269.41	66.85	5.576E-02	5.23	2.45

CWR103C	430.8	7.026E-02	94.28	27.93	6.577E-02	260.39	61.36	5.814E-02	1.17	5.83
CWR103D		5.015E-02	248.92	28.64	4.795E-02	51.52	60.22	4.212E-02	154.80	7.49
CWR103E		4.582E-02	250.78	38.94	4.430E-02	50.89	49.33	3.762E-02	152.65	9.93
CWR103F		4.951E-02	257.34	52.19	4.658E-02	53.16	35.29	3.912E-02	151.68	11.83
CWR106A	439.5	5.582E-03	147.09	36.28	5.231E-03	306.85	51.96	4.843E-03	49.73	9.90
CWR106B		9.751E-03	147.93	34.61	8.942E-03	334.60	55.21	8.299E-03	240.09	3.13
CWR106C		9.001E-03	154.69	34.82	8.332E-03	1.68	52.02	7.673E-03	254.12	13.25
CWR106D		1.899E-02	154.50	26.76	1.782E-02	13.83	56.90	1.639E-02	253.93	18.00
CWR110A	478.8	4.841E-03	143.17	27.84	4.410E-03	36.82	28.05	4.140E-03	269.77	48.48
CWR110B		1.273E-02	146.81	18.20	1.184E-02	33.82	49.90	1.124E-02	249.76	34.28

CWR110C	478.8	1.364E-02	144.93	20.31	1.257E-02	359.49	65.86	1.194E-02	239.71	12.68
CWR113A	503.4	3.289E-02	184.56	1.38	2.913E-02	276.44	53.82	2.573E-02	93.55	36.15
CWR113B		2.878E-02	3.29	5.24	2.544E-02	263.90	60.67	2.230E-02	96.17	28.77
CWR113C		2.903E-02	356.19	8.65	2.623E-02	251.31	59.36	2.284E-02	91.06	29.14
CWR113D		2.832E-02	14.12	7.99	2.534E-02	273.42	52.87	2.213E-02	109.96	35.97
CWR113E		2.830E-02	12.19	11.78	2.541E-02	259.88	61.23	2.283E-02	107.99	25.84
CWR113F		3.180E-02	11.51	8.71	2.848E-02	266.05	60.15	2.514E-02	106.24	28.31
CWR115A	525.3	2.314E-02	114.88	3.34	2.101E-02	14.24	72.42	1.911E-02	205.92	17.23
CWR115B		7.749E-04	119.50	44.66	7.519E-04	245.10	30.50	6.870E-04	354.89	29.89
CWR115C		1.167E-03	103.89	9.52	1.117E-03	315.51	78.86	1.012E-03	194.85	5.73

CWR115D	525.3	2.812E-03	102.40	16.09	2.642E-03	316.33	70.83	2.308E-03	195.36	10.14
CWR117A	546.9	7.739E-02	249.83	8.73	7.414E-02	97.30	80.18	6.615E-02	340.52	4.46
CWR117B		7.282E-02	74.42	0.74	6.675E-02	167.69	77.21	5.616E-02	344.25	12.77
CWR117C		9.792E-02	76.39	0.52	8.631E-02	167.65	67.41	7.045E-02	346.18	22.59
CWR120A	559.2	8.891E-02	63.02	14.59	7.868E-02	312.43	53.48	7.022E-02	162.61	32.62
CWR120B		9.147E-02	57.96	9.40	7.951E-02	311.68	59.44	6.853E-02	153.18	28.78
CWR120C		9.739E-02	56.87	13.36	8.021E-02	301.34	61.14	7.116E-02	153.25	25.07
CWR123A	575.1	4.240E-02	36.49	0.81	3.469E-02	128.49	67.92	3.005E-02	306.16	22.07
CWR123B		4.906E-02	335.89	5.56	4.131E-02	70.88	41.72	3.647E-02	239.75	47.73
CWR126A	594.6	2.228E-01	199.38	14.37	2.023E-01	107.08	8.93	1.996E-01	346.18	72.98

CWR126B	594.6	1.524E-01	215.53	4.17	1.302E-01	108.55	75.98	1.229E-01	306.52	13.36
CWR126C		1.350E-01	213.87	11.60	1.084E-01	113.81	40.42	9.929E-02	316.70	47.25
CWR126D		9.307E-02	218.00	5.14	7.822E-02	127.16	9.28	7.473E-02	336.63	79.37
CWR130A	629.7	2.108E-02	92.94	14.06	1.821E-02	195.12	40.12	1.671E-02	347.66	46.48
CWR130B		2.947E-02	107.62	10.12	2.422E-02	206.91	42.14	2.211E-02	6.94	46.09
CWR130C		2.352E-02	101.54	4.06	1.924E-02	194.97	40.17	1.746E-02	6.77	49.54
CWR130D		1.116E-02	287.04	9.96	9.831E-03	179.76	59.59	9.378E-03	22.51	28.49
CWR130E		1.235E-02	295.67	13.71	1.121E-02	193.71	40.35	1.056E-02	40.52	46.41
CWR135A	641.4	1.041E-01	311.80	1.21	8.909E-02	42.93	43.15	7.895E-02	220.51	46.83
CWR135B		1.131E-01	240.70	28.53	1.075E-01	146.88	6.98	9.927E-03	44.39	60.47

CWR135C	641.4	1.115E-01	309.48	1.59	9.364E-02	217.78	46.91	7.988E-02	40.96	43.04
CWR135D		1.130E-01	135.86	1.87	9.428E-02	227.87	47.14	7.756E-02	44.13	42.80
CWR140A	702.0	1.174E-02	308.70	39.35	9.876E-03	164.28	44.76	9.492E-03	54.75	18.63
CWR140B		1.051E-02	312.42	39.48	8.633E-03	175.69	41.48	8.396E-03	63.27	23.37
CWR140C		1.288E-02	313.43	42.78	1.062E-02	190.14	30.67	1.049E-02	78.51	31.84
CWR140D		1.473E-02	310.26	43.22	1.256E-02	173.66	37.71	1.147E-02	64.18	23.34
CWR150A	780.9	1.056E-02	336.89	34.15	9.231E-03	157.00	55.85	8.618E-03	66.98	0.18
CWR150B		6.090E-03	330.53	40.46	5.344E-03	168.76	48.08	5.176E-03	68.43	9.15
CWR150C		5.924E-03	317.32	44.97	5.533E-03	170.23	40.04	5.327E-03	65.24	17.12
CWR160A	855.6	3.640E-02	258.56	32.38	3.116E-02	148.99	27.84	3.033E-02	27.46	44.72

CWR160B	855.6	2.845E-02	270.39	36.21	2.572E-02	137.64	42.84	2.490E-02	21.07	25.75
CWR160C		3.404E-02	275.02	32.72	2.961E-02	163.22	30.02	2.825E-02	41.18	42.56
CWR160D		2.829E-02	264.78	44.53	2.479E-02	145.59	26.37	2.271E-02	36.14	33.89
CWR160E		3.095E-02	241.91	51.74	2.538E-02	333.49	1.24	2.504E-02	64.39	38.23
CWR165A	906.3	9.324E-02	52.38	23.71	8.042E-02	320.06	5.28	6.524E-02	218.30	65.64
CWR165B		9.251E-02	54.33	23.80	7.621E-02	321.12	7.23	6.430E-02	215.34	64.99
CWR165C		9.527E-02	59.75	23.23	7.972E-02	325.56	9.67	6.667E-02	214.51	64.61
CWR165D		9.716E-02	59.96	23.15	8.055E-02	324.24	13.11	6.825E-02	207.04	63.01
CWR170A	933.0	1.143E-01	70.71	30.71	8.969E-02	339.20	2.54	7.852E-02	244.95	59.16
CWR170B		1.264E-01	73.58	29.08	9.906E-02	341.03	4.58	8.176E-02	242.90	60.49

CWR170C	933.0	1.268E-01	75.63	27.82	9.902E-02	342.39	6.11	8.165E-02	241.06	61.40
CWR170D		1.365E-01	75.03	21.75	1.078E-01	340.97	10.06	8.855E-02	227.72	65.82
CWR180A	981.0	5.023E-02	20.10	2.17	4.979E-02	110.33	6.05	4.503E-02	270.46	83.57
CWR180B		5.817E-02	33.37	4.02	5.706E-02	124.86	20.30	5.284E-02	292.66	69.27
CWR180C		5.346E-02	104.89	30.65	5.170E-02	7.20	12.71	4.784E-02	257.46	56.27
CWR180D		7.453E-02	9 3.1	42.67	5.409E-02	271.75	1.53	3.043E-02	180.17	47.29

APPENDIX B: NRM DATA

APPENDIX B1: DEEP BAY - HOLE 62-1A - NRM DATA

SAMPLE	DEPTH (m)	DECL. (°)	INCL. (°)	INTENSITY (mA/m)
010A	93.9	108.9	56.9	0.183
010B		357.5	-14.4	0.587
010C		311.1	17.2	1.749
010D		276.3	23.3	1.724
010E		206.1	31.3	0.423
020A	120.6	250.4	-52.9	301.4
020B		238.4	-56.8	159.7
020C		240.1	-57.3	125.7
020D		233.8	-76.6	78.15
030A	141.3	351.3	82.9	8.837
030B		22.6	85.1	14.03
030C		46.5	83.7	23.43
030D		14.0	78.3	19.72
030E		344.6	75.8	15.62
040A	173.1	259.6	45.5	1.396
040B		290.9	13.7	6.021
040C		100.3	14.1	8.234
040D		135.0	-24.4	1.344
050A	184.5	252.3	68.8	4.170
050B		94.8	71.9	1.766
050C		11.6	45.0	1.009
050D		274.2	67.8	1.005

050E	184.5	89.7	-6.9	0.3866
060A	204.9	60.3	69.5	4.558
060B		182.7	13.6	2.484
060C		37.1	61.9	3.079
060D		348.9	59.6	1.669
060E		151.4	64.3	1.313
070A	226.5	114.3	49.9	4.859
070B		155.0	76.8	3.686
070C		91.5	69.9	2.019
080A	233.7	297.4	77.5	1.906
080B		88.9	62.4	2.690
080C		314.3	22.0	2.239
090A	246.0	118.3	76.6	2.613
100A	276.0	106.1	74.3	2.157
100B		93.7	67.4	1.667
100C		100.1	74.9	8.203
100D		16.8	82.5	2.692
110A	288.0	154.8	87.5	19.65
110B		283.3	81.9	25.60
110C		213.7	87.1	97.35
110D		211.2	72.7	1110
110E		232.2	76.9	136.9
120A	294.0	166.2	68.4	25.27
120B		211.4	77.0	7.304
120C		15.8	83.7	2.650

130A	315.0	205.1	66.0	7.936
130B		222.2	84.6	6.348
140A	321.6	31.9	83.5	46.95
140B		17.4	84.2	30.83
140C		352.1	85.0	34.97
140D		331.2	81.8	26.40
140E		321.3	84.8	25.94
150A	351.3	276.0	31.5	3.354
150B		253.3	0.6	0.545
150C		191.6	-11.3	1.287
150D		145.8	-5.9	3.904
150E		320.6	-16.6	2.008
160A	384.6	29.5	78.8	1.449
160B		117.8	61.8	1.176
160C		124.0	80.3	1.428
170A	394.5	125.3	62.0	13.31
170B		255.1	70.6	13.57
170C		150.1	83.6	15.84
170D		322.7	68.2	15.21
180A	426.6	226.9	59.3	0.999

APPENDIX B2: WEST HAWK - HOLE 1-65 - NRM DATA

SAMPLE	DEPTH (m)	DECL. (°)	INCL. (°)	INTENSITY (mA/m)
010A	265.5	202.4	55.8	0.69771
020A	267.3	110.5	-38.0	0.58986
020B		173.3	-58.3	0.43809
020C		145.9	-70.6	0.64795
030A	290.1	171.8	88.5	125.97
030B		257.3	81.2	96.041
030C		261.6	78.2	139.07
040A	292.8	269.8	-75.3	475.00
050A	357.9	56.0	-31.1	2.0293
050B		88.6	-29.4	1.7656
050C		85.7	-14.5	5.2560
060A	358.2	165.7	-76.0	1.7796
060B		123.7	-22.4	0.78245
070A	391.8	78.7	-01.3	1.3932
070B		66.5	-16.7	4.8418
070C		252.7	-20.3	4.1836
070D		307.0	-15.4	2.7777
080A	444.0	256.8	07.2	0.66755
080B		60.6	-19.8	1.9145
080C		344.7	-64.5	1.6743
080D		356.4	-11.9	0.75370
090A	505.8	333.3	-12.8	21.953

090B	505.8	317.6	-51.4	4.9316
090C		99.0	40.2	2.3515
090D		49.5	-61.9	0.87599
100A	522.6	40.7	46.7	5.5594
100B		22.3	46.4	12.380
100C		46.8	57.9	20.106
100D		75.4	22.5	12.530
110A	523.5	30.5	06.1	3689.6
110B		187.1	-09.2	2155.3
120A	645.0	38.4	02.0	2.1400
120B		80.3	-02.6	3.6199
120C		88.9	-06.5	2.4282
120D		33.1	0.8	5.3334
130A	645.3	355.9	1.9	1.0264
130B		350.7	-0.6	5.9248
130C		14.4	-6.2	2.1496
140A	692.7	76.9	-24.3	0.35610
140B		145.1	19.6	3.3570
140C		302.4	60.7	159.21

APPENDIX B3: WEST HAWK - HOLE 1-66 - NRM DATA

SAMPLE	DEPTH (m)	DECL. (°)	INCL. (°)	INTENSITY (mA/m)
150A	150	170.4	83.1	23.084
150B		81.5	-37.3	1.7302
150C		69.1	-67.6	4.1568
150D		225.7	46.8	25.799
150E		122.0	76.6	13.161
160A	210	15.3	72.2	52.815
160B		349.1	53.6	39.068
160C		7.7	48.5	28.835
160D		138.1	-70.0	28.028
160E		134.8	-62.0	19.055

APPENDIX B4: CLEARWATER WEST - HOLE 1-63 - NRM DATA

SAMPLE	DEPTH (m)	DECL. (°)	INCL. (°)	INTENSITY (mA/m)
200A	024.3	322.0	14.4	550.88
200B		334.6	10.0	852.91
200C		333.4	15.2	1137.2
210A	052.2	77.7	2.7	664.55
210B		72.6	1.9	555.27
210C		63.4	-12.3	1145.2
210D		60.8	7.8	997.69
210E		65.2	3.7	696.19
210F		58.5	-6.4	777.93
220A	087.0	329.4	19.3	1059.4
220B		327.4	19.3	974.97
220C		334.2	15.4	830.75
220D		333.7	17.9	1329.0
220E		331.8	14.9	1114.7
220F		332.4	12.8	1027.6
230A	111.9	45.3	-0.4	570.95
230B		40.3	-2.7	438.02
230C		34.3	-1.0	619.16
230D		43.5	-13.3	327.13
240A	114.6	223.7	-6.2	1022.4
240B		226.1	-4.5	999.73
240C		216.6	-3.3	1293.7

240D	114.6	220.2	-9.0	1116.0
250A	138.9	56.8	-3.0	511.76
250B		55.3	1.4	972.96
250C		51.6	3.2	1254.2
250D		53.5	2.3	772.12
260A	170.1	31.7	3.9	1244.0
260B		26.6	-8.5	1905.0
260C		31.7	-5.3	1064.1
260D		35.8	-2.6	967.51
260E		165.1	10.1	796.26
260F		165.3	5.8	945.32
260G		163.2	6.7	894.25
270A	207.6	137.9	-7.5	782.60
270B		138.1	-7.8	691.65
270C		130.7	-7.3	436.56
270D		40.3	-6.7	473.94
270E		36.5	-3.9	369.93
270F		38.2	-8.4	418.22
280A	228.3	87.9	-18.7	300.85
280B		87.4	-27.5	248.80
280C		100.7	-6.1	381.90
280D		99.2	-1.5	515.14
280E		91.1	-0.4	320.43
290A	265.5	174.7	-1.7	299.09
290B		180.3	-1.9	318.70

290C	265.5	181.0	-0.1	275.97
290D		178.5	-5.6	352.27
300A	295.5	338.6	-4.5	752.21
300B		339.6	4.0	1361.4
300C		343.6	-2.9	511.78
300D		347.0	-2.9	367.21
300E		347.3	-5.9	324.92
310A	318.0	86.6	4.4	153.03
310B		92.2	7.0	156.83
310C		95.2	11.4	185.43
310D		93.8	13.2	159.18
310E		96.4	9.9	161.29
320A	350.4	335.6	-0.2	185.01
320B		327.8	-2.6	151.74
320C		333.2	-2.2	155.26
320D		333.8	-4.6	141.84
330A	375.0	148.5	36.2	966.99
330B		170.7	0.7	212.97
330C		173.0	-16.6	182.00
330D		175.1	-14.3	222.47
330E		171.0	-17.7	284.93
340A	391.2	1.8	37.6	164.79
340B		2.4	20.3	206.53
340C		6.4	8.8	117.85
340D		3.1	3.6	190.00

APPENDIX B5: CLEARWATER EAST - HOLE 1-64 - NRM DATA

SAMPLE	DEPTH (m)	DECL. (°)	INCL. (°)	INTENSITY (mA/m)
010A	130.5	97.2	-32.4	3.9570
011A	130.8	220.8	26.4	6.4294
011B		173.6	13.6	10.306
011C		162.6	-2.3	8.0159
011D		199.9	59.4	6.6649
020A	137.4	228.8	21.2	7.6334
020B		229.9	14.6	7.7684
030A	153.0	259.0	3.4	487.99
030B		265.0	20.5	814.38
040A	182.4	111.2	13.8	29.707
040B		95.5	36.7	15.556
040C		113.4	-10.3	38.194
040D		309.1	40.8	103.54
050A	202.8	322.9	24.3	90.021
050B		169.0	63.1	33.189
050C		182.7	41.0	41.064
055A	228.0	84.1	-6.0	1361.8
055B		84.8	0.6	1353.0
055C		88.9	-3.7	1424.6
060A	239.4	151.8	16.1	1388.1
060B		155.1	15.1	1744.0
060C		152.4	16.9	1796.3

060D	239.4	154.5	14.5	1478.2
060E		159.4	9.8	1235.2
070A	252.9	123.8	18.6	73.507
070B		41.1	40.4	119.12
080A	277.8	254.0	23.0	159.59
080B		262.1	18.1	226.72
080C		259.5	19.6	181.42
090A	332.4	166.8	42.0	231.71
090B		171.2	45.9	212.57
090C		179.9	37.2	258.06
090D		186.0	34.5	446.63
100A	411.9	227.3	50.8	197.64
100B		248.1	57.6	141.48
100C		174.7	8.9	502.16
100D		187.2	31.9	432.74
103A	430.8	121.6	65.0	757.77
103B		130.8	70.5	1465.9
103C		129.3	70.4	1565.7
103D		287.4	60.2	604.22
103E		274.4	60.8	567.01
103F		269.8	64.9	514.89
106A	439.5	171.2	25.0	187.15
106B		176.7	23.3	302.05
106C		179.3	25.5	265.28
106D		175.7	20.1	527.87

110A	478.8	175.0	31.7	125.60
110B		176.0	32.9	368.68
110C		175.8	35.8	380.00
113A	503.4	46.8	63.1	500.76
113B		48.2	65.5	383.38
113C		61.9	68.7	400.69
113D		74.4	69.9	405.50
113E		83.0	74.5	398.04
113F		69.1	71.8	459.41
115A	525.3	126.8	20.2	489.62
115B		110.7	30.5	29.963
115C		119.8	26.9	38.710
115D		119.7	24.5	81.614
117A	546.9	273.7	35.0	2827.0
117B		278.2	36.4	2306.4
117C		277.7	32.4	2966.1
120A	559.2	71.1	80.5	2255.4
120B		88.7	84.2	2079.9
120C		62.4	82.9	1854.6
123A	575.1	244.3	50.1	929.85
123B		179.3	48.2	1159.0
126A	594.6	220.6	65.3	7017.0
126B		212.9	69.1	4896.6
126C		232.1	70.8	6158.6
126D		216.1	68.2	4926.1

130A	629.7	289.6	56.7	661.59
130B		306.9	61.6	858.40
130C		297.6	54.6	634.81
130D		299.6	59.7	256.54
130E		309.1	58.5	305.81
135A	641.4	138.1	52.6	3014.4
135B		321.1	50.1	3152.5
135C		320.7	49.8	3291.8
135D		325.6	47.2	3453.0
140A	702.0	333.9	55.1	208.04
140B		335.2	43.4	169.86
140C		337.6	40.4	221.69
140D		342.6	46.9	260.59
150A	780.9	41.9	84.1	822.71
150B		6.8	81.9	413.85
150C		15.0	85.3	501.46
160A	855.6	10.6	86.7	5293.3
160B		313.5	82.0	4471.3
160C		334.0	83.1	5129.3
160D		49.9	83.8	4908.6
160E		42.6	84.0	6608.0
165A	906.3	224.5	70.9	5522.8
165B		217.5	68.4	5416.2
165C		222.2	70.3	5455.7
165D		218.1	69.7	5589.0

170A	933.0	353.7	74.3	8258.7
170B		284.2	69.1	9605.4
170C		281.4	64.7	7507.8
170D		289.2	84.8	10706
180A	981.0	165.1	69.9	5263.9
180B		218.7	78.0	8944.1
180C		238.3	78.1	8869.9
180D		236.6	83.0	9336.2